

Searching for late-time interaction between Type Ia supernovae and distant circumstellar material using the Zwicky Transient Facility

A dissertation submitted to the University of Dublin
for the degree of Doctor of Philosophy

Jacco H. Terwel

School of Physics, Trinity College Dublin

Supervisor:

Prof. Kate Maguire

September 2024



Trinity College Dublin
Coláiste na Tríonóide, Baile Átha Cliath
The University of Dublin

Declaration

I agree to deposit this thesis in the University's open access institutional repository or allow the Library to do so on my behalf, subject to Irish Copyright Legislation and Trinity College Library conditions of use and acknowledgement.

I consent to the examiner retaining a copy of the thesis beyond the examining period, should they so wish (EU GDPR May 2018).

Name: Jacco H. Terwel

Signature: **Date:** 01/09/2024

Summary

... abstract ...

... dedication ...

Acknowledgements

... acknowledgements ...

List of Publications

Publications

1. ... publications ...

Contents

List of Publications	vi
List of Figures	x
List of Tables	xvii
1 Introduction	1
1.1 The final stages of stars	1
1.1.1 Stars below $8 M_{\odot}$	1
1.1.2 Stars above $8 M_{\odot}$	2
1.2 The transient universe	4
1.2.1 Core Collapse Supernovae	4
1.2.2 Thermonuclear SNe	7
1.2.2.1 Standardizable candles	8
1.2.3 Other types of transients	9
1.2.3.1 SLSN - Superluminous Supernova	9
1.2.3.2 AGN - Active Galactic Nucleus	10
1.2.3.3 TDE - Tidal Disruption Event	10
1.2.3.4 ANT - Ambiguous Nuclear Transient	11
1.2.3.5 Variable stars	11
1.3 SN Ia progenitor systems	12
1.3.1 Single degenerate	12
1.3.2 Double degenerate	14
1.4 Subclasses	14
1.4.1 Photometric differences	15
1.4.2 Spectroscopic differences	17
1.5 SNe with circumstellar material	17
1.5.1 The SN Ia-CSM subclass	18
1.5.2 CSM in CCSNe	21
1.5.3 Distant CSM	22
1.6 In this thesis:...	23
2 Observing in the optical regime	25
2.1 Types of obeservations	25
2.1.1 Photometry	26
2.1.2 Spectroscopy	26
2.2 Telescopes	28
2.2.1 Zwicky Transient Facility	28
2.2.2 Nordic Optical Telescope	30
2.2.3 Gran Telescopio CANARIAS	30

2.2.4	Other observations	31
2.3	Calibration images	32
2.3.1	Bias	32
2.3.2	Dark	32
2.3.3	Flatfield	33
2.3.4	Arc	33
2.4	Reduction	34
2.4.1	Bias, dark, and flat corrections	35
2.4.2	Cosmic-ray removal and image stacking	35
2.4.3	Standard star calibration	35
2.4.4	Forced photometry	36
2.5	General considerations for observing	38
2.5.1	Location	38
2.5.2	Telescope, instrument, observation type, and setup	39
2.5.3	Night plan	40
3	ZTF SN Ia DR2: Searching for late-time interaction signatures in Type Ia supernovae from the Zwicky Transient Facility	42
3.1	Data	42
3.1.1	ZTF light curve data	43
3.1.2	Baseline correction	44
3.2	Analysis	45
3.2.1	Binning & filtering programme	46
3.2.2	Removal of SN Ia radioactive tail detections	47
3.2.3	SuperNova Animation Programme (SNAP)	49
3.2.4	Simulated interaction recovery fractions	50
3.2.4.1	The interacting SN model	51
3.2.4.2	Simulating the observing campaign	52
3.2.4.3	Simulated interaction recovery	55
3.2.4.4	Impact of reference image depth	57
3.3	Results	57
3.3.1	Initial summary of detected events	58
3.3.1.1	Known Ia-CSM	60
3.3.1.2	Siblings	62
3.3.1.3	Kinked tails	64
3.3.2	Additional tests of promising events	67
3.3.2.1	Scene modelling photometry	68
3.3.2.2	AGN contamination	69
3.3.2.3	Presence of a sibling close to the SN location	70
3.3.2.4	Late-time interaction candidates	76
3.3.3	Late-time CSM interaction rates based on my candidate objects	82
3.4	Discussion	86
3.4.1	Late-time interaction is rare in SNe Ia	86
3.4.2	Properties of SNe Ia with late-time interaction	88
3.4.3	Limitations of the analysis	89
3.4.4	By-product pipeline detections	91
3.5	Conclusions	91
3.6	Tables	93

3.7	Inputs to SIMSURVEY simulations	96
3.8	Late-time spectrum of SN 2020alm	96
3.9	Binned SMP light curves of the final candidates	98
4	ZTF-observed late-time signals of pre-ZTF transients	101
4.1	Data	101
4.2	Analysis	103
4.2.1	Detection pipeline modifications	105
4.2.2	Removing false positives	106
4.2.3	Estimating CSM masses	108
4.3	Results	111
4.3.1	Pre-ZTF transients still active in ZTF	111
4.3.1.1	AT 2017gpy - a 14hls-like event	112
4.3.2	Siblings	115
4.3.3	Non-SN sources of flux excesses in ZTF	117
4.3.4	Final shortlist of late-time interaction	119
4.4	Discussion	129
4.4.1	Rarity of late-time signals from SNe	130
4.4.1.1	Siblings	131
4.4.1.2	Serendipitous nuclear transient detections	131
4.4.1.3	CSM interaction	132
4.4.2	Limitations	133
4.5	Conclusions	136
4.6	Tables	137
4.7	Recovered non-SN sources	140
References		143

List of Figures

1.1	Schematic view of the onion structure of a highly evolved massive star just before core collapse, with light elements on the outside and heavier elements towards the core. Typical values are given along the horizontal and vertical axes. This figure originally comes from chapter 35 of Kippenhahn et al. (2013).	3
1.2	<i>gri</i> composite image of NGC4216 using observations taken by the Zwicky Transient Facility. Left: composite image of observations taken before 1 January 2024. Right: composite image of observations taken between 5 and 19 January 2024, the first two weeks after the first detection of the Type Ia SN 2024gy. (Credit: Benjamin Nobre Hauptmann)	5
1.3	<i>gril</i> ight curve of a SN Ia in the rest frame and at absolute magnitude, corrected for Milky Way extinction but not for host extinction. The <i>g</i> -band clearly shows a change in the decline rate as ^{56}Co decay becomes dominant over ^{56}Ni decay. The <i>r</i> and <i>i</i> -band show the second peak. This light curve is made using ZTF observations.	8
1.4	Left: Artistic impression of a single degenerate system, where the white dwarf accretes material coming from the surface of the donor star. Image credit: STFC / David Hardy. Right: Artistic impression of a double degenerate system where two white dwarfs spiral in to each other while releasing gravitational waves. Image credit: NASA / Tod Strohmayer (GSFC) / Dana Berry (Chandra X-Ray Observatory).	13
1.5	Subclasses of SN Ia. The peak absolute B-band magnitude is plotted as a function of Δm_{15} in the same band. Normal SNe Ia lie along the Phillips relation, which is shown with a black line. Most of the non-normal subclasses can separated from normal SNe Ia based on these two values alone. The only exception are the 91T-like SNe, which form a subclass based on their spectral differences from normal SNe Ia. This figure was taken from Taubenberger (2017).	16
1.6	Schematic view of a SN Ia-CSM event. Top: The progenitor system containing a WD feeding on material from the donor star. Through various mechanisms a fraction of this material can be lost from the system and end up as CSM in a disk or shell at a distance d around the progenitor system. Middle: The WD explodes as a SN Ia. This can be a SN Ia-norm or a peculiar object, depending on the progenitor system. The ejecta start traveling outwards from the explosion site. Bottom: The ejecta catch up to the CSM and start interacting with it, causing the CSM to start emit light as well as it is swept up. This results in a slowing down of the photometric light curve decline and narrow emission lines in the spectra. Needs aligning	19

-
- 2.1 Image and partial spectrum of SN 2024nqr (left) and SN 2024pgd (right), two SNe Ia active simultaneously in the same galaxy. The image was taken without a filter and used to align the 1.0" slit (horizontal dashed lines) over both SNe. The resulting spectrum, taken with grism #4, shows three traces as white vertical stripes. The outer two line up with the two SNe, while the middle trace is from the host galaxy edge in the slit (vertical dotted lines for guidance). The horizontal lines in the spectrum are sky lines coming from atmospheric emission, and the white spots in the spectrum are due to cosmic rays. This data was taken with NOT+ALFOSC on the night of 28 July 2024 while testing an experimental rapid response mode (RRM, credit: Samuel Grund Sørensen). **check AT/SN status weirdness** 27
- 2.2 Throughput as a function of wavelength of the different filters used to gather the bulk of the data in this thesis *g* filters are shown in green, *r* in orange, *i* in red, and the different telescopes are shown with different line styles (Continuous for ZTF, dashed for NOT, dot-dashed for GTC). The SDSS filter transmissions (dotted lines) are shown for comparison. For the grisms the wavelength ranges are shown as only, not their efficiency at each wavelength. 29
- 2.3 Night plan for the NOT on the night of 10 August 2024. Targets are plotted with their altitude as a function of universal standard time. Local stellar time is shown on top. The target priority has been colour coded, with the coloured bars showing the amount of time each observation is expected to take. Green targets have already been completed, and the red vertical line shows the current time. Several unscheduled backup targets are shown in case the plan has to be updated during the night. 41
- 3.1 First 250 days of the *gri*-band light curves of SN 2019hbb in flux scaled to the peak flux (top panel) and magnitude (bottom panel) space. Binning starts 100 days after the estimated peak date (vertical black dashed and solid lines), using 25 d bins. The *g*-, *r*-, and *i*-bands are shown green, orange, and red, respectively. Before 100 days, I show the unbinned detections with their uncertainties (coloured circles) and non-detections (inverted triangles). After 100 days I show the bins as horizontal lines to show their size, a circle to show their mean value, and the shaded region showing the 1σ uncertainty (dashed regions are non-detections). A bin is deemed a non-detection if the flux $f < 5\sigma_f$. The 5σ magnitude limit is calculated and shown as a downward arrow. In both the *g*- and *r*-bands, the first bin is a detection and there are multiple adjacent bins with detections, triggering the tail-fitting procedure (see Section 3.2.2). The resulting tail fits are shown in the green and red lines, respectively, with their 1σ uncertainties as hashed regions. The half-life times are $t_{1/2,g} = 70 \pm 6$ d ($\chi^2_{\text{red}} = 0.6$) and $t_{1/2,r} = 27 \pm 4$ d ($\chi^2_{\text{red}} = 1.4$). This tail is therefore deemed to be a normal SN Ia tail. 48

- 3.6 Binned late-time observations of the recovered known SNe Ia-CSM. All objects are shown in absolute magnitude and over the same time range for easy comparison. All objects are detected beyond 100 days after the peak without using the binning technique. I do not show these individual data points to increase readability. The tail fits are shown as solid lines with the hashed region denoting their 1σ uncertainties. For comparison, SN 2020ssf (ZTF20abyptpc) in the top left corner is a normal SN Ia with a normally declining tail with $t_{1/2,g} = 53 \pm 1$ days and $t_{1/2,r} = 26 \pm 1$ days. The fitted tails for the SNe Ia-CSM are significantly shallower. 61
- 3.7 Binned late-time observations in flux space of the five events with a detected sibling, with the flux normalised to the found peak flux. All objects are plotted on the same flux scale for easy comparison except for SN 2018big, as its late-time detections are much weaker compared to the original SN peak magnitude due to the larger distance offset between the siblings. 62
- 3.8 Light curves of SN 2018big and its sibling SN 2019nvm in magnitude space using bins of 25 d. The g (green) and r (orange) bins follow the tail of SN 2018big until it disappears in the noise. About 450 d after the peak of SN 2018big, new detections are identified in the binned photometry. The individual observations remain upper limits, although their shape hint to the true nature of these late-time detections. 63
- 3.9 Five objects with kinks in their tails that start to deviate from the assumed decline rate at $\sim 200 - 250$ d post peak are shown in magnitude space as a function of days since peak. As most of these objects have their peak magnitude blinded, no scaling is shown. A normal radioactive decay model was fitted to these tails, shown as solid straight lines with their 1σ uncertainty as dashed regions. But as the ejecta opacity changes over time so does the half-life time of the tail, causing a kink seen in the bins which is not reproduced by the model. The arbitrarily normalised R -band light curve of SN 2011fe (known not to have CSM interaction from detailed spectral studies) (Zhang et al., 2016) is shown in blue, showing the same shift in decline slope at a similar phase. 65
- 3.10 Two objects whose late-time detections were revealed to be caused by the photometry extraction. The colours are as in Fig. 3.9. The left side shows the binned forced photometry light curve, and the right side shows the binned SMP light curve. Bins with 5σ detections are shaded solid, while the non-detections are hashed. 68
- 3.11 Objects whose late-time detections are explained in the additional tests. The top four rows show the light curves of the objects where a previously undetected sibling transient as an explanation for the late-time observations could not be ruled out, with forced photometry light curves in the left-hand panels and the scene modelling photometry light curves in the right-hand panels. The 5σ detections are shown as bins with solid uncertainty regions and bins with hashed uncertainty regions are non-detections. The object whose late-time detections are caused by the host galaxy AGN, SN 2019vzf, is shown in the bottom row. The colours are as in Fig. 3.9 with g band in green, r band in orange, and i band in red. 72

-
- | | | |
|-----|---|-----|
| 4.1 | The final sample split into nine classes. As there is a big difference in class sizes, the smaller groups have been put together in the left chart as ‘other’ and are split up in the right chart. | 104 |
| 4.2 | Sample size as a function of redshift for each class of objects. All objects with $z > 1$ are put together in the bin starting at $z = 1$. The histograms are split into two plots for better readability. In all classes of objects our sample is biased towards lower z | 104 |
| 4.3 | Examples of pre-ZTF SNe whose light curves have been recovered in the binned ZTF light curves. For each object we show the pre-ZTF g (dark green), r (dark yellow), and i (dark red) data points, as well as the binned ZTF detections (green, orange, red, respectively). The binned ZTF observations are in 25 day bins, with the width showing the beginning and end of each bin, and the shaded region shows its 1σ magnitude uncertainty. The pre-ZTF data was taken from Andrews et al. (2019) (SN 2017gmr), Brown et al. (2019) (SN 2017erp), Tartaglia et al. (2020) (SN 2015da), Zhu et al. (2023) (SN 2017egm), and Kuncarayakti et al. (2018) (SN 2017dio). None of the light curves are corrected for host extinction. | 110 |
| 4.4 | Light curve of AT 2017gpv with the axes representing absolute magnitude (left), apparent magnitude (right), the rest frame days since first detection (top) and mjd (bottom). Single epoch detections by ZTF, Gaia, Pan-STARRS and ATLAS are shown, as well as the binned ZTF observations after the transient faded below the single epoch noise limit. The dashed lines are the <i>gri</i> -band light curves of iPTF2014hls, which have been corrected for time dilation but not extinction (data taken from Arcavi et al. 2017; Sollerman et al. 2019). | 113 |
| 4.5 | The nine objects whose late-time detections required a more rigorous investigation. Each object is shown in absolute and apparent magnitude (left and right axes respectively) and rest frame days since first detection and mjd (top and bottom axes respectively). We show the binned ZTF data with the late-time detections as well as pre-ZTF detections from other surveys (Pan-STARRS, Gaia, ASASSN, PTF) where available. For SN 2017ige a heavily extinct ($E(B-V)_{\text{host}} = 1.2$ mag) light curve of SN 2020jfo is shown with dashed lines matching the late-time ZTF r -band detections. The objects are marked with the explanation for their late-time detections. | 118 |
| 4.6 | M_{CSM} as a function of the r -band absolute magnitude M for different assumptions of t (panels), T (shaded region), and F_R (colours). The five objects for which we estimate M_{CSM} in Sect. 4.3.4 have been marked in the panel that has t the closest to the detected signal. Decreasing shell thickness and temperature to mitigate M_{CSM} is effective, though there is a limit to far this can be done while keeping realistic values for F_R . . . | 121 |

- 4.7 Binned r -band observations of the objects whose late-time detections are consistent with a galaxy nucleus (see Table 4.4) and are potentially transient events unrelated to the original SN. Upper limits are shown with downward arrows. The r -band light curve of the slowly evolving ambiguous nuclear transient AT 2020ohl (ASASSN-20hx, Hinkle et al. 2022) is also shown for comparison. As the late-time signal in AT 2017fwf was found to be significantly offset from the SN location we show the processed light curve at the host nucleus location instead. 124
- 4.8 Binned flux of the recovered AGN. The flux is calibrated to a zeropoint at mag 30. The dashed lines show the baseline value for each object. Since the observations used to determine the baseline cannot be binned we show the unbinned data in the baseline region of each object, this region is marked by the black lines. Even though not all objects are properly sampled over the entire lifetime of ZTF, they all clearly show variability over long timescales. As these objects are always varying, it is impossible to do a baseline correction without the transient present. This causes some light curves to go below their baseline. Note that the values for AT 2017kas have been divided by 10 as the variability is so large. 141
- 4.9 Binned flux of the recovered variable stars. The flux is calibrated to a zeropoint at mag 30. The dashed lines lines show the baseline for each object. Since the observations used to determine the baseline cannot be binned we show the unbinned data in the baseline region of each object, this region is marked by the black lines. All three objects vary around their central values, but the amplitude varies widely between the ZTF bands. Note that the values for PTF10qpf have been divided by 100 as the variability is so large. 142

List of Tables

3.1	Initial sample size and its reduction in each step of the analysis process.	45
3.2	List of objects that passed the initial visual inspections.	59
3.3	Objects with a detected sibling transient.	63
3.4	Results of the additional tests for the ten promising objects. The host separation is given in " and converted to kpc using the redshift given in Table 3.2 and the same cosmology as was used in Section 3.2.4.4. In the final five columns the similarity of each SN Ia with a late-time excess is compared to different transient classes to see if the late-time signal can be interpreted as another transient. This can be excluded based on an inconsistent colour (1), duration (2), and/or an excessive amount of host extinction (3) needed to obtain the observed magnitudes.	67
3.5	Details of the comparison transients used to test if late-time detections could be explained by another transient at a similar sky position. The first column shows the assumed type of transient, the second shows the transients used to represent each type, the third has the approximate absolute extinction-corrected r -band peak magnitudes, and the fourth the reference for each event.	69
3.6	Parameters used for rate estimation simulations for each object.	82
3.7	Spectra used to make the SN 2011fe model. All spectra were taken from WISEREP (Yaron & Gal-Yam, 2012).	94
3.8	Redshift values where 50 per cent of the simulated SNe were found to have CSM interaction. Strength is the strength of the $H\alpha$ line compared to the strength detected in SN 2015cp. Start shows how many days after the peak the interaction begins, and duration is in days as well. I fitted sigmoid functions to the results of each simulation in order to find the redshift where 50 per cent of the interactions were recovered, assuming the reference images were of the same depth as the ones used in ZTF or 0.5 or 1 mag deeper. These values are shown in $z_{50} \pm \sigma_{z_{50}}$, and χ^2_{red} shows the quality of the fit.	97
4.1	Details of the three baseline regions used in our pipeline. The first column gives the start and end MJD of each baseline region, and the second column gives its length in days. The last three columns give the number of transients that had at least 30 points in the baseline to provide a robust estimate of the baseline, in the g , r , and i band, respectively .	108

4.2	Pre-ZTF transients with a sibling transient detected in ZTF in single exposures. The first four columns give the name, type, discovery mjd, and redshift of the pre-ZTF transient, and the next five columns give the same information of its ZTF sibling when available. The second to last columns gives an estimate of the peak r -band (unless specified otherwise) absolute magnitude of the ZTF transient assuming the pre-ZTF transient redshift, except for AT 2018iml as this is likely a foreground CV. The last column gives the separation between the siblings. A ? type means the transient was never spectroscopically classified. IAU names in parentheses are ZTF transients wrongly associated with a pre-ZTF transient.	114
4.3	Pre-ZTF transients detected in the binned ZTF light curves due to AGN or variable star activity. The original type and z values are as they were recorded on the OSC or WISEREP. The late-time type gives the reason for the ZTF detections.	117
4.4	Objects with detections whose origin was not immediately clear. The first five columns give information on the original transient, and the last six columns give an overview of the binned ZTF detections. Start gives the time after discovery of the first detections in ZTF, and duration gives the length of these detections. Both are in rest frame days and rounded to 10 days. The g , r , and i columns give the range of detections in absolute magnitude if detected. Inferred cause of excess gives the type of object that best explains the detections. The last two columns state whether the excess is consistent with the SN and host nucleus location, respectively.	119
4.5	Number of recovered signals for each SN type in our sample. As it is unclear whether SN 2016cob and SN2017fby should be counted as nuclear transients or due to CSM interaction, they have been counted in both.	130
4.6	List of the 63 pre-ZTF objects whose tail is still visible in ZTF using our binning method after a baseline correction.	138

Introduction

1.1 The final stages of stars

Stars are big balls of plasma that is gravitationally bound together. Consisting of primarily hydrogen upon first formation, the extreme heat and pressure in their cores allows stars to fuse hydrogen into helium, which generates the energy needed to maintain hydrostatic equilibrium and prevent further gravitational collapse. [Kippenhahn et al. \(2013\)](#) gives an excellent and detailed review of the evolution of stars in different mass ranges. When the hydrogen supply is depleted the inward pressure from gravity causes the core to contract until something is able to stop it once more. This can be matter in the core turning degenerate and providing an electron degeneracy pressure, or the start of helium fusion. What happens next, and the ultimate fate of a star depends on its mass.

1.1.1 Stars below $8 M_{\odot}$

The lightest stars have a theoretical lifespan that is larger than the current age of our universe, and as such the final stages of their evolution cannot be observed yet. The outer layers of stars with a mass between $0.6 M_{\odot}$ and $8 M_{\odot}$ increase dramatically, and they become red giants as they fuse helium into carbon and oxygen in their cores and hydrogen in a shell around the core. Eventually the outer layers are blown away while the core is left behind to cool down and become a white dwarf (WD).

WDs are degenerate objects primarily made up of carbon and oxygen. As electrons are fermions, the Pauli exclusion principle ([Pauli, 1925](#)) forces each one to occupy a different quantum state. Due to their high density in the WD, electrons become degenerate as they are forced in higher energy states. The degenerate electron gas provides a pressure that is independent of temperature, allowing the WD to theoretically cool to absolute zero without any significant change in the stellar structure (although some

models predict WDs to crystallise at a certain temperature, [Mochkovitch 1983; Isern et al. 1997](#)). Assuming that the electron gas is non-relativistic, it can be shown that the radius of a WD is related to its mass as

$$\frac{R_{\text{WD}}}{R_{\odot}} = 0.010 \left(\frac{M_{\odot}}{M_{\text{WD}}} \right)^{1/3}, \quad (1.1)$$

with R_{WD} the radius of the WD and M_{WD} its mass. This shows that WDs are roughly planet sized, and that more massive WDs are smaller. As the mass increases however, the electrons in the WD become relativistic and Equation 1.1 is no longer valid. In this case the radius decreases much more drastically with increasing mass, up to the limit of

$$M_{\text{Ch}} \approx 1.4M_{\odot}, \quad (1.2)$$

which is the so-called Chandrasekhar limit ([Chandrasekhar, 1931](#)). A WD at the Chandrasekhar mass M_{Ch} has a radius of 0, and the electron degenerate pressure cannot stop a WD from collapsing in on itself.

1.1.2 Stars above $8 M_{\odot}$

More massive stars are able to burn the carbon that is left after burning helium. New elements get created and subsequently burned under increasingly more extreme conditions, resulting in a core which is structured like an onion. Each ring consists of a different fusion product, with heavier elements towards the core. Figure 1.1 shows a schematic view of the layered structure of a highly evolved massive star. Each stage of fusion is less efficient, and once iron is reached it further fusion consumes energy rather than releasing it. The core becomes unstable to support itself and collapses into a neutron star or black hole, depending on the mass of the star. The outer layers fall inwards but bounce back and gains enough energy to become unbound from the star. Additionally the high densities allow for elements heavier than iron to be fused in these brief moments. The stellar demise is known as a core collapse supernova (CCSN).

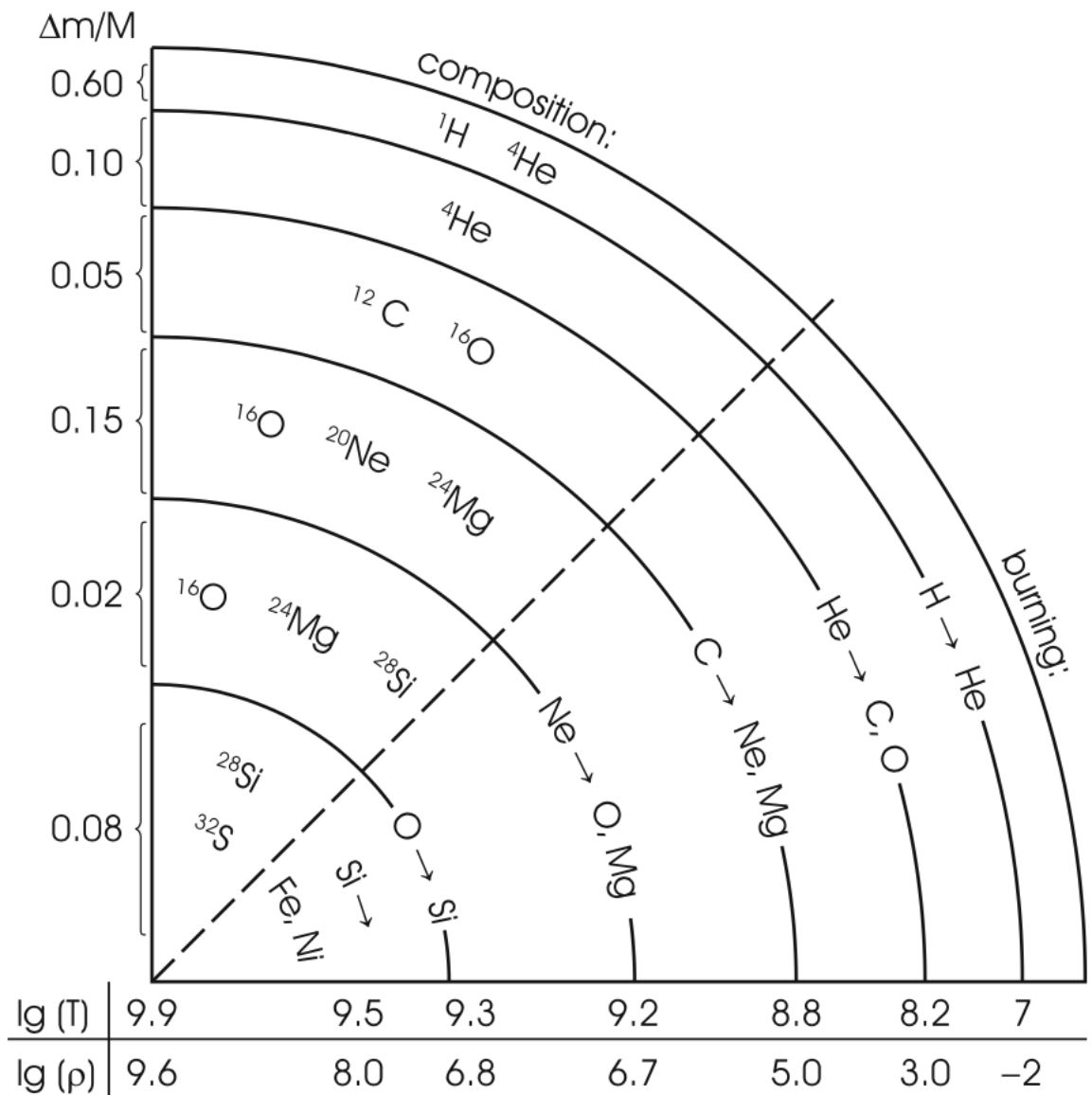


Figure 1.1: Schematic view of the onion structure of a highly evolved massive star just before core collapse, with light elements on the outside and heavier elements towards the core. Typical values are given along the horizontal and vertical axes. This figure originally comes from chapter 35 of Kippenhahn et al. (2013).

Section 1.2.1 contains more details on these events.

1.2 The transient universe

Astronomy is a field filled with large scales, and when studying processes that change over time our limited time-span to observe often prevents us from studying a single object through its entire evolution. From formation of stars and planets to the evolution of galaxies and the cosmic web, these occur on such long time scales that a human life is just a blip. From our perspective we only have a snapshot of the state of each object, and it is through the combination of a large ensemble of objects together with theory and simulations that we are able to understand the bigger picture.

Transients are, by definition, fleeting things, and in extrasolar astronomy these are objects or events that occur on short timescales of mere hours to a few years. This means we are able to observe the entire evolution of a single object, as long as it is discovered early. The most famous examples of transients are supernovae (SNe), exploding stars at the end of their life releasing enough light that they can outshine their entire host galaxy for a few weeks to months before fading away again.

Figure 1.2 is a *gri* composite image of NGC4216, taken with the Zwicky Transient Facility (ZTF, see Section 2.2.1). The left image is made using data before the start of 2024, the right image is made using data from Januari 2024 and clearly shows an extra source in the southern part of the galaxy. This is SN 2024gy, a Type Ia SN (see Section 1.2.2) first discovered on 4 Jan 2024 ([Itagaki, 2024](#)). Despite the galaxy being at a distance of 16.194 ± 0.491 Mpc ([de Vaucouleurs et al., 1991](#)) the SN still outshines the Milky Way stars that are in the same image.

1.2.1 Core Collapse Supernovae

As was mentioned at the end of Section 1.1.2, stars above $8 M_{\odot}$ end their lives in a CCSN when the core implodes into a compact object due to the effects of gravity. The outer layers fall in as well but bounce back outwards as the enormous amounts of



Figure 1.2: *gri* composite image of NGC4216 using observations taken by the Zwicky Transient Facility. **Left:** composite image of observations taken before 1 January 2024. **Right:** composite image of observations taken between 5 and 19 January 2024, the first two weeks after the first detection of the Type Ia SN 2024gy. (Credit: Benjamin Nobre Hauptmann)

released gravitational energy from the collapsing core is imparted on the outer layers, heating them up and expelling them outwards at high velocities. The light coming from the cooling of this material and the radioactive decay of newly formed unstable nuclei into stable ones cause the SN to rise rapidly in brightness. Within hours after the explosion it is bright enough to be observed in other galaxies, peaking after several days to weeks at an absolute magnitude in the range of -16.5 Mag to -18.5 Mag depending on the type of CCSN ([Richardson et al., 2014](#)). This is what we observe as the supernova event, and by analysing their spectra they can be classified based on the visible elemental emission and absorption lines.

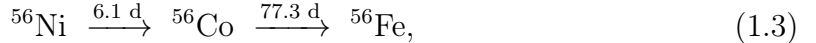
The composition of the outer layers of the progenitor star depend heavily on the life of the star. Most CCSNe have hydrogen in their envelope, which will show up in the SN spectra as strong Balmer emission lines. These are known as Type II SNe. Photometric features of the light curve, the SN brightness as it changes over time, are also used in SN identification, leading to subtypes such as SN IIL or SN IIP for Type II SNe that show a linear decline or a plateau, respectively. High mass-loss rates, due to the stars metallicity or the presence of a binary companion, can however strip the hydrogen layer leaving the helium shell as the outermost part of the progenitor at the moment of core collapse which results in a SN without H lines but with He lines in their spectra that are known as Type Ib SNe. In some extreme cases even the helium layer has been stripped away, resulting in SNe without H or He lines in their spectra, known as Type Ic SNe. Transitional objects, where a layer is mostly but not completely stripped, are also known ([Alsabti & Murdin, 2017](#)).

Photometric classification is cheaper as photometry is easier to obtain, but it cannot differentiate between subtypes that are defined on the presence, strength, or absence of specific elemental lines, leading to broader classifications with less certainty. Besides this, many of the differences that make certain SNe interesting are visible at early times, while a SN needs to evolve up to a certain point to have a light curve that is long enough to allow classification. For these reasons a common strategy is to use dedicated large-scale surveys such as the Zwicky Transient Facility (ZTF, see Section

[2.2.1](#)) to find new SNe within days after explosion using photometry, and using different telescopes to follow these up with spectroscopy for classification.

1.2.2 Thermonuclear SNe

Besides CCSNe are the more common thermonuclear SNe (Type Ia SNe, SNe Ia), which are exploding WDs after fusion in their core has been ignited through some mechanism (see Section [1.3](#)). The more massive the WD, the easier it is to ignite as the nuclei are forced closer together. Since the WD is degenerate the energy released by a single fusion event can completely be used to heat up the surrounding material and let it fuse as well, leading to a runaway process where the entire WD tries to fuse to iron-peak elements on a timescale of seconds. This process disrupts the entire star, expelling the material outward at relativistic speeds ([Hoyle & Fowler, 1960](#)). Not all carbon and oxygen is fused, but most of the mass ends up in ^{56}Ni , with typical SNe Ia producing between $0.3 - 0.8 M_{\odot}$ of ^{56}Ni ([Stritzinger et al., 2006](#)). This is an unstable nucleus and decays as



with ^{56}Fe being the stable end product of the decay chain. The key spectral signatures of a SN Ia are the absence of hydrogen lines (hence the Type I classification), and broad Si II absorbtion features. At first the ejecta are dense and opaque, and only photons from the outer layers can escape. As the ejecta expand they become more transparent, and the slower moving inner layers become visible as the photosphere recedes back inwards. Therefore, by taking spectra at different phases a map of the elemental abundances in velocity space can be built. [Rewrite the spectra part, doesn't feel right, needs refs](#)

The SN reaches peak brightness around three weeks after the explosion and starts to fade again. The main powersource that governs the rate at which the SN fades is the decaying ^{56}Ni , resulting in a linear decline of the light curve in magnitude space. In the near infrared there is a second peak a few weeks after the first, which is suggested

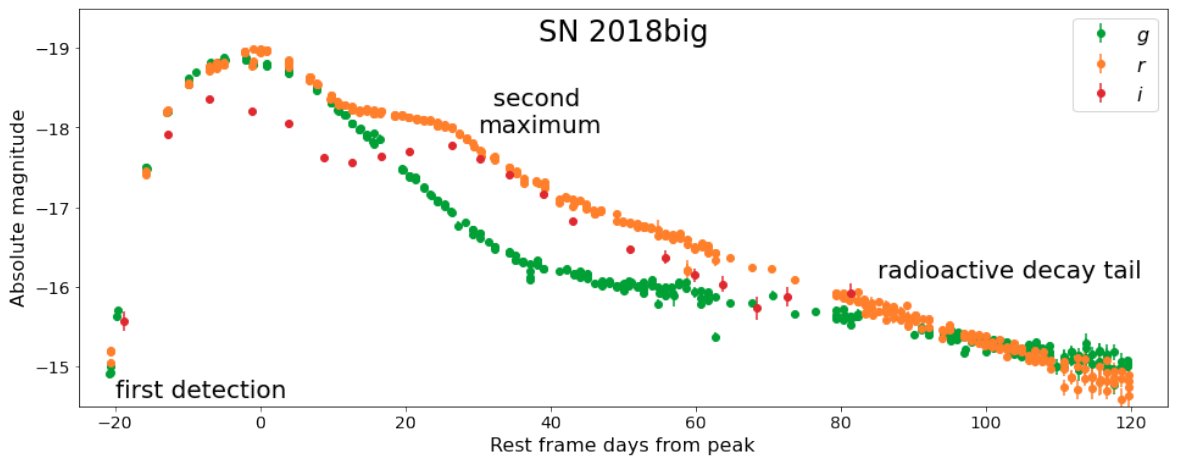


Figure 1.3: *grilight* curve of a SN Ia in the rest frame and at absolute magnitude, corrected for Milky Way extinction but not for host extinction. The *g*-band clearly shows a change in the decline rate as ^{56}Co decay becomes dominant over ^{56}Ni decay. The *r* and *i*-band show the second peak. This light curve is made using ZTF observations.

to be the result of a decrease in opacity due to the changing ionization state of iron group elements (Kasen, 2006). Figure 1.3 shows an example of a well-observed normal SN Ia.

1.2.2.1 Standardizable candles

A WD with a mass of $\sim 1.37M_{\odot}$ has high enough pressure and density in its core for carbon to ignite, triggering a thermonuclear runaway process that results in the SN Ia explosion. Most WDs tend to explode in a very similar way, which results in very similar light curves that peak around an absolute magnitude of -19.5 Mag, making them brighter than CCSNe. Some SNe Ia become brighter than others, but they also evolve slower. This is called the Phillips relation (Phillips, 1993), and it can be used to infer the absolute peak brightness based on how fast it evolves. Tripp (1998) improved the standardization by adding a second term, the so called colour luminosity term. This accounts for the intrinsic SNe Ia colour and as bluer SNe Ia are brighter. These days there is a third term, which accounts for environmental dependencies and is implemented as a step function (Kelly et al., 2010; Sullivan et al., 2010). The resulting standardisation formula is given by

$$\mu_{\text{obs}} = m_B - M_0 + \alpha x_1 - \beta c - \gamma p, \quad (1.4)$$

where μ_{obs} is the observed distance modulus. m_B and M_0 are the apparent and absolute B-band magnitude, respectively. x_1 is the SN stretch, c its colour, and α and β are the coefficients used to correct for these effects. γ is the size of the step function and p determines when this step needs to be applied.

Using the standardisable nature of SNe Ia allows their distance to be measured, as well as the distance between Earth and the host galaxies they reside in. At the same time the redshift of the host galaxy can be measured from the spectra, and with these values together the Hubble constant H_0 , which measures the expansion rate of the universe, can be measured. According to one of the latest measurements made by the SH0ES team (Riess et al., 2021) using the Pantheon+ sample (Scolnic et al., 2021) the universe expands at a rate of $H_0 = 73.30 \pm 1.04 \text{ km s}^{-1} \text{ Mpc}^{-1}$.

1.2.3 Other types of transients

There are other types of transients besides SNe. Some SNe become much brighter than normal events and are therefore called superluminous SNe (SLSNe). Supermassive black holes (SMBHs) in the center of galaxies can cause a variety of transient events such as tidal disruption events (TDEs) or ambiguous nuclear transients (ANTs), or a galaxy could have an active galactic nucleus (AGN). Some types of stars also pulsate and vary in brightness over time. All of these can show up transients in surveys looking for changes in the night sky on a day-to-day basis.

1.2.3.1 SLSN - Superluminous Supernova

SLSNe are SNe that have a higher peak luminosity than normal SNe, in some cases reaching over 5 magnitudes brighter than normal events at their peak (Gal-Yam, 2019). Like normal SNe they can be classified into Type I and Type II based on the absence of presence of hydrogen emission lines in their spectra. One of the main puzzles regarding these types of events is the source that powers their superluminous nature. Different types of models have been put forward, using magnetars (Maeda et al., 2007), black holes (Dexter & Kasen, 2013), radioactivity (Kasen et al., 2011), or interaction with

circumstellar material (CSM) (Yan et al., 2017) to push the brightness significantly above that of regular SNe. Each of these has different strengths and weaknesses.

1.2.3.2 AGN - Active Galactic Nucleus

An AGN is the central region of a galaxy in which a SMBH accretes matter at a high rate, releasing a part of the potential energy as heat and radiation. As a result of this the AGN has a very high luminosity compared to the rest of the galaxy, with different orientations of the system resulting in different types of AGN (Antonucci, 1993; Urry & Padovani, 1995). As the stream of matter being accreted is inhomogeneous, the accretion rate and luminosity change over time. In some cases AGN variability is so extreme that it changes the entire spectrum of the AGN, with (dis)appearing broad emission lines and continuum flux. These are so called changing-look AGN (CL-AGN) (see Ricci & Trakhtenbrot, 2023, for a review). AGN variability can be used to estimate the SMBH mass through reverberation mapping (Wandel et al., 1999; Peterson & Horne, 2004). Fast moving clouds close to the AGN change the strength of line emission based on how strongly they are illuminated by the AGN. The delay between a luminosity change in the AGN continuum and the broad emission line features coming from these clouds gives a measure of their distance, while the width of the emission lines give a measure of their velocity. From these measurements the SMBH mass can be estimated using Kepler's third law.

1.2.3.3 TDE - Tidal Disruption Event

In some cases a star can get too close to the SMBH and get tidally disrupted (Rees, 1988; Strubbe & Quataert, 2009). In a TDE the star gets ripped apart due to the strong gravity of the SMBH and forms an accretion disk of hot gas that gets accreted onto the SMBH. The distance at which the TDE occurs depends largely on the SMBH mass, and for SMBHs more massive than $\sim 10^8 M_\odot$ the tidal disruption radius lies within the event horizon, meaning that TDEs cannot be observed around the most massive SMBHs (Hills, 1975). The other dependency of the tidal radius is the difficulty to

disrupt a star. Compact objects such as WDs are very difficult to disrupt and thus have a smaller tidal radius. A red giant on the other hand has outer layers that are very loosely bound to the star and is therefore easier to disrupt at a larger radius, though this might also result in a partial tidal disruption where only the outer layers are stripped while the stellar core survives the encounter. TDEs can become brighter than SNe, with the brightest event ever observed being AT 2021lwx (ZTF20abrbeie, nicknamed "Scary Barbie"), which is thought to be the disruption and accretion of a giant molecular cloud ([Subrayan et al., 2023](#); [Wiseman et al., 2023](#)).

1.2.3.4 ANT - Ambiguous Nuclear Transient

Some nuclear variability does not quite fit the known classes of AGN or tidal TDEs, showing characteristics of both types of events. These events have been named ambiguous nuclear transients (ANTS; [Kankare et al., 2017](#); [Hinkle et al., 2022](#); [Hinkle, 2024](#); [Hinkle et al., 2024](#); [Wiseman et al., 2024](#)) and rise up quickly, reaching peak brightness within a few weeks before declining very slowly over hundreds of days, although their decline rates are variable.

1.2.3.5 Variable stars

Some stars show variability as well, with the brightness of certain types of stars oscillating by a magnitude or more. The most famous class of variables are Cepheids, whose regular oscillation period of the order of days is related to their absolute magnitude. They are bright enough to be visible in nearby galaxies, which makes them useful to calibrate SN Ia distance measurements when building the distance ladder ([Gibson et al., 2000](#); [Saha et al., 2006](#)). Other types of stars, such as Mira variables, are much more extreme in their change of brightness and have periods > 100 days ([Bedding & Zijlstra, 1998](#)).

1.3 SN Ia progenitor systems

Section 1.1.1 states that WDs are stable objects, but Section 1.2.2 states that WDs explode in SN Ia explosions. These two statements seem to disagree with each other, as a stable object is not expected to suddenly explode. This observation is correct, WDs do not explode. At least, not by themselves. However, not all stars are single, and those that in a binary system can under certain conditions interact with the other star and start accreting matter coming from the so-called donor star. As the radius of a WD is inversely proportional to its mass (Equation 1.1), it will shrink as it becomes more massive until the point is reached where fusion is ignited in the core of the WD triggering its explosion.

The obvious thing to do is to ask what kind of star the donor is. Assuming that the stars have been in the binary system since formation and since more massive stars have a shorter lifespan, the more massive star has turned into the WD. This means that the donor has to be $< 8 M_{\odot}$ (though due to stellar and especially binary evolution the mass of the donor has likely changed since formation). Other than this there are many possible options, the donor could still be in its hydrogen burning phase or have evolved to the later stages in its life up to and including becoming a WD as well. This is called the progenitor problem, and it is currently still being debated. Different progenitor scenarios can broadly be put into one of two categories based on whether the donor star is a compact object (double degenerate) or not (single degenerate). Artistic impressions of these two scenarios are shown in figure 1.4.

1.3.1 Single degenerate

The most straightforward and classical way to explode a WD is by adding mass to a near M_{Ch} WD until carbon is ignited in the core due to compressional heating. The companion star fills its Roche lobe and material from the outer layers is syphoned onto the WD. The donor can fill its Roche lobe while it is still a main sequence star, when it has evolved into a red giant, or it may even be a helium star whose hydrogen layer

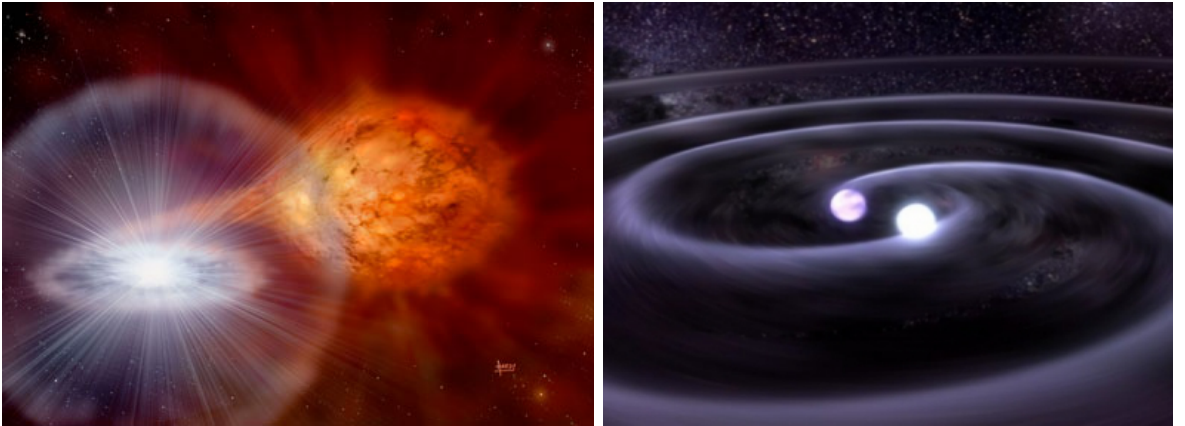


Figure 1.4: **Left:** Artistic impression of a single degenerate system, where the white dwarf accretes material coming from the surface of the donor star. Image credit: STFC / David Hardy. **Right:** Artistic impression of a double degenerate system where two white dwarfs spiral in to each other while releasing gravitational waves. Image credit: NASA / Tod Strohmayer (GSFC) / Dana Berry (Chandra X-Ray Observatory).

has been stripped due to binary interactions ([Whelan & Iben, 1973](#); [Nomoto, 1982](#)). In delayed-detonation models the WD first expands during a deflagration phase, which then transition into a detonation after the WD becomes unbound ([Khokhlov, 1991](#); [Mazzali et al., 2007](#)).

In non-classical models a sub- M_{Ch} WD can explode by first slowly accreting and building up a layer of helium on its surface, which explodes after a sufficient amount of material is gathered. As this explosion wraps around the outside of the WD it sends a shockwave into the interior of the star, which culminates near the center and temporarily increases the local pressure. If this is enough to ignite carbon fusion, the second detonation is triggered which disrupts the star and results in the main SN ([Taam, 1980](#); [Livne & Arnett, 1995](#); [Shen & Bildsten, 2009](#); [Fink et al., 2010](#)).

It is also possible that the WD and red giant companion enter a common envelope phase. The WD merges with the hot core of the red giant forming a rapidly rotating, WD-like degenerate core with $M_{\text{core}} > M_{\text{Ch}}$ inside the red giant. The angular momentum prevents the core to collapse in on itself but is gradually lost until it can no longer support itself, triggering the SN Ia explosion in the so-called core degenerate scenario ([Kashi & Soker, 2011](#)).

1.3.2 Double degenerate

If both objects are WDs the primary (more massive) WD can still accrete material from the secondary WD in a stable Roche lobe overflow scenario ([Piersanti et al., 2003b,a](#)). In other scenarios the WDs fully merge, either dynamically or violently. In the dynamical scenario the WDs lose angular momentum as it is radiated away through gravitational waves ([Iben & Tutukov, 1984](#); [Webbink, 1984](#)). An artist impression of this scenario is given on the right side of figure 1.4. As the WDs come closer the less massive companion fills its Roche lobe and material starts flowing onto the primary. As the companion loses mass its radius increases, leading to more mass loss until the entire star is disrupted. Around half of the material forms a disk around the surviving WD while the rest falls directly onto its surface, very little material is expected to be flung out of the system. As the system evolves further it eventually explodes in a SN Ia.

In collisions or violent mergers of two WDs a detonation can occur during the merger at the location of the accretion stream due to its high density and temperature ([Rosswog et al., 2009](#); [Pakmor et al., 2010, 2012](#)). This might either directly start carbon fusion at the ignition site or cause a surface explosion that again wraps around the WD and compresses its interior causing a second ignition, depending on the system and WD masses. The asymmetry of this system when it explodes is expected to cause significant asymmetry in the ejecta and its composition in different directions. This is expected to lead to different amounts of polarization of the SN light, depending on the angle between the plane of rotation and the line of sight ([Wang et al., 2007](#); [Bulla et al., 2016](#)).

1.4 Subclasses

As has been stated in Section 1.2.2.1, most SNe Ia explosions evolve in a very similar way with a tight relation between their peak, colour, and rate at which they evolve. These are called normal SN Ia, or SN Ia-norm. This name suggests the existence of

abnormal SNe Ia besides the normal ones. This is indeed the case, in fact there is an entire zoo of subclasses that have photometric and / or spectroscopic differences from SN Ia-norm. [Taubenberger \(2017\)](#) showed the different subclasses of SNe Ia together by plotting their peak absolute B-band brightness as a function of $\Delta m_{15}(B)$, which is the difference in brightness in the B-band between the SN at peak brightness and 15 days after the peak in the SN rest frame expressed in magnitudes. This plot is also shown in Figure 1.5.

Recently, [Dimitriadis et al. \(2024\)](#) made a similar plot but in the *g*-band, using the carefully curated sample of SNe Ia from the Zwicky Transient Facility’s second data release (ZTF SN Ia DR2, [Rigault et al., 2024](#), Smith et al., in prep.). They show that $\sim 75\%$ of all SNe Ia are normal events that can be standardized and used for distance measurements. After that the two largest subclasses are SN Ia-91T ($\sim 12\%$) and SN Ia-91bg ($\sim 6\%$), leaving a final $\sim 7\%$ as the combined total of various other subclasses of SNe.

Different subclasses have a preference for different environments. By studying the various different subclasses, the characteristic properties of their light, and the connection to their environments, we can learn more about the properties of their progenitor systems and the exact mechanisms that are involved in SN Ia explosions.

1.4.1 Photometric differences

The Phillips relation is easily visible in Figure 1.5, and SNe Ia-norm lie in a narrow strip around it. Most subclasses can be distinguished from SNe Ia-norm by photometry alone. The (aptly named) fast decliners fade unusually quickly after reaching peak brightness, while SNe Ia-CSM barely fade at all in the first few weeks after reaching their peak brightness. SNe Iax never reach the peak brightness of a normal SN Ia, which in some models is explained through the explosion failing to fully disrupt the WD ([Jordan et al., 2012; Kromer et al., 2013](#)). Super-Chandrasekhar SNe Ia on the other hand are brighter than what would be expected from a M_{Ch} WD explosion. Many subclasses are named after a prototypical SN that defines the subclass.

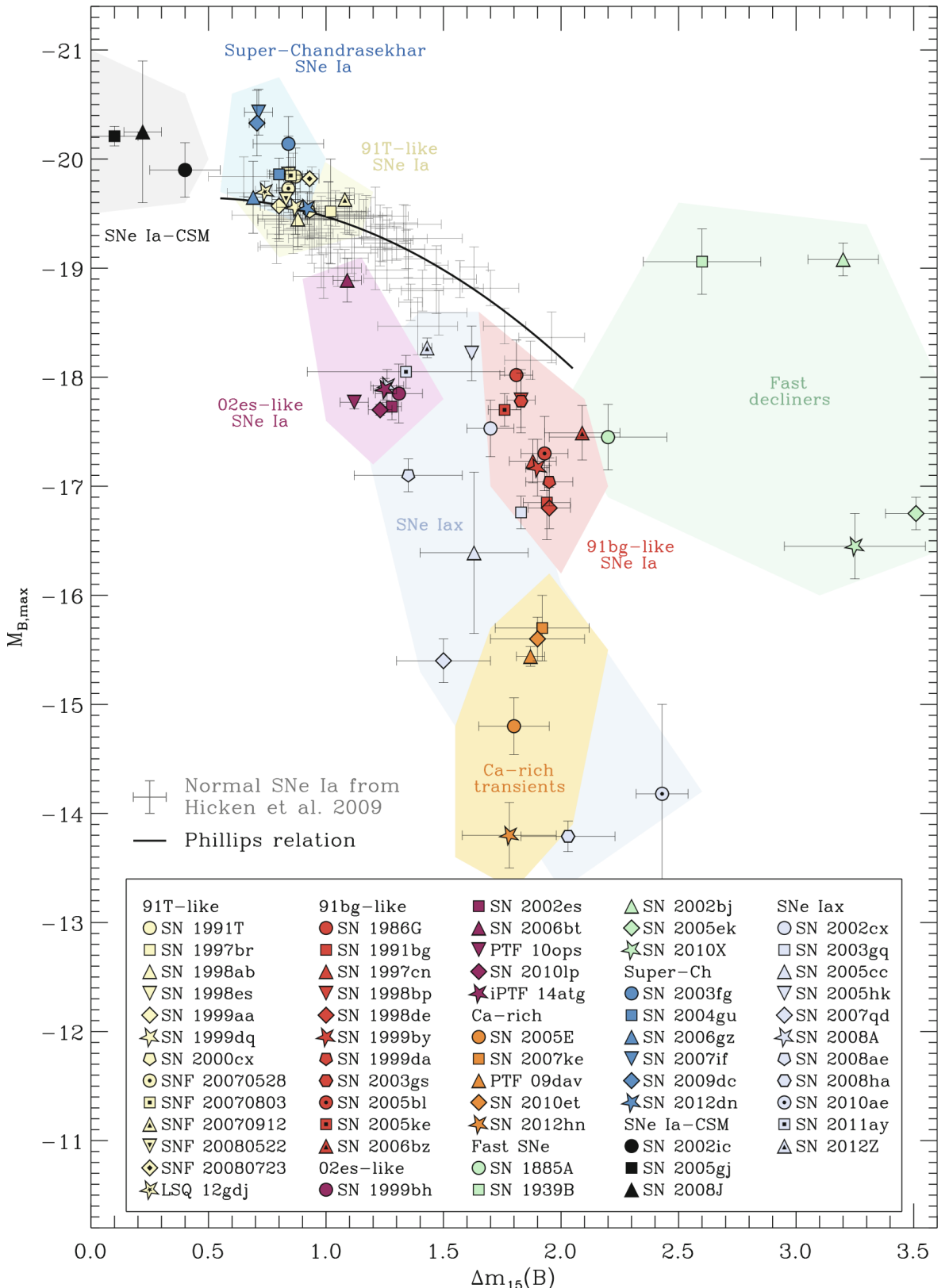


Figure 1.5: Subclasses of SNe Ia. The peak absolute B-band magnitude is plotted as a function of Δm_{15} in the same band. Normal SNe Ia lie along the Phillips relation, which is shown with a black line. Most of the non-normal subclasses can be separated from normal SNe Ia based on these two values alone. The only exception are the 91T-like SNe, which form a subclass based on their spectral differences from normal SNe Ia. This figure was taken from Taubenberger (2017).

1.4.2 Spectroscopic differences

Besides photometric differences, most subclasses are also spectroscopically different from SNe Ia-norm. Some have stronger emission lines of particular elements, others have weaker ones. Ca-rich transients (e.g. Perets et al., 2010; Kasliwal et al., 2012; Frohmaier et al., 2018) show Ca II emission lines in their nebular spectra that are much stronger than for other SN Ia types. The spectra of super-Chandrasekhar SNe show that their ejecta move considerably slower compared to other subclasses, which together with their high luminosity is consistent with a double degenerate merger scenario (Howell et al., 2006; Hicken et al., 2007; Yamanaka et al., 2009).

The SN Ia-91T subclass lies at the bright end of the Phillips relation, and thus cannot be identified photometrically but can therefore be normalized and used for distance measurements. Spectroscopy however reveals that this subclass evolves differently as it rises towards peak brightness, showing a blue pseudo-continuum with two strong Fe III absorption multiplets instead of intermediate mass element lines. They also have a preference for younger stellar populations (Filippenko et al., 1992; Ruiz-Lapuente et al., 1992), although this preference is not seen in Dimitriadis et al. (2024).

1.5 SNe with circumstellar material

The progenitor system of a SN is not completely isolated. Through various mechanisms a significant amount of material can end up close to the explosion site before the explosion occurs. This is called circumstellar material (CSM), and as it is usually originated from the progenitor system, CSM can give new insights in the history of the progenitor system and the sequence of events that led it to explode.

Ejecta from the SN explosion are expelled at high velocities and quickly catch up with the often much slower moving CSM. As the ejecta slam into the CSM shockwaves are produced and energy is deposited into the CSM, which starts to emit light of its own. This new light source alters the light curve, making it brighter and slowing or even stalling its decline. CSM interaction also shows up in the spectra as the emergence

of narrow emission lines that give clues about the composition of the slower moving material. Eventually the ejecta overtake the CSM and its signal fades as the CSM is swept up.

Another way in which the presence of CSM has been inferred is through the presence of narrow absorption lines that vary with time, indicating that they evolve alongside the SN (e.g., Ferretti et al., 2016; Soker, 2015). However, these absorption lines are not always seen and their behaviour varies from object to object, making it difficult to interpret them consistently. Light echoes can also provide an opportunity to study circumstellar and interstellar material, though the difficulty to geometrically separate them from the SN location, combined with their weak nature makes this only possible for SNe in the Milky Way or nearby galaxies (Patat, 2005; Krause et al., 2008; Graur et al., 2016).

1.5.1 The SN Ia-CSM subclass

SNe Ia-02ic, or SNe Ia-CSM, are the subclass of thermonuclear explosions that show signs of CSM interaction. This often shows up as a peculiar long-lived light curve along with narrow Balmer emission lines, which is a clear indicator of this signal coming from CSM as SNe Ia are expected to be hydrogen-poor. The prototypical event, SN 2002ic, showed narrow H α and H β lines, and the slowly declining light curve was found to be consistent with $\sim 1.3 M_{\odot}$ of CSM (Hamuy et al., 2003a,b; Wood-Vasey et al., 2004; Nomoto et al., 2005).

Currently there are several dozen known SNe Ia-CSM (Aldering et al., 2006; Silverman et al., 2013; Sharma et al., 2023). In all cases the interaction started within two months after the explosion, leading to their (re-)classification after spectroscopic confirmation. The amount and duration of interaction varies quite significantly from one object to another. While some members such as SN 2018gkx and SN 2020xtq mainly feature an unusually slow decline rate, other objects such as SN 2020aekp have a plateau for several 100 d before starting to fade away slowly (Sharma et al., 2023).

The CSM could be created by different mechanisms depending on the progenitor

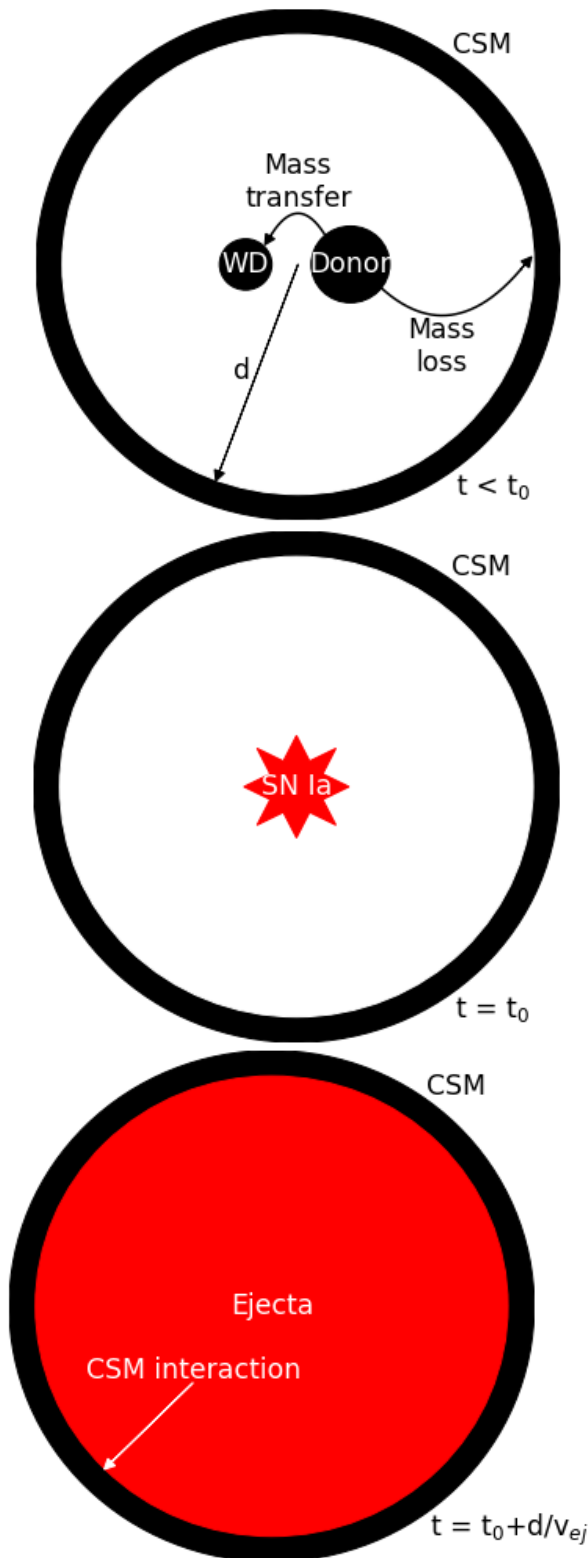


Figure 1.6: Schematic view of a SN Ia-CSM event. **Top:** The progenitor system containing a WD feeding on material from the donor star. Through various mechanisms a fraction of this material can be lost from the system and end up as CSM in a disk or shell at a distance d around the progenitor system. **Middle:** The WD explodes as a SN Ia. This can be a SN Ia-norm or a peculiar object, depending on the progenitor system. The ejecta start traveling outwards from the explosion site. **Bottom:** The ejecta catch up to the CSM and start interacting with it, causing the CSM to start emit light as well as it is swept up. This results in a slowing down of the photometric light curve decline and narrow emission lines in the spectra. **Needs aligning**

system, and its composition depends on the type of donor star present. In the single degenerate scenario, CSM rich in hydrogen can be created by a WD generating a fast wind, blowing away a part of the material it received from the mass transfer (Nomoto et al., 2005). In the double-degenerate scenario, part of the tidally disrupted secondary WD becomes unbound from the system, creating (H-poor) CSM and may be able to produce detectable signatures depending on the time between the tidal disruption and the SN Ia explosion (Raskin & Kasen, 2013). The core degenerate scenario could provide a massive amount of hydrogen-rich material near the explosion site (e.g. for SN 2014J, Soker, 2015), though the signatures of this scenario could be ambiguous with interacting SNe IIn, leading to confusion (Inserra et al., 2016a). Tsebrenko & Soker (2015) proposed that the core degenerate and double degenerate scenarios could lead to SNe Ia exploding inside planetary nebulae, possibly resulting in observable time-varying sodium absorption lines or CSM interaction.

Figure 1.6 shows a schematic view of the creation of a CSM shell (or ring depending on how mass is lost from the progenitor system) and the subsequent interaction between the CSM and SN ejecta. When the SN explodes the ejecta will initially expand within the gap between the progenitor system and the CSM, and its spectrum will look like that of a non-interacting class of SN Ia that may or may not display absorption features caused by the CSM if it is in the line of sight. Compared to the ejecta which are traveling at v_{ej} the CSM is practically stationary but at a distance d from the explosion site. This means that the ejecta need a time $t = d/v_{ej}$ to reach the CSM and start to interact with it. Only then does the event transform into a SN Ia-CSM with new narrow emission lines. This later transformation explains why in some cases objects are re-classified as Ia-CSM after first being classified as something else (e.g. SN 2020aekp, which was first classified as a SN Ia by Dahiwale & Fremling 2021 but reclassified as a SN Ia-CSM by Perley et al. 2021).

SN 2011km (PTF11kx) is a well observed Ia-CSM event, and shows signs of a complex CSM consisting of multiple shells with which the SN ejecta interact. Dilday et al. (2012) show that its photometry is similar to 91T-like objects before the CSM

interaction begins, and explain SN 2011km using a symbiotic nova progenitor system. [Leloudas et al. \(2015\)](#) also suggested a link between SNe Ia-91T and SNe Ia-CSM as they show similarities in their peak brightness and spectroscopy before the start of the interaction. In some cases, a 91T-like SN could start interacting with CSM hundreds of years after the explosion, like as has been suggested for Kepler's SN [Patnaude et al. \(2012\)](#); [Katsuda et al. \(2015\)](#).

Another interesting Ia-CSM is SN 2020eyj, which [Kool et al. \(2023\)](#) present as the first detection of a Ia-CSM interacting with He-rich material. Up until then all members of the subclass had shown strong H α emission and weak He signatures. SN 2020eyj, however, showed little to no H present in the CSM. This suggests that the progenitor system contained a He star. This was also the first time a SN Ia was detected in the radio. Non-detections in normal SNe Ia suggest a clean environment for the ejecta to expand in, while in this case there is a lot of material present.

1.5.2 CSM in CCSNe

Some CCSNe show interaction with CSM as well, the events are subclassified as SN IIIn, SN Ibn, or SN Icn, due to the narrow emission lines. As stated in Section 1.2.1 the difference between these three main types of SNe is the amount of material that has been stripped prior to explosion. Mass can be lost through binary interaction, but massive stars have also been known to have strong stellar outflows and winds. The existence of Wolf-Rayet stars shows that very massive stars can lose their entire hydrogen envelope, and they are thought to be one of the very last stages in the life of the star before it explodes in a SN Ib or SN Ic ([Groh et al., 2013](#); [Gal-Yam et al., 2022](#)).

The CSM is often resides close to the progenitor and can be thick enough to obscure features of the underlying SN, depending on the geometry and orientation of the system ([Chugai et al., 2004](#); [Smith et al., 2015a](#)). The short distance between the SN and CSM suggest that the material was ejected recently, and in some cases precursor events have been observed prior to the final SN explosion (e.g. SN 2011ht, [Fraser et al. 2013](#)

and SN 2020pvb (Elias-Rosa et al. 2024). CSM residing close to the progenitor causes most CCSNe to show signs of CSM interaction almost immediately after the explosion. However, examples of the interaction starting much later have been found as well, suggesting that their CSM has been ejected a long time ago (Miller et al., 2010; Fox et al., 2013).

Recently, SN 2021yfj was discovered to be a new type of SN and given the classification of SN Ien. This object showed highly ionized silicon, sulphur, and argon lines but barely any carbon, oxygen, helium, or hydrogen. This suggests the progenitor being a massive star stripped all the way down to its final layer before the iron core. The classification leaves space for the yet to be discovered explosion of a slightly less stripped star in a SN Type Idn which would have no carbon but strong oxygen, neon, and magnesium emission lines, as well as their non-interacting counterparts and transitional objects. (Schulze et al., 2024). [Get astronote ref in ones its on ADS](#)

1.5.3 Distant CSM

As stated in Section 1.5.1 and shown in Figure 1.6, there is a delay between the SN explosion and the start of CSM interaction due to the distance between the progenitor system and CSM. All objects that are currently classified as SNe Ia-CSM on the Transient Name Server¹ (TNS) have shown signs of interaction at or around peak brightness. Assuming an ejecta velocity of $v_{\text{ej}} \sim 20\,000 \text{ km s}^{-1}$ and that the interaction starts on average around the SN peak ~ 3 weeks after the explosion, the CSM is located at a distance $d \sim 3.5 \times 10^{15} \text{ cm}$ of the progenitor system (Sharma et al., 2023). If however the CSM is at a distance of $d \sim 10^{17} \text{ cm}$, ejecta with the same v_{ej} would need ~ 1.5 years to catch up and start interacting.

In the effort to systematically search for such late-time CSM interaction, Graham et al. (2019b) looked at old (≥ 1 year) SNe using the *Hubble Space Telescope* (HST). They focused their search on subclasses, such as 91T, that are associated with CSM interaction (Leloudas et al., 2015). Out of 72 targets, only ASASSN-15og and SN

¹<https://www.wis-tns.org/>

2015cp were found to show late-time CSM interaction. ASASSN-15og is a Type IIn SN with detected CSM interaction around peak, and was used as a control object. SN 2015cp has been classified as a 91T-like SN Ia, without signs of CSM interaction around peak. This showed that late-time CSM interaction may be systematically missed due to SNe Ia not being actively followed at these phases. From a progenitor point of view this means that material can be ejected from the system prior to the explosion, giving it time to travel further before being caught up by the SN ejecta.

[Dubay et al. \(2022\)](#) used archival UV-band data from the *Galactic Evolution Explorer* (GALEX) to look for late-time CSM interaction in SNe Ia. Out of a sample of 1080 SNe Ia, 4 were detected in the UV near peak, but none showed signs of late-time CSM interaction. They show that this type of CSM interaction is rare, occurring between 500 to 1 000 d after the initial discovery of the SN in < 5% of the SNe Ia at a strength similar to SN 2015cp, and a decreasing percentage as the interaction gets stronger. **Make sure all mentions of full spacecraft names are in italics**

1.6 In this thesis:...

In this thesis I will present my work on the search for signs of late-time interaction in Type Ia SNe using observations taken by ZTF survey. In Chapter 2 I will introduce the survey as well as the other facilities that have been used to gather data that is presented in this thesis. I will also give an overview of the basics of observing, some of the types of data that can be obtained, and the basic steps that are required to reduce them to something that can be used in further analysis.

Chapter 3 is an adaptation of [Terwel et al. \(2024\)](#), and presents my search for late-time signals in the ZTF SN Ia DR2, which consists of 3 628 spectroscopically classified SN Ia that were first discovered between March 2018 and October 2020. It also details the pipeline and analysis tools I developed to search in a consistent manner (Section 3.2).

It might be possible that a late-time signal is observed by ZTF while the main

transient occurred before the survey started. In Chapter 4 I search for this type of event using a slightly modified version of the pipeline used for the DR2 search. As the analysis is exactly the same whether the original transient was a SN Ia, SN II, or any other type of transient, I search through a sample of 8707 transients that were first discovered between 1 January 2008 and 1 January 2018.

Up to this point my search has been through archival data only, with the obvious drawback that it is very likely that any recovered late-time signal cannot be followed up on. By further modifying the pipeline I search in Chapter [not put in yet](#) for late-time signals in SNe Ia in real-time using the latest ZTF observations with the goal to follow up photometrically and/or spectroscopically using other telescopes.

Finally, in Chapter [not put in yet](#) I conclude on the results of searching through these three samples and finish with possible continuations of this search, modifications, and possible alternative usages for this or a similar pipeline.

To convert between apparent and absolute magnitude I assume a flat Λ CDM cosmology with $H_0 = 67.7 \text{ km s}^{-1} \text{ Mpc}^{-1}$ and $\Omega_m = 0.310$ ([Planck Collaboration et al., 2020](#)) throughout this thesis, unless specified otherwise. [Do I use another one anywhere?](#)

Observing in the optical regime

To do list: Add refs, sometimes slightly confused which tense to use, recheck carefully, opmaak, reference about the LP light pollution restriction laws? mention gain (e^- / ADU conversion) and read noise (mean e^- added per pixel at readout) as well somewhere.

Astrophysicists face the challenge of not being able to set up and control their experiments. The universe is our laboratory but all we can do is see or detect the results while often not knowing the exact setup of the experiment. Models are made to explain and predict the behaviour of planets, stars, galaxies, etc. but ultimately observations are needed to compare against and test our models. My work relies heavily on observational data, and in this chapter I will introduce the different types of observations that are used throughout this thesis (section 2.1), telescopes and instruments that are used to obtain these observations (section 2.2), and a quick overview of how to calibrate the raw images and extract useful data (sections 2.3 and 2.4). I will also give a general overview of what to consider when planning observations in section 2.5.

2.1 Types of obeservations

All optical observations are, in esssence, images taken by a camera. Light falls onto a pixel on the detector, a charge-coupled-device (CCD), and frees some amount of electrons. The more light that hits the pixel, the more electrons are freed. At readout these electrons are counted per pixel, or group of pixels if binning is applied, and turned into a digital number called a count. During this process there are contributions from different noise sources, but as long as the total count rate is in the linear regime of the CCD there is a linear relation between the received flux and final count. It is then possible to calculate the observed flux from the target by using calibration images. The different types of calibration images are described in section 2.3 and their usage is explained in section 2.4 when discussing image reduction.

2.1.1 Photometry

Photometry is one of the simplest observing modes as it is just taking a photo of a part of the sky. The top of Fig. 2.1 shows a raw photometric image, taken with ALFOSC on the Nordic Optical Telescope (NOT) without the use of a filter. The images are monochromatic, i.e. they only have a value for the intensity. For colourful images multiple observations have to be made using different filters and combined to represent different colours. Faint objects can be observed by increasing the exposure time in a single image, or by stacking multiple images together to increase the effective exposure time. Stacking images can be useful for e.g. reducing cosmic ray interference, avoiding overexposure of a bright source close to a fainter target, or for constructing time series. When stacking images it is common practice to dither the telescope: applying a small offset between exposures to ensure that the target hits a different part of the CCD to avoid issues with bad pixels ruining otherwise good observations. While this decreases the effective size of the fully stacked image, as long as the edges are not needed there is no issue.

2.1.2 Spectroscopy

Spectroscopy goes one step beyond just taking a photo. Assuming that this is slit spectroscopy, instead of a filter to select a wavelength range to observe now a slit restricts the observable region of the sky to a narrow band along one axis of the detector (e.g. horizontal). After the slit the light hits a grating or grism (a grating and prism combined) which diffracts the light based on wavelength across the second axis of the detector (vertical). The rule density on the grating / grism dictates the wavelength spread of the light: the more rules per unit distance, the bigger the diffraction, and the higher the spectral resolution of the resulting image. The tradeoff is that a smaller part of the spectrum can be observed at a time, and there is less light being received per pixel which reduces the SNR unless the exposure time is increased to account for this. Any point-like source that is observed becomes a line in the spectral direction,

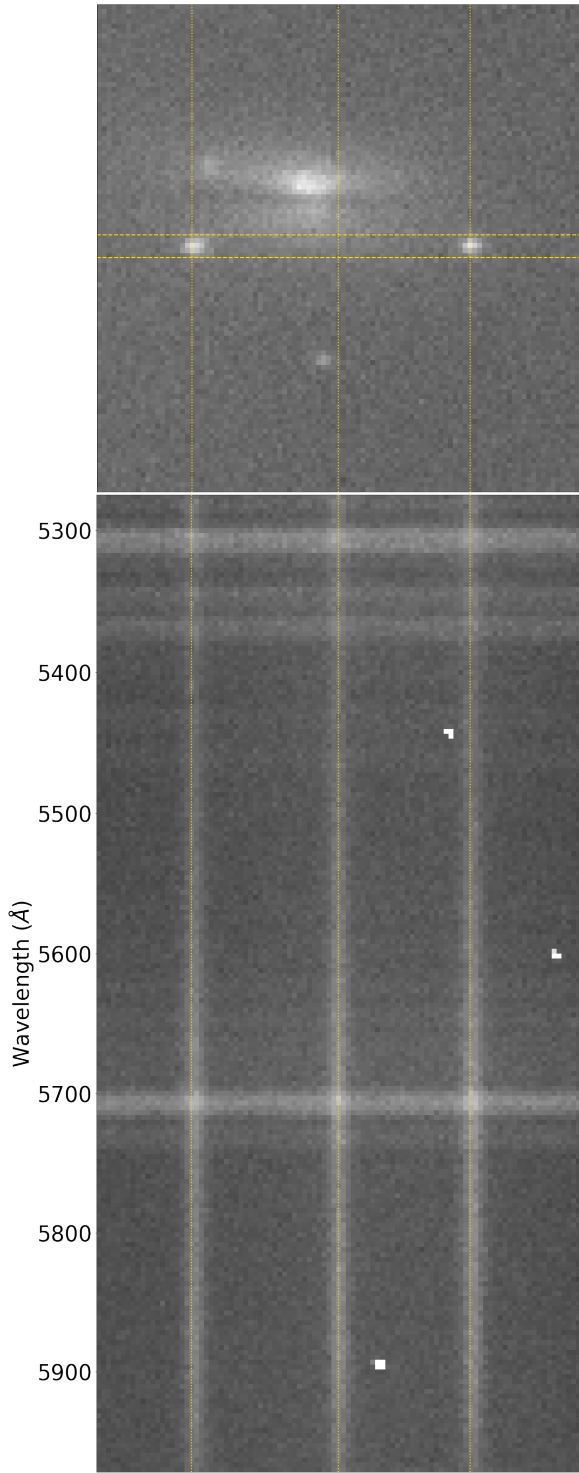


Figure 2.1: Image and partial spectrum of SN 2024nqr (left) and SN 2024pgd (right), two SNe Ia active simultaneously in the same galaxy. The image was taken without a filter and used to align the $1.0''$ slit (horizontal dashed lines) over both SNe. The resulting spectrum, taken with grism #4, shows three traces as white vertical stripes. The outer two line up with the two SNe, while the middle trace is from the host galaxy edge in the slit (vertical dotted lines for guidance). The horizontal lines in the spectrum are sky lines coming from atmospheric emission, and the white spots in the spectrum are due to cosmic rays. This data was taken with NOT+ALFOSC on the night of 28 July 2024 while testing an experimental rapid response mode (RRM, credit: Samuel Grund Sørensen). [check AT/SN status weirdness](#)

called a trace. Extended sources create extended traces.

There is some freedom in the orientation of the slit. This is called the position angle of the slit. If there are multiple targets near each other, and they can be in the slit at the same time, the required position angle can be calculated from the two target positions. If there is a single target to be observed the position angle can be anything, but usually the parallactic angle is chosen. In this orientation the slit is perpendicular to the horizon, and prevents losses from differential diffraction (different colours diffracting differently when entering the atmosphere at an angle, [Filippenko 1982](#)). The trace will only be slightly diagonal on the CCD.

The bottom panel of Fig. 2.1 shows a section of the spectrum taken of the SNe in the top panel image. The two SNe are drawn out into vertical traces and a third trace belonging to the edge of the host galaxy can be seen in the middle. The horizontal lines are sky emission lines, and while these can technically be used to estimate the conversion from pixel position to wavelength, standardized arc frames will result in a much better wavelength calibration (see section 2.4).

2.2 Telescopes

Most of the data used in this thesis comes from the Zwicky Transient Facility (ZTF), and follow-up observations have been made using the Nordic Optical Telescope (NOT), and the Gran Telescopio Canarias (GTC), which will be introduced below. Some additional data comes from other sources, which are listed for completeness. The same filter names (*gri*) are used for filters at different telescopes, which have slight differences. In the rest of this thesis I will use *gri* to refer to the ZTF filters, unless specified otherwise. [gotta make sure this is done correctly everywhere](#)

2.2.1 Zwicky Transient Facility

The Zwicky Transient Facility (ZTF, [Bellm et al. 2019a,b; Graham et al. 2019a; Masci et al. 2019; Dekany et al. 2020](#)) is an optical large-sky survey observing the entire

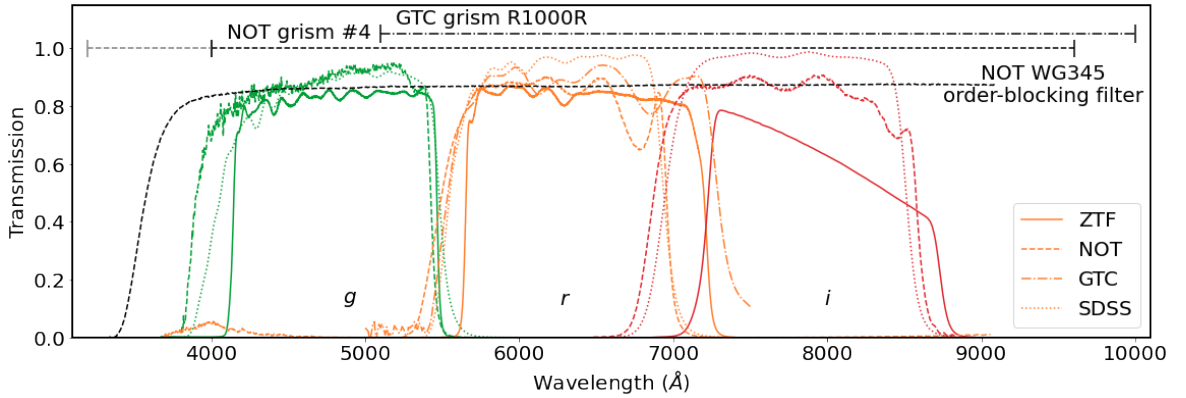


Figure 2.2: Throughput as a function of wavelength of the different filters used to gather the bulk of the data in this thesis *g* filters are shown in green, *r* in orange, *i* in red, and the different telescopes are shown with different line styles (Continuous for ZTF, dashed for NOT, dot-dashed for GTC). The SDSS filter transmissions (dotted lines) are shown for comparison. For the grisms the wavelength ranges are shown as only, not their efficiency at each wavelength.

northern night sky above Dec $\approx -30^\circ$ every 2 to 3 nights in three broadband optical filters *g* ($\lambda_{eff} = 4746.48 \text{ \AA}$), *r* ($\lambda_{eff} = 6366.38 \text{ \AA}$), and *i* ($\lambda_{eff} = 7829.03 \text{ \AA}$), which are similar to the well-known SDSS *gri* filters. The efficiency of these filters is plotted as a function of wavelength in Fig. 2.2. The survey saw first light in October 2017 and the survey formally began scientific operation in March 2018, and has been running continuously until the time of writing this document.

The observations are made using the 48" aperture Schmidt-type design Samuel Oschin Telescope, which is based at the Palomar Observatory in Southern California. Each exposure is 30 s long, can go a limiting magnitude of ~ 20.5 mag and covers an area of $\sim 47 \text{ deg}^2$ at a resolution of $1.01''$ per pixel. The camera is divided in a 4×4 grid of CCDs, each of which have 4 readout channels called quadrants. This results in each observation producing 64 separate images, each with their own readout channel identifier (rcid). Similarly, the observed region of the sky is divided into different telescope pointings called fields to ensure that the same region of the sky is observed in the same way each time, aiding with the reduction of the data. This results in each combination of filter, field, and rcid being a set of observations of a particular part of the sky using specific setup.

2.2.2 Nordic Optical Telescope

The Nordic Optical Telescope (NOT¹) is a 2.56 m telescope located at Observatorio Roque de Los Muchachos in La Palma, Spain, at an elevation of 2382 m above sea level. It hosts several instruments for observing in the optical and near infrared, both for imaging and spectroscopy. The Alhambra Faint Object Spectrograph and Camera (ALFOSC) was used to obtain the data used in this thesis. I will only discuss the parts relevant to this thesis, further details on this instrument and details on the other instruments can be found at the NOT website.

ALFOSC is a versatile instrument mounted in cassegrain and can be used for imaging, spectroscopy, and (spectro)polarimetry. As there are several wheels equipped to hold a variety of optical elements, the instrument can switch quickly between different setups between observations. The images can cover up to $6.4' \times 6.4'$ per exposure at a resolution of $0.2138''$ per pixel. In this thesis g ($\lambda_{cen} = 4800 \text{ \AA}$), r ($\lambda_{cen} = 6180 \text{ \AA}$), and i ($\lambda_{cen} = 7710 \text{ \AA}$) are used for photometry. For spectroscopy grism #4 is used to split the light vertically, together with a horizontal $1.0''$ slit if the seeing was $\leq 1.3''$ or a horizontal $1.3''$ slit if the seeing was $\geq 1.3''$. Grism #4 has a resolution of $3.3 \text{ \AA pixel}^{-1}$ and an wavelength range from 3200 \AA to 9600 \AA , but as the response at short wavelengths is poor, the spectra used in this thesis are cut at 4000 \AA . For some spectra an order-blocking filter (WG345) is used as well to avoid second order diffracted blue light to overlap with first order diffracted red light on the detector. The transmission curves of the filters and wavelength range of the grism are shown in Fig. 2.2.

2.2.3 Gran Telescopio CANARIAS

The Gran Telescopio CANARIAS (GTC²) is a 10.4 m telescope at Observatorio Roque de los Muchachos in La Palma, Spain, and is the largest optical / near infrared telescope on the island. Its primary mirror is made up from 36 hexagonal pieces creating an effective collection area of 73 m^2 , ideal for observing very faint targets. The GTC

¹<https://not.iac.es>

²<https://www.gtc.iac.es>

can host up to six instruments at a time in various focal positions, allowing for a large variety of observations to be made. One of the most commonly used instruments is OSIRIS+, the upgraded version of OSIRIS: the Optical System for Imaging and low-Intermediate-Resolution Integrated Spectroscopy.

OSIRIS+ has an unvignetted field-of-view of $7.8' \times 7.8'$ at a resolution of $0.254''$ per pixel. Since the standard readout has 2×2 binning, the resolution can be increased to $0.127''$ per pixel if so desired. Like ALFOSC, this instrument is also built to easily switch between different setups between observations. For photometry the r ($\lambda_{cen} = 6410 \text{ \AA}$) filter is used in this thesis, and for spectroscopy the R1000R grism with a $1.0''$ vertical slit is used. R1000R splits the light horizontally over the detector with a range of 5100 \AA to 10000 \AA with a resolution of $2.62 \text{ \AA pixel}^{-1}$. These filter transmission curve and grism wavelength range are shown in Fig. 2.2.

2.2.4 Other observations

Small amounts of data coming from other telescopes and surveys are presented in this thesis as well. This includes a follow-up observation of SN 2019ldf in Section 3.3.2.4 in g and r using the ESO Faint Object Spectrograph and Camera version 2 (EFOSC2, Buzzoni et al. 1984) imaging spectrograph on the ESO New Technology Telescope (NTT) in La Silla, Chile as part of the extended Public ESO Spectroscopic Survey of Transient Objects+ (EPESSTO+, Smartt et al. 2015).

To complement ZTF data of several SNe, in chapters **PUT REFERENCES ONES SECTIONS ARE IN, MIGHT BE DIFFICULT TO DO SECTION SPECIFIC FOR THIS** optical photometry from the Panoramic Survey Telescope and Rapid Response System (Pan-STARRS, Chambers et al. 2016), (intermediate) Palomar Transient Factory (PTF, Law et al. 2009; Rau et al. 2009, iPTF, Kulkarni 2013), All Sky Automated Survey for SuperNovae (ASASSN, Shappee et al. 2014; Jayasinghe et al. 2019), Asteroid Terrestrial-impact Last Alert System (ATLAS, Tonry et al. 2018), and Global Astrometric Interferometer for Astrophysics (Gaia, Gaia Collaboration et al. 2016) are used, as well as near-infrared photometry from the Wide-Field Infrared Survey Explorer

(WISE, Wright et al. 2010).

2.3 Calibration images

Before the observations can be used for science, the images need to be calibrated. This is done using different types of calibration images, each of which measure and correct for different effects of the telescope and detector. Usually these are taken during the day or twilight so no valuable observing time is lost. It is standard practice to take multiple calibration images and use an odd number in the reduction to find median values and remove interference from e.g. cosmic rays, this is called a master image.

2.3.1 Bias

The first type of calibration image is the bias, which is made by reading out the CCD without exposing. The resulting image contains the amount of counts that will be in every exposure regardless of what has been observed or with what exposure time. In other words, measuring the bias can be thought of as measuring the offset to correct for in every other image.

2.3.2 Dark

Any detector that is not at a temperature of 0 K will have some amount of noise due to thermal effects. This can free electrons in pixels over time, creating a dark current and increasing the noise over time. The effect can be measured by exposing for the same amount of time as the science images taken, but without letting any light hit the CCD. This is called a dark frame.

As this is a thermal effect, it can be reduced to negligible amounts by cooling the instrument. This saves precious observing time, as otherwise dark frames would ideally have to be taken at the same temperature as the target was observed, which is easiest to do directly after the science exposure. By cooling the detector with e.g. liquid

nitrogen this noise source can be avoided instead of having to correct for, saving time and the amount of images that need to be taken in the process.

2.3.3 Flatfield

The amount of light that the telescope receives is converted into a digital number, but there is no guarantee that this conversion rate is the same for each pixel. This can be due to intrinsic differences between the pixels, or outside effects such as dust reducing the amount of light received on a part of the detector. To correct for this an evenly illuminated field has to be observed, resulting in an image called a flat or flatfield. By ensuring that each pixel receives the same amount of light, the different counts will reflect the varying responses per pixel.

Any evenly illuminated object can be used for this, such as the inside of the telescope dome to create dome flats. A more perfect evenly lit source however is the sky, and using this sky flats can be taken. While it is usually too bright during the day and the CCD will saturate even with the narrowest filter and shortest exposure time, there is a window during twilight where the sky is darker but not dark enough to observe stars yet, perfect for taking flats. As a general rule, narrowband filters need a brighter sky and in the evening these need to be done before the broadband filters. After that, assuming similar efficiencies between filters, blue filters need brighter skies than red filters, forcing a specific order in which the sky flats need to be taken during the short window where this is possible. Of course if flats are taken in the morning the order has to be reversed.

2.3.4 Arc

In spectroscopy one of the axes has low wavelength at one end and high wavelength at the other end of the image. To know where each wavelength falls on the detector, arc frames are needed. These are taken by observing a lamp filled with a known set of elements (e.g. He, Ne, or TH and Ar). The wavelengths of the emission lines are

known very precisely, and by matching these with the observed lines in the arc image a pixel-to-wavelength conversion can be found, called the wavelength solution.

Usually arcs can be taken during the day, when the telescope is idle. However in some cases the mechanical flexure of the telescope, caused by being in a different position during observing, can introduce an uncertainty in the wavelength calibration unless an arc is taken with the telescope in the same position as for the target. In these cases an arc is usually taken directly before or after the target is observed, or between exposures of the target.

2.4 Reduction

After all observations have been taken it is time to analyze them. The first step is to reduce the raw data into the required format to work with. After that, additional analysis technique can manipulate the reduced images directly or the data that has been extracted from them. The response function of a detector can be written as

$$R_{ij}(f, t, \lambda) = B_{ij} + D_{ij}(t) + F_{ij}(\lambda) \times f \times t, \quad (2.1)$$

where R_{ij} is the CCD response of pixel i, j as a function of the integrated flux of the target $f \times t$ during the exposure which lasted a time t . The goal is to measure the flux f , which requires knowing and correcting for the bias level B_{ij} , dark current D_{ij} , and pixel response F_{ij} . Each type of calibration image is used to measure one of these values. Note that it is assumed that there are no cross or higher order terms in Eq. 2.1, in other words, the CCD is in its linear regime. When a pixel receives too much light and gets close to saturation it is no longer in its linear regime, and more terms appear in Eq. 2.1 making it much more difficult or even impossible to measure the observed flux.

2.4.1 Bias, dark, and flat corrections

Using the calibration images from section 2.3, the raw science images can be reduced to something a flux level can be measured from.

First the master-bias is created and subtracted from every other image. As both F and t are 0, the bias measures B_{ij} directly and can then immediately be removed.

With the bias gone, the dark frames measure D_{ij} for a specific t , but the master-dark can only be used on science observations with the same exposure time. Alternatively it is possible to subtract $B_{ij} + D_{ij}(t)$ in a single step by not separating out the bias term using bias images first.

Finally every science image is divided through the normalized master-flat to equalize the pixel responses. There is still a factor $F(\lambda)$ present as the detector efficiency is wavelength dependent, but the value is now independent of the pixel position, allowing values from across the CCD to be compared.

2.4.2 Cosmic-ray removal and image stacking

At this point it is often good practice to run a cosmic-ray removal algorithm to remove this source of noise as much as possible. This can be done using e.g. L.A.Cosmic ([van Dokkum, 2001](#)), which I used through Astro-SCRAPPY ([McCully et al., 2018](#)) when reducing follow-up photometry of several objects in this thesis.

If multiple images are taken of the same field or object they can be stacked to reduce background noise and increase the SNR of the observed objects. Sometimes the observations have been taken with dithering to avoid the same objects being on the same pixels in every exposure, which has to be taken care of to make sure that the images are stacked correctly.

2.4.3 Standard star calibration

Filters are never 100% transparent at any wavelength, and the CCD responds differently to different wavelengths as well. To correct for this, one last type of calibration

image is used: the standard star. This was not mentioned in section 2.1 as observing a standard star is exactly the same as observing the actual science target. The only difference is that the expected result of the observation is known and can be used to correct for the wavelength dependent efficiency of the instrument.

With photometry the observed brightness can be measured for each star in the image to get a list of instrument magnitudes. The relative differences between the magnitudes of objects are correct, but there is still an absolute offset across all objects. This is corrected by finding the offset using the standard star. If the filter is commonly used, there is a good chance many stars in the field have known magnitudes in that filter, which can be used for calibration instead of a dedicated standard star.

In spectroscopy the arcs are used to find the wavelength solution for the spectra, after which the trace from the standard star can be extracted and divided by the known spectrum of the star to obtain the sensitivity function of the detector $F(\lambda)$. The trace of the target can be extracted as well to get its spectrum, which can then be flux-calibrated using the sensitivity function. In some cases only a relative sensitivity function is known, resulting in a calibrated spectrum in an unknown flux unit. In these cases proper calibrated photometry of the object can be used to flux-calibrate the spectrum by integrating the spectrum over the filter transmission curve.

2.4.4 Forced photometry

The two most common methods to measure flux from a source in an photometric image are PSF photometry and aperture photometry. A good explanation of these can be found in [Da Costa \(1992\)](#). PSF stands for point spread function, and with this method a function is fitted to model the source. This function describes how an infinitely small point of light is spread over the detector, and through its spatial size and peak value the flux of the light source can be measured. Aperture photometry sums up the signal in a given radius around the source center and subtracts the contribution from the background in the same region.

Large surveys such as ZTF observe the night sky to find new transients and monitor

known ones. Difference imaging is used to subtract constant sources and reveal active transients, as these are the main sources that should be left in the difference image along with solar system objects that move across the sky. A historically popular algorithm for difference imaging is High Order Transform of PSF ANd Template Subtraction (HOTPANTS, Becker 2015)¹, which is used for image subtraction in Sect. 3.3.2.4. There are other algorithms as well. For instance, ZTF uses ZOGY (Zackay et al., 2016)², and in Sect. AUTOPHOT (?)³ is used to subtract reference images from follow-up observations obtained with the NOT and GTC.

Through PSF photometry the location and strength of each source in the image is determined, which are then compared to the locations of known sources to separate new from known ones. Each location has however been observed for the entire duration of the survey, which means that it is also possible to measure the flux of a known transient before and after it was visible in the images, creating a light curve for the full duration of the survey.

This is called forced photometry, because the PSF function is forced to center on a specific location instead of finding the best-fitting position for the centroid. All ZTF light curves that are used in this thesis have been obtained through FPBOT (Reusch, 2023)⁴. When there is nothing but noise at that location the measured flux will be 0 within the error. When there is a source at the target location it will be measured, but if the source is not at the center of the PSF the fit will have trouble converging, resulting in a large uncertainty. Artefacts such as cosmic rays, imperfectly subtracted difference images, or light bleeding effects from saturated bright nearby stars can also affect the accuracy of the photometry measurement.

¹<https://github.com/acbecker/hotpants>

²<https://github.com/cenko/ZOGY>

³<https://github.com/Astro-Sean/autophot>

⁴<https://github.com/simeonreusch/fpbots>

2.5 General considerations for observing

During my PhD I have spent two years doing studentships with the Isaac Newton Group of Telescopes (ING) and Nordic Optical Telescope (NOT) on La Palma, gaining first-hand experience with the specifics of observing in the optical regime and the considerations that come with it. I will briefly go over these in this section. These studentships also gave me the unique opportunity to very quickly follow up on interesting transients, which was very valuable for the objects that will be discussed in [chapter](#).

2.5.1 Location

Although this is normally already done before constructing a telescope, the first thing to consider is the observing location. When purely aiming for the best observations possible, there are three main things to consider when choosing where to observe from:

- Weather: Clear, stable sky conditions for most nights of the year, and low atmospheric distortion (e.g. seeing) are vital to ensure good quality data on a regular basis. Low hanging clouds can be avoided by being high above sea level, while simultaneously decreasing the amount of air light has to travel through to reach the detector, decreasing atmospheric influence.
- Light pollution: Darker skies allow observations of fainter objects. Even the presence of a (partially) illuminated moon significantly changes the depth that can be reached with the same exposure time. Many observatories have (inter)national laws to control the light pollution and ensure good quality data can be obtained.
- Target observability: The target location needs to be reachable by the telescope to be observable. The closer to zenith an observation is made, the less atmosphere between the target and telescope. The atmosphere reduces the data quality through turbulence (seeing), broadband absorption (clouds, dust), narrowband interference (tellurics, skylines), and differential diffraction, among others.

Observatories should be located on top of high mountains in areas with stable and clear weather, with as small a nearby population as possible while still being accessible enough for transporting materials and observing staff. One of the best locations in the world that meets these requirements is Roque de los Muchachos on La Palma, a small Spanish island in the Atlantic ocean off the coast of Morocco. At around 2300 m above sea level, the telescopes are built on the highest peak of the mountain far from most communities on the island which are much closer to sea level, and the temperate climate ensures good sky conditions for most nights around the year. Additionally, the government has put laws in place to minimize light pollution, e.g. by limiting the use of street lights and restricting flight paths over the island. I remember a plaque at the roque mentioning this, maybe it has a good ref?

2.5.2 Telescope, instrument, observation type, and setup

Depending on the type of observations and the brightness of the target there is a choice of hardware to be used. Telescope, intsrument, observation type, and desired setup(s) have to be considered together, as some choices will affect other ones.

Bigger telescopes can observe fainter targets, but it is also more difficult to obtain observing time. On the other hand, smaller telescopes are less oversubscribed (a measure of requested versus available observing time), but are more limited in observation depth even with long exposure times.

Secondly, different instruments, which are often telescope specific, have different observing capabilities. Photometry and spectroscopy are very standard observing modes, and most telescopes have at least one instrument can offer this. Even though ALFOSC and OSIRIS+ can both of these modes, there are still differences in data quality and resolution even if the same object is observed at the same time. However for polarimetric observations for instance, OSIRIS+ cannot be used while ALFOSC can, limiting the options for this observation mode.

Lastly, the specific setup has to be considered as well. For photometry, which filters are desired? If a very specific or rare filter is needed this may limit the options

of telescopes and instruments. For spectroscopy there are other choices, such as fiber or slit spectroscopy, different gratings or grisms depending on the desired resolution and wavelength range, neutral density filters to observe targets that are otherwise too bright for the instrument, and order-blocking filters to remove second order blue light from red parts of the spectrum.

2.5.3 Night plan

Lastly, it is good to have a plan of what to observe at each point during the night in order to avoid losing observing time during the night. Most proposals already have a list of targets and standard stars to observe and exposure times when they are submitted to request observation time, but the detailed plan is usually made mere hours before the night starts as it depends on e.g. the current weather, target priority, and specific time constraints (e.g. for transits). Calibration images might need to be taken during the night as well. All of these things need to be considered when trying to maximize the time used to expose and observe targets, and minimize the overheads from e.g. positioning, target acquisition, and readout.

Time spent repositioning the telescope can be reduced by finding the path between targets that minimizes telescope and dome movement throughout the night. The target acquisition time depends on the type of observation, but also on the experience and tiredness of the observer. With photometry a field is observed, so usually a small offset is not disastrous for the science. With spectroscopy the target needs to be identified and placed in the slit or fiber before the exposure can start, costing extra time. Readout times are detector specific, but can be sped up by windowing and binning if only a part of the CCD is needed, and a worse resolution is acceptable. Considering readout times can be especially important when multiple shorter exposures are taken instead of a single long one.

Nothing is certain during the night. Weather conditions can change suddenly, technical problems can occur, a high priority target can be discovered during the night, or observations might go so smoothly that they are completed faster than expected.

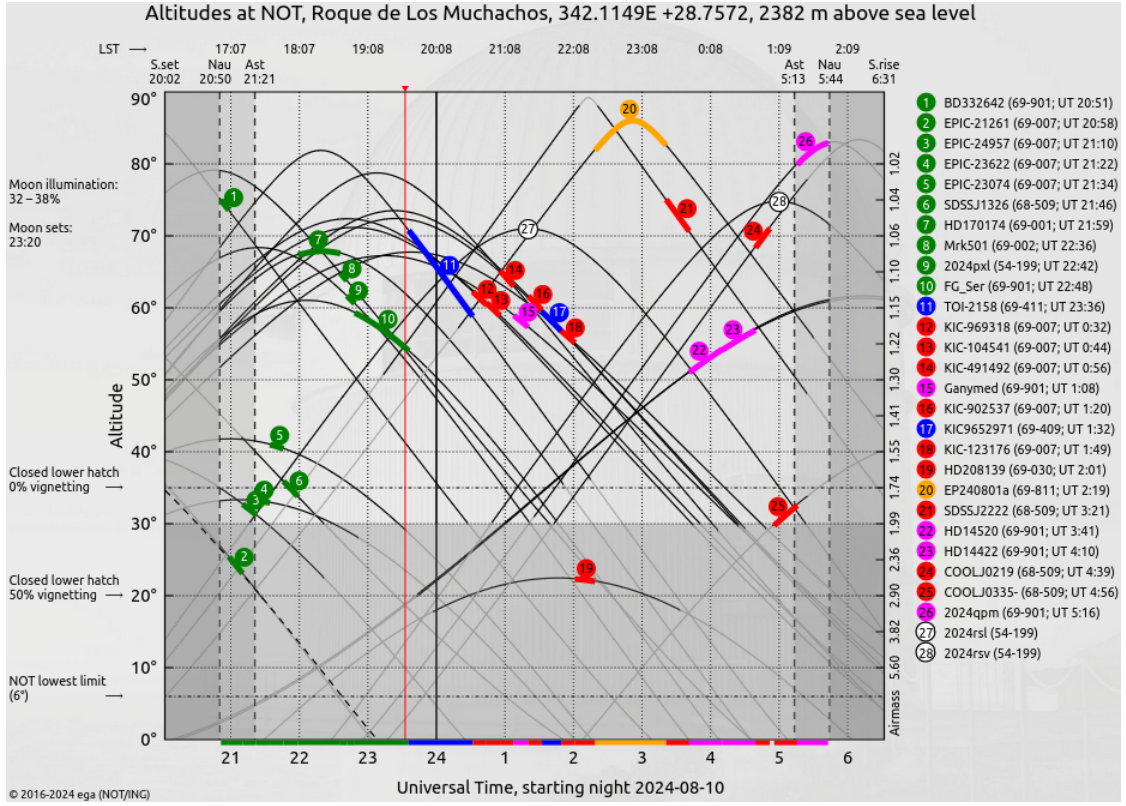


Figure 2.3: Night plan for the NOT on the night of 10 August 2024. Targets are plotted with their altitude as a function of universal standard time. Local stellar time is shown on top. The target priority has been colour coded, with the coloured bars showing the amount of time each observation is expected to take. Green targets have already been completed, and the red vertical line shows the current time. Several unscheduled backup targets are shown in case the plan has to be updated during the night.

A flexible schedule with a priority list and backup targets helps adapting to these situations quickly. After all, an idling telescope in (half-)decent observing conditions is a waste of resources. Fig. 2.3 shows an example night plan for the NOT with some space for adaptability built in.

ZTF SN Ia DR2: Searching for late-time interaction signatures in Type Ia supernovae from the Zwicky Transient Facility

This is Paper I, but needs to be properly adapted. Refer back to previous chapters. Copied in paper and appended the appendix straight afterwards. To-do list: Check for broken references, check for double refs, reformat pages, expand SNAP section, make sure all the *gri* things are consistent, check the in prep. refs

This chapter details my search for late-time interaction signals in the ZTF second data release (ZTF SN Ia DR2, Rigault et al. in prep.; Smith et al. in prep.) and has been published in [Terwel et al. \(2024\)](#). As stated in Section 2.2.1 the magnitude limit for single ZTF exposures is ~ 20.5 mag. By binning post-SN observations together for each confirmed SN Ia observed with ZTF, I attempt to push beyond this limit to find any faint signals that have gone previously unnoticed due to being close to the detection limit. In Section 3.1, I introduce the sample I use in my search for optical signals for late-time CSM interaction in the ZTF data stream. In Section 3.2, I present my custom pipeline for identification of late-time flux excesses and set up a simulation to test it and estimate the detection efficiency of my pipeline. Section 3.3 shows the result of running my sample through my pipeline, and provides further investigation on some interesting objects. These results are discussed in Section 3.4, and I conclude in Section 3.5. Chapter 3 contains the same details as the paper but expands on Section 3.2.3 with an extra figure.

3.1 Data

My aim is to look for late-time (>100 d after peak brightness) signatures of CSM interaction in the largest sample of SNe Ia to date. This has been obtained by the

ZTF. I am particularly interested in events that appear to be normal SNe Ia from their spectra and light curves around the peak but may display signs of late-time interaction, as seen in SN 2015cp ([Graham et al., 2019b](#)). My starting sample is 3628 events that were discovered by ZTF from March 2018 to October 2020 (hereafter the ZTF data release 2, ZTF DR2). Each event is spectroscopically classified as a SN Ia or one of its sub-classes. An overview of the ZTF DR2 will be presented in Rigault et al. (in prep.), including the sample definition, properties, and use for cosmology. In this study, since I am searching for likely rare signatures of interaction in the ZTF light curves, I am as inclusive as possible in my sample definition and include all SNe Ia in the DR2 covering a redshift out to $z = 0.288$.

3.1.1 ZTF light curve data

ZTF observes in three optical bands *gri* on a 2 – 3 day cadence. Reference images, mainly made using observations at the start of ZTF, are subtracted from the science images using the ZOGY image subtraction algorithm ([Zackay et al., 2016](#)) to produce difference images. Forced photometry is used at the transient location on the difference images using ZTFFPS ([Reusch, 2020](#)) to get a measure of the observed flux at each epoch. This includes non-detections before each SN was first detected and after each SN has faded below detection limits.

Light curve quality cuts on specific light curve points are applied as in Smith et al (in prep.). I do not correct the light curves for Milky Way extinction in my initial analysis but do consider it when focussing on specific objects of interest in Section 3.3.

Another approach for extracting photometry at the transient location is by using Scene Modelling Photometry (SMP; [Holtzman et al., 2008](#)). SMP is extracted for a few selected objects of interest in Section 3.3 to test if the identified late-time detections are independent of the approach. When using SMP, one has to define an ‘off’ time and an ‘on’ time. The observations taken during the off time are used to create a model of the region, or scene, where the SN occurs. This is then used as a template during the on time to calculate and remove host contributions to the photometry, leaving

just the transient itself (Lacroix et al. in prep.). The advantage of this method is the significantly lower uncertainty in the model compared to the difference imaging technique, allowing one to find fainter detections. Since I assume that a signal from late-time interaction could occur at any point after the SN, The off time is defined as everything up to shortly before the SN explodes, and the on time as everything after this moment.

3.1.2 Baseline correction

Issues in the construction of the reference images such inaccurate flat-fielding or artefacts in the images that are subsequently co-added can result in a systematic offset in the forced photometry light curve made using different images. The technique of baseline correction is used to correct for this (Yao et al., 2019; Miller et al., 2020).

To estimate the necessary baseline correction, I calculated the weighted mean of the flux of all data points up to 40 days before the estimated SN peak (which is assumed to be the highest flux detection deemed real), and subtracted it from the light curve. Baseline corrections are done separately for each combination of band (*gri*), field (telescope pointing), and rcid (part of the camera, which is arranged in 4×4 charge-coupled devices (CCDs) with four readout channels each, giving a total of 64 readout channels) as each of these combinations uses different, unique reference images. To be able to apply a baseline correction, at least two observations are needed. If this is not possible all observations with that band, field, rcid combination are removed.

Since I am interested in post-SN detections, my baseline correction method using only pre-SN data differs from the one used in Rigault et al. (in prep.) with both pre- and post-SN data. A comparison between the methods found that for most objects my corrections agree with the ones used in Rigault et al. (in prep.) within the uncertainties. This is as expected as objects with late-time flux excesses are expected to be rare, meaning that the two baseline correction methods should give the same result for most objects.

If there is insufficient data to perform a baseline correction, the relevant data (based

Table 3.1: Initial sample size and its reduction in each step of the analysis process.

Criterion	Removed	Objects left
Initial DR2 sample	-	3 628
No photometry at 100+ days	109	3 519
No robust late-time detections ^(a)	2 953	566
Presence of SN Ia tail ^(b)	432	134
Removed on visual inspection ^(c)	101	33
No late-time CSM interaction ^(d)	30	3

^(a)For a ‘robust detection’, at least four positive detections (two or more adjacent bins with $\geq 5\sigma$) are required out of the 16 possible combinations of bin size (25, 50, 75, 100 d), and the starting position of the bin varied by 25, 50 or 75 per cent of the bin size.

^(b)I tested for the presence of a radioactive tail of the SN Ia as described in Section 3.2.2 and removed those where this was the most plausible explanation.

^(c)Each remaining light curve was inspected using SNAP (Section 3.2.3) for possible issues causing late-time detections. See Section 3.3 for a discussion of the reasons events were removed.

^(d)For each remaining light curve I checked in detail if the late-time detections could be explained without CSM interaction starting at late times.

on field, filter and rcid) is removed from the light curve. If this includes data around the peak position, the peak position in the light curve may change and therefore, the position of the peak is recalculated.

3.2 Analysis

To systematically search for objects with late-time flux excesses, a custom pipeline was developed. In Section 3.2.1, I describe how the late-time photometry for each object is binned to reach deeper magnitude limits, as well as the scheme used to select objects with robust, significant detections. In Section 3.2.2, I identify and remove bright nearby SNe Ia whose late-time detections are due to the SN radioactive decay tail. In Section 3.2.3, I describe my method of visually inspecting images of potentially interesting sources, and in Section 3.2.4, I detail the use of SIMSURVEY to simulate SNe Ia with late-time interaction signatures. Table 3.1 shows my sample size after each step of analysis that is discussed in the subsequent sections.

3.2.1 Binning & filtering programme

After pre-processing, the late-time observations are binned in phase to push the detection limit beyond the limit of the individual observations. I define late-time observations as being at least 100 days after the estimated date of SN peak brightness in the observer frame. I remove all SNe Ia that have no data in any band beyond this phase. The exact choice of 100 days is arbitrary but was chosen as a balance between minimising spurious detections due to the light curves being dominated by SN light at earlier times and maximising the phase range over which the interaction can be searched for.

Binning of the light curves is performed in each band separately. Larger bins are better for pushing the magnitude limit as deep as possible, but they sacrifice temporal sensitivity. To balance the time sensitivity and magnitude limit, I use bins with widths of 100, 75, 50, and 25 days. To make sure that the placement of the bin edges does not affect my results, I repeat the binning four times for each bin size while adjusting the starting epoch of the bins by decreasing the size of the first bin by 25 per cent in each iteration. This results in a total of 16 trials for each band.

Each bin starts at the position of a data point to avoid empty bins. A gap in the data that is larger than the bins being used can cause the bins after the gap to always be placed in the same location despite the size modifications of the first bin. To avoid this I re-apply this modification of adjusting the size of the first bin after the data gap to trial different start positions. Lastly, if a bin would only contain one or two points, and the phases of these points occur no later than 10 per cent of bin size of the previous bin (e.g. if the bin size is 25 d, they would occur within 2.5 d of the end of the bin), the previous bin is increased in size to include these points. An example of the bin placement is shown in Fig. 3.1.

For each bin the weighted mean and uncertainty of the observed flux are calculated. When binning flux measurements taken from difference images, the uncertainty of the reference images used in the difference imaging procedure has to be considered, as this

will limit the depth of the binned observations ([Strotjohann et al., 2021](#)) and this is added in quadrature to the weighted uncertainty of the binned flux.

After the binning procedure each light curve has undergone 16 trials per band across four bin sizes and four bin placements. An attempt in a specific trial is considered significant if it has two or more adjacent bins with $\geq 5\sigma$ detections. A late-time detection is considered ‘robust’ if at least four out of 16 attempts have significant detections suggesting that the detections are insensitive to bin placement and/or size. I make this choice of robust detection in at least four attempts to ensure that I am not dominated by spurious detections but that I can still detect a long but faint signal that can only be picked up in the four trials involving the largest (100 day) bins.

3.2.2 Removal of SN Ia radioactive tail detections

For some nearby SNe Ia, the normal light curve tail powered by the radioactive decay of $^{56}\text{Co} \rightarrow ^{56}\text{Fe}$ is still visible at the phases investigated here (>100 d after the peak), possibly triggering false positives in my pipeline. To test if the fading tail is the reason for detections after 100 d, I checked if the detections follow a declining power law in flux space consistent with that of a normal SN Ia tail. I take all bins, normalise to the brightest data point, and fit a declining power law. To ensure that the tail matches the earlier data points, I include the unbinned observations between 60 and 100 d after the peak, making sure that if there are N bins only the latest N/2 unbinned detections are used to ensure that the fit focusses on the bins and not the unbinned points.

A successful fit of a declining normal SN Ia tail has a reduced chi-square of $\chi_{\text{red}, \text{fit}}^2 < 5$ and fitted half-life of $t_{1/2}$ with uncertainty $\sigma_{t_{1/2}}$, satisfying $t_{1/2} - 5\sigma_{t_{1/2}} \leq 50$ d. I chose a threshold of 50 d as [Dimitriadis et al. 2017](#) showed that this is the approximate decay time scale for a normal SN Ia at these phases. A fit with a high $\chi_{\text{red}, \text{fit}}^2$ value could have failed due to bad or uncertain data, or due to the late-time detections not following a power law decay. Fits with a $t_{1/2}$ significantly larger than that of a normal SN Ia tail suggest an additional luminosity source contributing to the light curve at these phases. Figure 3.1 shows an example where this tail fitting procedure determines

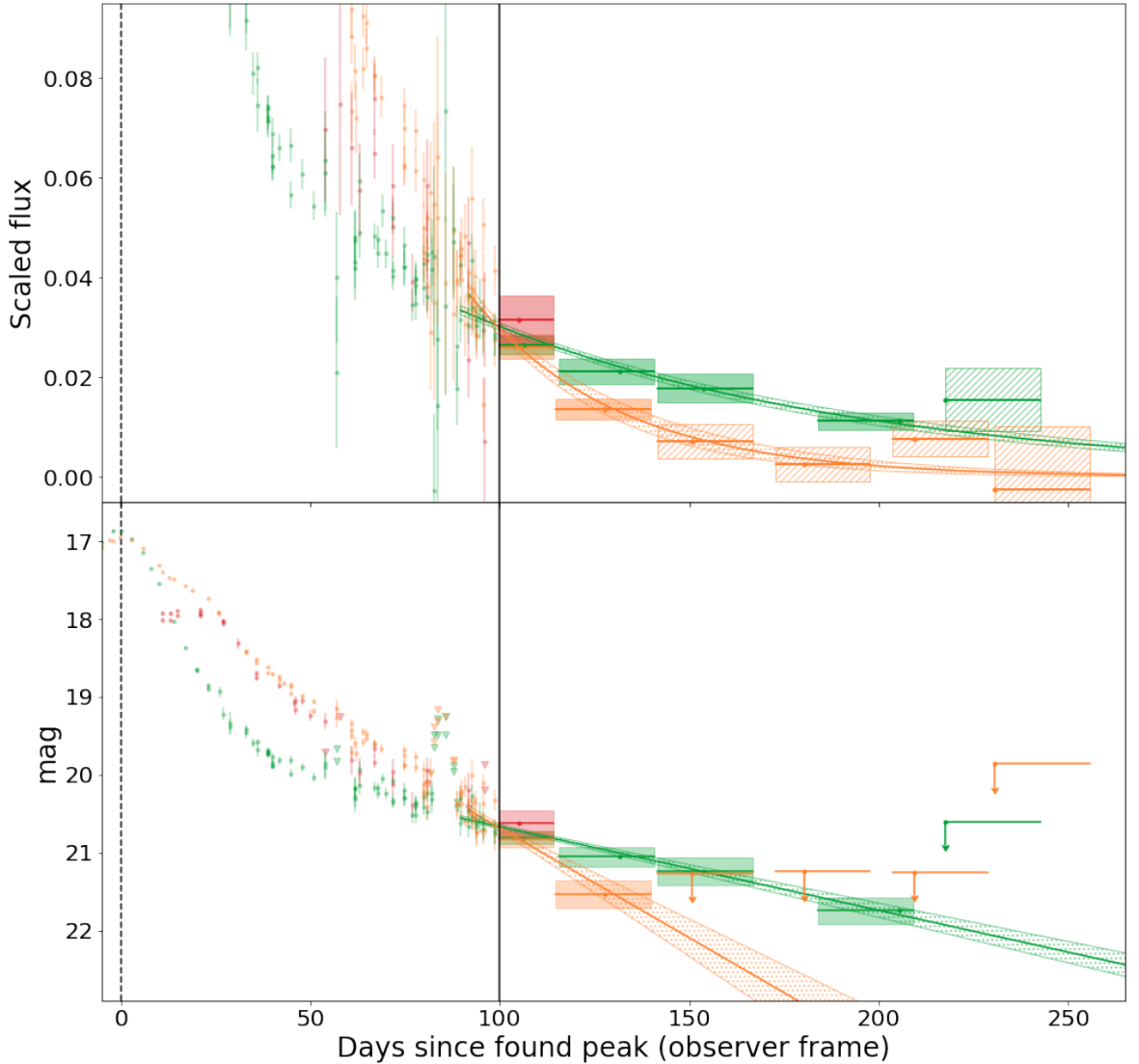


Figure 3.1: First 250 days of the *gri*-band light curves of SN 2019hbb in flux scaled to the peak flux (top panel) and magnitude (bottom panel) space. Binning starts 100 days after the estimated peak date (vertical black dashed and solid lines), using 25 d bins. The *g*-, *r*-, and *i*-bands are shown green, orange, and red, respectively. Before 100 days, I show the unbinned detections with their uncertainties (coloured circles) and non-detections (inverted triangles). After 100 days I show the bins as horizontal lines to show their size, a circle to show their mean value, and the shaded region showing the 1σ uncertainty (dashed regions are non-detections). A bin is deemed a non-detection if the flux $f < 5\sigma_f$. The 5σ magnitude limit is calculated and shown as a downward arrow. In both the *g*- and *r*-bands, the first bin is a detection and there are multiple adjacent bins with detections, triggering the tail-fitting procedure (see Section 3.2.2). The resulting tail fits are shown in the green and red lines, respectively, with their 1σ uncertainties as hashed regions. The half-life times are $t_{1/2,g} = 70 \pm 6$ d ($\chi^2_{\text{red}} = 0.6$) and $t_{1/2,r} = 27 \pm 4$ d ($\chi^2_{\text{red}} = 1.4$). This tail is therefore deemed to be a normal SN Ia tail.

the late-time detections in an object to be a normal declining SN Ia tail. 432 SNe Ia that were flagged as having late-time detection are discounted from further discussion because their light curves can be explained by a normal fading SN Ia tail.

3.2.3 SuperNova Animation Programme (SNAP)

After performing the binning and filtering, and removing SNe Ia with contamination from the radioactive tail, I am left with 134 SNe Ia with robust late-time detections (see Table 3.1). Since the binning and filtering programme is designed to handle a large quantity of light curves and cannot be tailored specifically to suit the peculiarities of a single object, it is possible that there are objects remaining with issues in the data or data processing (e.g. cosmic rays, bad subtractions), resulting in false positive detections. Therefore, I manually check the difference imaging to search for potential issues. To do this efficiently, I use SNAP¹.

Using ZTFQUERY (Rigault, 2018), SNAP takes all difference images of the requested sky position during the requested time period(s) in the requested band(s) and shows them in chronological order in an animation. At the start of each animation the reference images in all bands are shown. The programme can show the image in greyscale, a three-dimensional wire-frame representation of the intensities measured per pixel, the averaged values along both axes of the image, the observation date and duration, the peak and mean pixel values of the shown region, the last spectrum taken before the currently shown image, and highlight the resulting forced photometry point in the light curve corresponding to the plotted images. Figure 3.2 shows a frame of such a SNAP movie.

Using SNAP, issues in the difference images can be identified, including SN ghosts (the SN is visible in the reference image, leaving a negative imprint in difference images after it has faded), cosmic rays, and bad pixels (NaN, or a large negative number). Variability of a separate source can also be seen, which, when close by, can contaminate the forced photometry at the SN location. An example of such a contaminant is an

¹https://github.com/JTerwel/SuperNova_Animation_Program

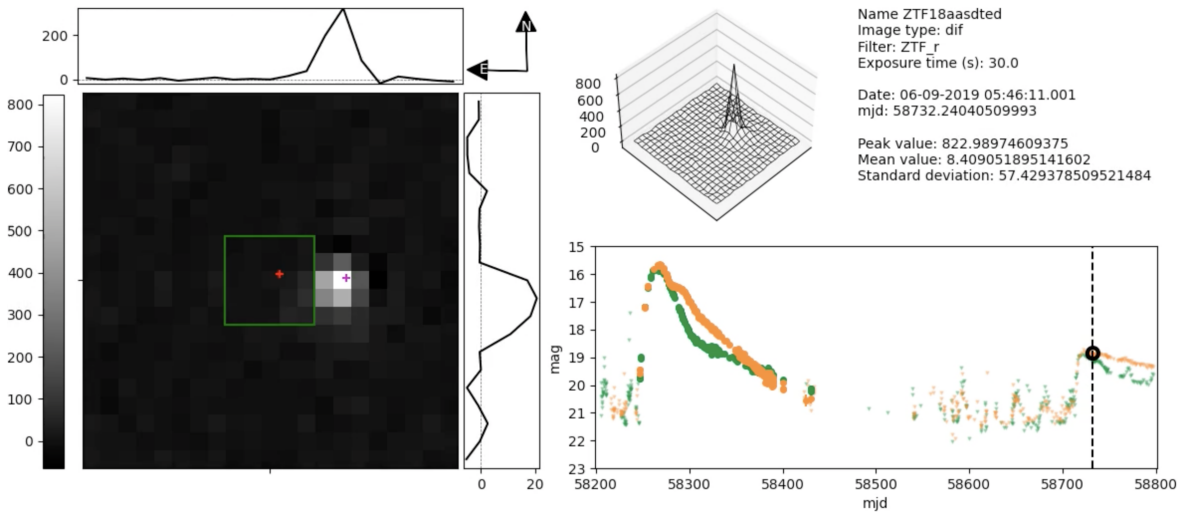


Figure 3.2: Frame of a movie made using SNAP showing the *r*-band difference images of ZTF18aasdted (SN 2018big). The left side shows a cutout of the difference image, with the red + at the location of ZTF18aasdted. The magenta + is at the location of ZTF19abqhobb (SN 2019nvm). The plots above and right of the image show the mean value of the middle five rows and columns respectively, with the green square indicating which rows and columns are used for this. The compass shows the orientation of the image, and the wireframe gives a different way of viewing the pixel values. General information of the image and object is shown in the top right corner, as well as some statistics of the shown cutout. The plot in the bottom right shows the light curve at the red +. The black dashed line shows the mjd of the currently shown image, and the black circle highlights the data point associated with it. The bottom right light curve can be replaced by a plot showing the latest spectrum at the time of the shown difference image.

active galactic nucleus (AGN).

3.2.4 Simulated interaction recovery fractions

To make sure the binning programme works as expected and estimate its detection efficiency in finding late-time signals, I simulated an observing campaign using SIMSURVEY (Feindt et al., 2019a,b), a python package designed to simulate large scale time domain surveys such as ZTF. To successfully simulate an observing campaign, the programme needs to be told what, when, where, and how something is observed, and under what conditions. For this, I need a model of the SN Ia-CSM that is going to be observed, an explosion rate as a function of redshift, and a time range for these explosions to occur. I also require an observing log specifying which part of the sky is being observed at a specific time, the length of the observations, and the weather conditions during the observations. Lastly, I require details of the camera that is used to carry out the observations. The SN model needs to be in a similar format to the

SNCOSMO models (a PYTHON package made for supernova cosmology, [Barbary et al. 2021](#)). This means I need a set of spectra over the entire phase range, all having the same wavelength spacing and range. Since no such model exists, I built my own model as described in the next section.

3.2.4.1 The interacting SN model

I chose SN 2011fe as the template of a normal SN Ia as it is well observed and close by (in M101 at a distance of 6.4 Mpc, [Shappee & Stanek 2011](#)). Optical spectra of SN 2011fe were obtained between phases of -18 to 1017 d relative to the peak. I made a custom model using SNCOSMO and spectra found on WISEREP ([Yaron & Gal-Yam, 2012](#))¹, which are listed in Table 3.7. The spectra were flux calibrated to match the observed coeval broadband magnitudes. Spectra up to 45 d after the peak were flux calibrated using a SALT2 ([Guy et al., 2007](#)) fit of the *PTF48g* and *PTF48R*-band photometry ([Law et al., 2009; Rau et al., 2009](#)), which is used to estimate the flux in the *g*- and *r*- bands at these phases. Spectra between 45 and 400 d are flux calibrated using a cubic spline interpolation of photometry in the *PTF48g*- and *PTF48R*-bands. The interpolation extends up to 600 d after the peak in the *PTF48R*-band, there is no *PTF48g* photometry used between 400 and 600 d after the peak. Three interpolated photometry points from the SALT2 fits were used as anchor points to connect these two parts of the calibration. [Dimitriadis et al. \(2017\)](#) show that there is a slight kink in the light curve tail around 600 d after the peak. This is replicated in the model by calibrating all spectra more than 600 d after the peak using a cubic spline interpolation of photometry from the Large Binocular Telescope (LBT; [Hill et al., 2006](#)) in the Bessel *R*-band ([Shappee et al., 2017](#)).

After flux calibration, the spectra were dereddened to remove dust extinction effects, using the [Cardelli et al. \(1989\)](#) extinction law with $A_V = 0.04$ mag ([Patat et al., 2013](#)). The spectra were rebinned, and any wavelength region that was not covered in all spectra was removed as required by SIMSURVEY. Lastly, the model is corrected for

¹<https://wiserep.weizmann.ac.il>

distance, redshift and time dilation. The resulting model is that of a normal SN Ia, which exploded at a distance of 10 pc without any dust between the source and observer.

The best late-time detection of CSM in a normal/91T-like SN Ia was for SN 2015cp, where H α emission was identified in its spectra at 664 d after the light-curve peak ([Graham et al., 2019b](#)). To model potential CSM interaction signals similar to that of SN 2015cp, I add a narrow H α line with a Gaussian profile to the SN 2011fe model. Due to the rareness of interaction in otherwise normal SNe Ia, I do not have good constraints on the diversity of interaction signatures and simulate a broad parameter space. The interaction was chosen to start at 100, 200, 300, or 500 days after the peak, last for 100, 300, or 500 days, and have a similar brightness to the observed signal in SN 2015cp ([Graham et al., 2019b](#)), as well as 10 times weaker or 10 times stronger than it. All possible combinations of these values are used, and a simulation without any interaction is also used as a control test, giving a total of 37 simulations.

Figure 3.3 shows an example of my model spectra at 300 d and SN 2015cp at 694 d in the rest frame ([Graham et al., 2019b](#)). It also shows the model redshifted to $z = 0.07$, where the H α line is partly shifted into the i -band. Figure 3.4 shows the absolute magnitude ri -band light curves of the SN 2011fe model in the rest frame, as well as light curves with different strengths of H α emission. My interaction model will only generate a late-time interaction signal in the r -band (or i -band at $z > 0.06$) as I only add a H α emission line. This is enough to test the binning programme but is likely too simple to reflect the actual late-time signal seen in SN 2015cp (which also showed O I and Ca II in the restframe i -band) or potential other events.

3.2.4.2 Simulating the observing campaign

By specifying the object to observe, as well as the telescope details and observation schedule, an observation campaign can be performed using SIMSURVEY resulting in a collection of observed light curves. For a deeper explanation of SIMSURVEY I refer the reader to [Feindt et al. \(2019b\)](#). The parameters used as input are listed in Appendix

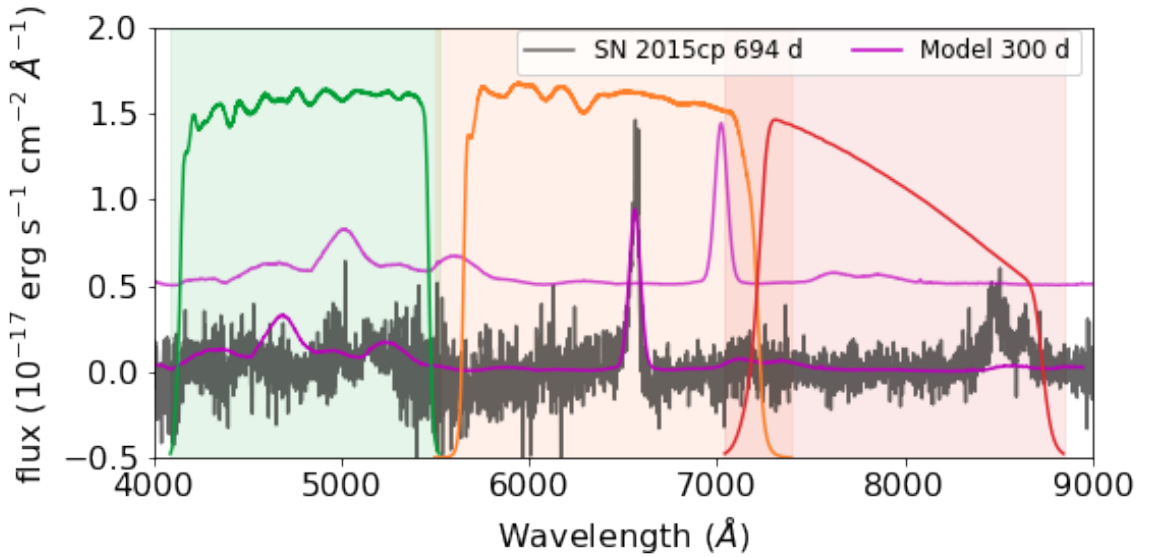


Figure 3.3: Model spectrum at 300 days (SN 2011fe with the added $\text{H}\alpha$ line) is shown in magenta overlaid on a rest-frame spectrum of SN 2015cp at 694 days in grey. The model flux has been scaled to the distance of SN 2015cp for comparison. The green, orange, and *i*-bands, respectively. The transmission profiles are plotted in the same colours for each band. The model is also shown shifted to $z = 0.07$ (and offset up in flux), where the $\text{H}\alpha$ line has just started to be in the *i*-band.

3.7. In each SIMSURVEY run, 10^5 SNe Ia are simulated to produce observed light curves and meta-data such as redshift, observed peak date, etc. To ensure that the SNe Ia are similar around the peak to those recovered, I require that the SN Ia light curves must have at least three detections of $\geq 5\sigma$ and are brighter than 19 magnitude at the peak. This reduces the sample to $\sim 40,000$ objects per simulation. These are sent through the binning and filtering programme (Section 3.2.1) as if they were real observed light curves to determine the recovery efficiency.

The volumetric rate used as input in the simulations favours more distant SNe, which results in very few SNe at extremely low redshift values and hence larger uncertainties. To mitigate this, I split $0 \leq z \leq 0.015$ into bins of size 0.001 and simulate an additional 100 SNe in each bin using the same parameters as in the original simulations. Introducing these additional events does not impact the recovery efficiencies because I am comparing the number of recovered events relative to the input number in each redshift bin and therefore, am insensitive to the input rate of events.

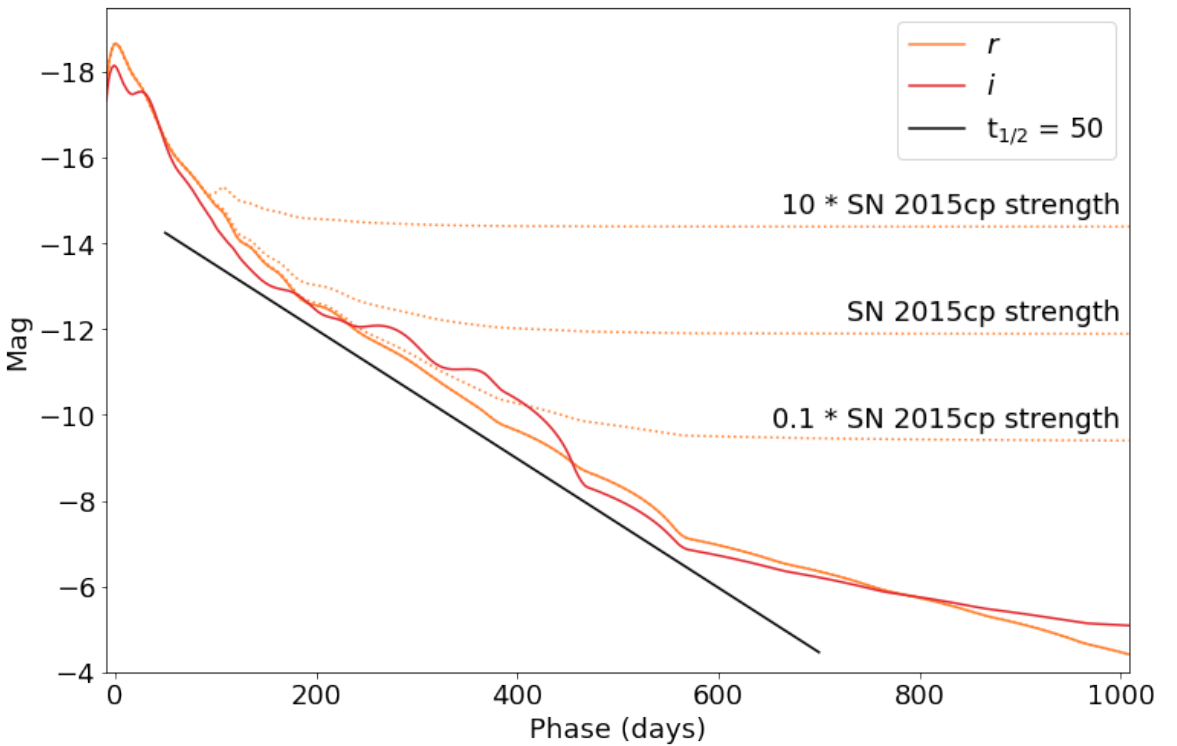


Figure 3.4: r (orange) and i (red) absolute magnitude light curves of the SN 2011fe model used in the simulations in the ZTF bands as a function of phase from rest-frame B -band peak (Mazzali et al., 2014). The bumpiness in the models is because the underlying SNCOSMO model class interpolates in flux space but fails to find an exponential decay. The added rest-frame CSM interaction model based on $H\alpha$ emission (starting at a phase of 100 d) is shown with dotted lines for the r -band. Once the interaction becomes the dominant source, it smooths out the bumps from the underlying tail. The black line shows a radioactive decay with $t_{1/2} = 50$ d, typical of a declining normal SN Ia tail.

3.2.4.3 Simulated interaction recovery

My aim is to determine from my simulations how many SNe Ia with signatures of late-time interaction similar to that of SN 2015cp would have been detected by my pipeline. For each of the simulations, I binned the SNe based on their redshift and looked at the fraction of SNe that were reported by the pipeline to show late-time excesses. Figure 3.5 shows the recovery fractions as a function of redshift for an example simulation when the interaction starts at 500 d and lasts for 500 d for simulations of no CSM interaction, late-time interaction with the same strength as SN 2015cp, and interaction 10 times as strong as SN 2015cp (strong interaction). As expected the recovery fraction drops off with increasing redshift for both the SN 2015cp equivalent strength and the interaction that is 10 times stronger, with the strong interaction recoverable out to a higher redshift.

The recovery fraction of the simulations with CSM interaction does not reach 100 per cent in the lowest redshift bins. This is because the radioactive tails of these SNe Ia tend to be bright out to hundreds of days after explosion. Therefore, depending on the cadence and uncertainties of the simulated photometry, the SN light can dominate over the CSM interaction and the CSM interaction signal does not alter the shape of the SN decay tail enough to be flagged as CSM interaction.

In the simulation without CSM interaction, the recovery fraction is non-zero at small redshifts, meaning that some objects are falsely identified as having late-time excess. For these very bright and high signal-to-noise SN Ia light curves, the decaying tail model for normal SNe Ia proves to be too simple. My analysis pipeline detects real deviations of the SN light curve evolution from the simple decay tail model. This only occurs at the lowest redshifts and nearby SNe Ia are rare, with only 0.6% of my observed SN Ia sample at $z \leq 0.01$. This means that contamination of my sample due to normal SNe Ia tails that cannot be fit by the simplified tail fit model is very low.

I fitted a sigmoid function to the recovery fractions of each simulation, using the total amount of objects in each bin as its weight (Fig. 3.5). A sigmoid function is an

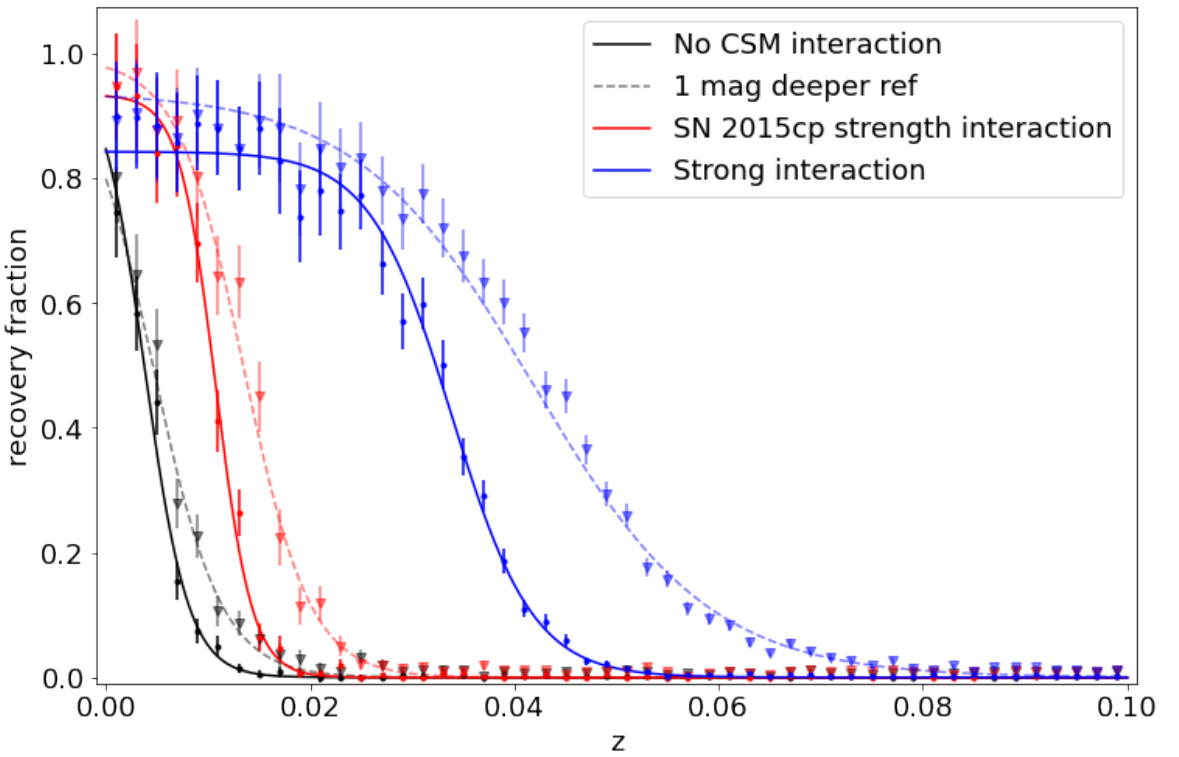


Figure 3.5: Fraction of SNe Ia for one of my simulations (interaction occurring between 500 – 1000 d after the peak) where the CSM interaction was recovered per redshift bin of size 0.002. The simulations are shown for interaction strengths of zero (grey), similar to SN 2015cp (red), and 10 times stronger than SN 2015cp (blue). In the simulation without CSM interaction, the recovery fraction should be interpreted as the fraction of false positives. The simulations with normal ZTF quality reference images are shown with dots and fitted sigmoid functions with solid lines. Simulations where one magnitude deeper reference images were assumed are shown in triangles, with their fitted sigmoid functions in dashed lines.

oversimplification (the recovery fraction is underestimated at the low redshifts) but it allows me to easily estimate the redshift limit where CSM interaction can be recovered. I define my redshift limit where CSM interaction can be recovered as z_{50} , the redshift where 50 per cent of the SN interactions are recovered. These values are listed for all simulations in Table 3.8.

As discussed in Section 3.2.4.1, I simulated 36 models with interaction signatures starting at 100, 200, 300 and 500 d post peak, lasting for 100, 300 and 500 d, and with strengths the same as SN 2015cp, 10 times weaker and 10 times stronger. I also simulated a model without any late-time CSM interaction. For the models with an interaction strength similar to SN 2015cp (Graham et al., 2019b), when the interaction is short and early (starting 100 days after the peak and lasting for 100 days), the interaction cannot be distinguished from a normal SN Ia decaying light curve and the

recovery fraction is as low as the no interaction simulation. When the interaction is longer, or if it starts later, the light curve flattens enough to be identified as deviating from a normally declining SN Ia tail. This pushes the redshift boundary where 50 per cent of the interaction would be recovered by ZTF to $z_{50} = 0.0105 \pm 0.0003$ for the longest and latest interaction (500 - 1000 days after peak).

If the CSM interaction is 10 times weaker than that of SN 2015cp, the decaying SN Ia tail generally dominates over the interaction signature and the light curve shows little deviation from a normal decaying SN Ia tail. Even in the best case scenario of the longest and latest CSM interaction simulation, the 50 per cent recovery thresholds lies at $z_{50} = 0.0050 \pm 0.0005$. In the simulations where the interaction is 10 times stronger compared than that of SN 2015cp, the shortest and earliest interaction (lasting from 100 to 200 days after peak) has $z_{50} = 0.0091 \pm 0.0014$. For the longest and latest interaction, the 50 per cent recovery rate is at $z_{50} = 0.0323 \pm 0.0004$.

3.2.4.4 Impact of reference image depth

The mean limiting magnitude of the ZTF reference images is ~ 21.8 mag and as discussed in ([Strötjohann et al., 2021](#)), this is the limiting factor for recovering faint signals from binned light curve data. To test the improvement of deeper reference images, the assumed limiting magnitude was changed to be 0.5 and 1 mag deeper. The recovery fraction for one magnitude deeper is shown for comparison in Fig. 3.5. As expected, deeper reference images allows the interaction signatures to be detected to higher redshift, although the increases in z_{50} values are modest (see Table 3.8). For example, for the latest onset and longest interaction duration interaction, z_{50} increases from 0.0323 ± 0.0004 to 0.0407 ± 0.0009 .

3.3 Results

I run my custom detection pipeline on the ZTF DR2 light curves in the same way as it was performed on the simulated light curves in Section 3.2.4. In 1932 light curves,

nothing is detected in any of the 16 trials discussed in Section 3.2.1, in 432 light curves the late-time detections are attributed to declining SN Ia tails, and in 1020 light curves the detections were not considered robust (<4 successful trials). These are the three largest cuts in my sample, as can be seen in Table 3.1, and leave me with 134 light curves that pass the pipeline. In Section 3.3.1, I describe the light curves of these events and discuss how some light curves fit into known classes of events (e.g. known Ia-CSM, late-time SN Ia tail detections). In Section 3.3.2, I describe the additional tests that were performed on the remaining promising 10 events to determine if their late-time excesses are due to CSM interaction or other scenarios.

3.3.1 Initial summary of detected events

As can be seen in Table 3.1, the result of the pipeline is a list of 134 objects that require visual inspection after passing the detection cuts of positive $>5\sigma$ detections in adjacent light curve bins in at least four of the 16 bin size and placement combinations. In 47 of these cases, by visual inspection I identify that an incorrect baseline caused false positives. In five cases, the peak date estimation failed and estimated the peak to be over 100 days before the actual SN explosion. Because of this the SN itself was detected as a late-time signal. Furthermore, in 29 cases there was evidence of the host galaxy being improperly subtracted or showing signs of activity, which interfered with the forced photometry at the SN location. Finally, in 20 cases the tail fit test was unable to show the nature of the tails due to various reasons (e.g. the fits did not converge properly or there was a gap in the observations while the tail was visible). After this step, 33 objects were remaining in the sample.

Further details of these remaining 33 SNe Ia are shown in Table 3.2 and can be split up into four main groups: i) known Ia-CSM events, ii) transient siblings, where a second transient event occurs near the identified SN Ia causing its light to (partially) be picked up during forced photometry at the first SN location, iii) nearby objects whose tail could not be fitted by my simple model, and iv) objects that do not fall in the first three groups. In the following sections, I describe the first three of these groups that

Table 3.2: List of objects that passed the initial visual inspections.

Name	IAU name	Redshift	Type ^(a)	Peak MJD	Peak mag.	Excess phase (d)	Excess band	Excess mag.	Group ^(b)
ZTF18aaykjei	SN 2018crl	0.09690 ± 0.00002	Ia-CSM	58297.3	18.40 ± 0.04	100 – 400	r	20.1 – 21.9	Known Ia-CSM
ZTF18abuafp	SN 2018gkx	0.13643 ± 0.00001	Ia-CSM	58382.1	18.71 ± 0.05	100 – 475	gri	19.6 – 21.5	Known Ia-CSM
ZTF18actuhrs	SN 2018evt	0.02442 ± 0.00001	Ia-CSM	58476.5	16.19 ± 0.01	100 – 525	gri	16.6 – 21.8	Known Ia-CSM
ZTF19aaeoqst	SN 2019agi	0.05958 ± 0.00001	Ia-CSM	58511.5	18.46 ± 0.04	100 – 450	gri	19.2 – 21.9	Known Ia-CSM
ZTF19abidbqp	SN 2019ibk	0.04014 ± 0.00001	Ia-CSM	58688.5	18.56 ± 0.05	100 – 1125	gr	19.1 – 21.5	Known Ia-CSM
ZTF19acbjddp	SN 2019rvb	0.1832 ± 0.0004	Ia-CSM	58790.1	18.90 ± 0.06	100 – 400	gr	20.4 – 22.0	Known Ia-CSM
ZTF20aaxtryt	SN 2020eyj	0.0294 ± 0.0004	Ia-CSM	58939.2	17.24 ± 0.01	100 – 450	gr	19.0 – 21.8	Known Ia-CSM
ZTF20abbbsfs	SN 2020kre	0.13530 ± 0.00001	Ia-CSM	58998.2	19.09 ± 0.04	175 – 425	gr	19.8 – 21.4	Known Ia-CSM
ZTF20abmlrxr	SN 2020onv	0.0940 ± 0.0004	Ia-CSM	59052.4	17.85 ± 0.01	100 – 500	gr	18.8 – 21.6	Known Ia-CSM
ZTF20abqkbf	SN 2020qxz	0.0968 ± 0.0004	Ia-CSM	59094.3	18.18 ± 0.04	100 – 450	gri	19.5 – 21.9	Known Ia-CSM
ZTF20accmutv	SN 2020uem	0.043 ± 0.001	Ia-CSM	59173.5	16.38 ± 0.01	100 – 525	gr	17.4 – 21.4	Known Ia-CSM
ZTF20aciwcuz	SN 2020xtg	0.06122 ± 0.00001	Ia-CSM	59189.5	17.45 ± 0.02	100 – 500	gri	18.0 – 21.9	Known Ia-CSM
ZTF20acyroke	SN 2020aeuh	0.12665 ± 0.00004	Ia-CSM	59217.4	19.01 ± 0.06	100 – 250	r	19.8 – 20.9	Known Ia-CSM
ZTF18aasdted	SN 2018big	0.01814 ± 0.00001	Ia-norm	58268.4	15.64 ± 0.01	450 – 550	gr	20.4 – 21.5	Sibling
ZTF19aaysiwt	SN 2019hnt	0.0926 ± 0.0004	Ia	58651.2	18.46 ± 0.05	525 – 625	gr	20.5 – 21.7	Sibling
ZTF19acihfxz	SN 2019tjz	0.055 ± 0.003	Ia-norm	58795.1	18.00 ± 0.03	950 – 1050	r	19.4 – 20.7	Sibling
ZTF20abzetedf	SN 2020ft	0.071 ± 0.002	Ia-norm	59113.5	18.2 ± 0.1	725 – 800	r	19.4 – 20.2	Sibling
ZTF20aachyxd	SN 2020uvd	0.0340 ± 0.0005	Ia-norm	59129.3	18.72 ± 0.03	300 – 350	r	20.2 – 21.5	Sibling
ZTF19aatlmo	SN 2019ein	0.0072 ± 0.0001	Ia-norm	58617.0	blinded ^(c)	100 – 425	r	18.9 – 21.8	Kinked tail
ZTF20abqvsk	SN 2020rcq	0.00246 ± 0.00001	Ia-norm	59144.5	blinded ^(c)	100 – 400	i	16.5 – 22.2	Kinked tail
ZTF20abrmjgi	SN 2020qxp	0.00356 ± 0.00001	Ia-91bg	59088.1	blinded ^(c)	100 – 375	r	17.9 – 21.8	Kinked tail
ZTF20abwrcmq	SN 2020sck	0.01643 ± 0.00001	Iax	59099.4	16.25 ± 0.01	100 – 450	gri	19.1 – 21.9	Kinked tail
ZTF20aachced	SN 2020uxz	0.00867 ± 0.00008	Ia-norm	59142.4	blinded ^(c)	100 – 400	gr	17.1 – 21.9	Kinked tail
ZTF19acwrqtv	SN 2019vzf	0.059 ± 0.004	Ia-99aa	58829.1	18.00 ± 0.07	150 – 400	gr	20.7 – 21.8	Other – AGN ^(d)
ZTF20aahtpds	SN 2020awr	0.07649 ± 0.00002	Ia-norm	58888.5	18.54 ± 0.07	300 – 1050	i	20.2 – 20.5	Other – data issue ^(d)
ZTF20aaazwuin	SN 2020kzd	0.082 ± 0.001	Ia-norm	58997.4	18.86 ± 0.03	250 – 850	gr	21.3 – 22.0	Other – data issue ^(d)
ZTF18abtqeves*	SN 2018grt	0.042 ± 0.003	Ia-norm	58372.3	18.56 ± 0.02	1350 – 1450	r	21.1 – 21.3	Other
ZTF19aanyuyh	SN 2020pkj	0.02456 ± 0.00001	Ia-norm	59060.4	16.90 ± 0.01	100 – 175	r	20.8 – 21.1	Other
ZTF19abfvhlx*	SN 2019ldf	0.05646 ± 0.00001	Ia-norm	58686.5	17.90 ± 0.04	1050 – 1225	ri	20.1 – 21.1	Other
ZTF19ablekwo	SN 2019mse	0.088 ± 0.004	Ia-norm	58715.4	18.37 ± 0.02	450 – 700	gri	19.8 – 20.6	Other
ZTF19abzwtiu	SN 2019rqn	0.075 ± 0.003	Ia-norm	58760.3	18.62 ± 0.03	950 – 1050	i	20.6 – 21.4	Other
ZTF20aaifyfx	SN 2020alm	0.06001 ± 0.00001	Ia-norm	58873.5	18.10 ± 0.02	750 – 1025	gri	19.9 – 21.9	Other
ZTF20abjfufv*	SN 2020tfc	0.031 ± 0.001	Ia-norm	59116.3	17.22 ± 0.01	550 – 800	gri	18.9 – 21.4	Other

*The three final objects with suggested detections of late-time interaction.

^(a)Type is based on spectral classifications (Rigault et al., in prep.), Ia-CSM are those interacting with CSM that is observed around peak, Ia-norm are those that are most consistent with a normal SN Ia, Ia are those without a sub-classification but are consistent with being a SN Ia, and SN 2020sck is a Iax (Dutta et al., 2022).

^(b)The objects are split into four groups: Ia-CSM that were previously known, identified siblings, SNe Ia that are detected due to their early-time tail fits showing a kink (Kinked tail), and the ‘Other’ category that includes ten events with potential flux excesses, including three (SN 2019vzf, SN 2020awr and SN 2020kzd) that are subsequently ruled out (see Section 3.3.2).

^(c)The peak magnitudes of four SNe Ia in the sample are blinded because of their planned use in H_0 constraints (Rigault et al., in prep.).

^(d)SN 2019vzf is ruled out as a true excess due to AGN variability at the position, in SN 2020awr the excess is only detected in the *i* and is ruled out by the scene modelling analysis, and SN 2020kzd is detected in the *gr* bands on a complex galaxy environment and not detected in the scene modelling analysis (see Section 3.3.2.1).

are not due to potential CSM interaction at late times.

3.3.1.1 Known Ia-CSM

The first group are the 13 known Ia-CSM, defined as those objects that already had a Ia-CSM classification. These objects started interacting relatively soon after the explosion and remained active long enough to be picked up by my pipeline beyond the 100 day threshold. Figure 3.6 shows the light curves of the recovered SNe Ia-CSM in absolute magnitude space (uncorrected for extinction). Even if the peak identified by my code is not the real peak due to it not being observed (e.g. for SN 2018evt, SN 2019agi, and SN 2019ibk), the CSM interaction persists for long enough for it to be picked up by my pipeline.

Ten of the known Ia-CSM SNe are presented in [Sharma et al. \(2023\)](#), who search for SNe Ia-CSM discovered in the ZTF Bright Transient Survey from May 2018 to May 2021 (BTS; [Fremling et al., 2020a](#); [Perley et al., 2020a](#)). They find two objects that are not in my sample: SN 2020abfe (ZTF20acqikeh) and SN 2020aejk (ZTF21aaabwzx). SN 2020abfe is in the DR2 sample, but due to a combination of a gap in the observed light curve and the interaction not altering the declining tail sufficiently, the tail fit procedure is unable to distinguish it from a normal declining SN Ia tail. SN 2020aejk was first detected after the final date for objects to be included into my sample. Two of the events in my sample (SN 2020eyj and SN 2020kre) are not presented in [Sharma et al. \(2023\)](#). SN 2020eyj was excluded as [Sharma et al. \(2023\)](#) focussed on interaction with H-rich material and this object showed He emission lines suggesting interaction with He-rich material ([Kool et al., 2023](#)). SN 2020kre is not in the BTS sample and therefore, not included in [Sharma et al. \(2023\)](#). However, it was confirmed with spectroscopy to have H α emission in its peak spectra.

Out of the 13 events SN 2020aeuh is an outlier, due to its distinct light curve. While the other 12 known Ia-CSM events detected in my sample have decline tails whose slopes are significantly shallower than for a normal SN Ia or steepen over time, SN 2020aeuh brightens significantly, having a double peaked nature with the second

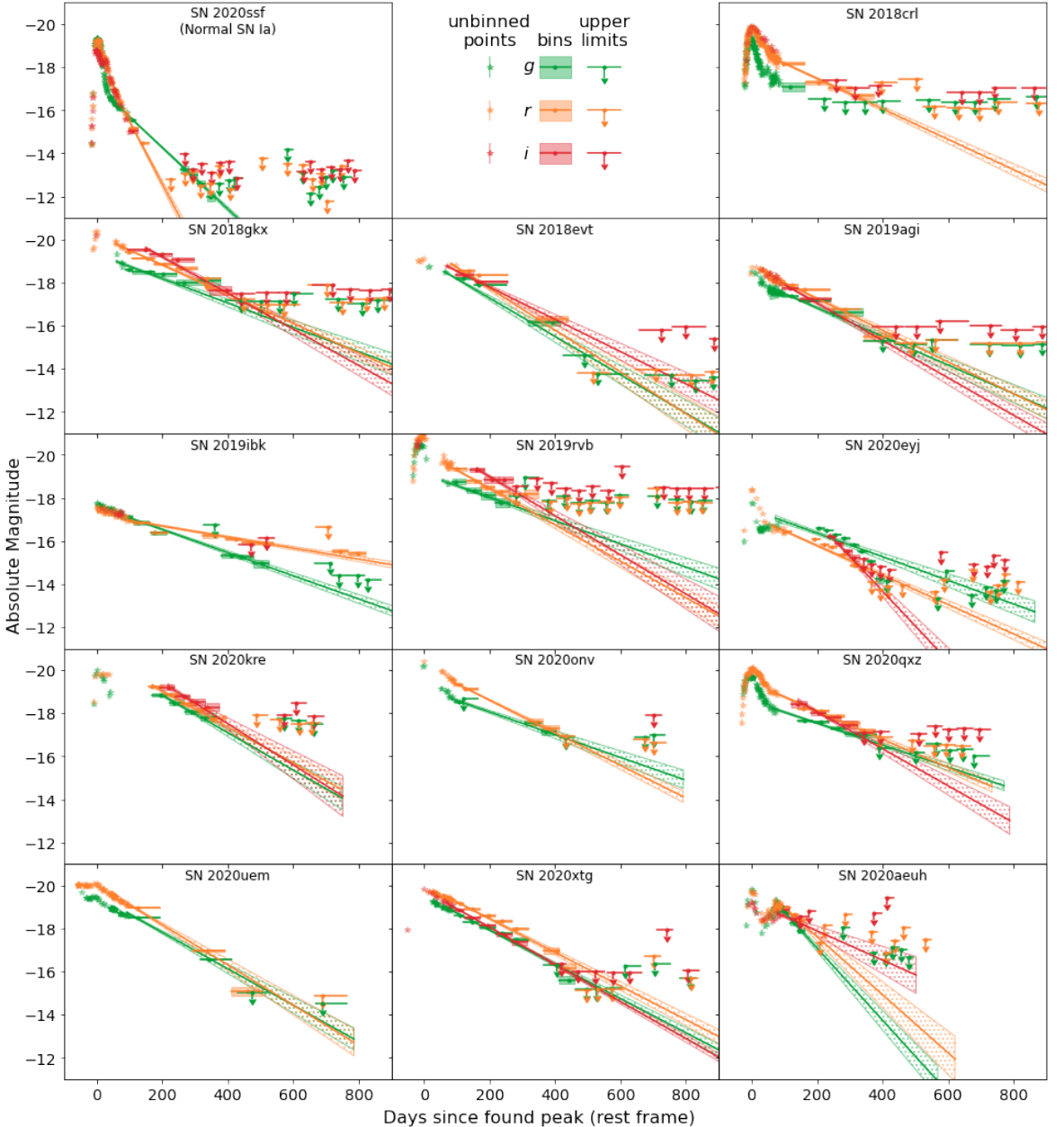


Figure 3.6: Binned late-time observations of the recovered known SNe Ia-CSM. All objects are shown in absolute magnitude and over the same time range for easy comparison. All objects are detected beyond 100 days after the peak without using the binning technique. I do not show these individual data points to increase readability. The tail fits are shown as solid lines with the hashed region denoting their 1σ uncertainties. For comparison, SN 2020ssf (ZTF20abyptpc) in the top left corner is a normal SN Ia with a normally declining tail with $t_{1/2,g} = 53 \pm 1$ days and $t_{1/2,r} = 26 \pm 1$ days. The fitted tails for the SNe Ia-CSM are significantly shallower.

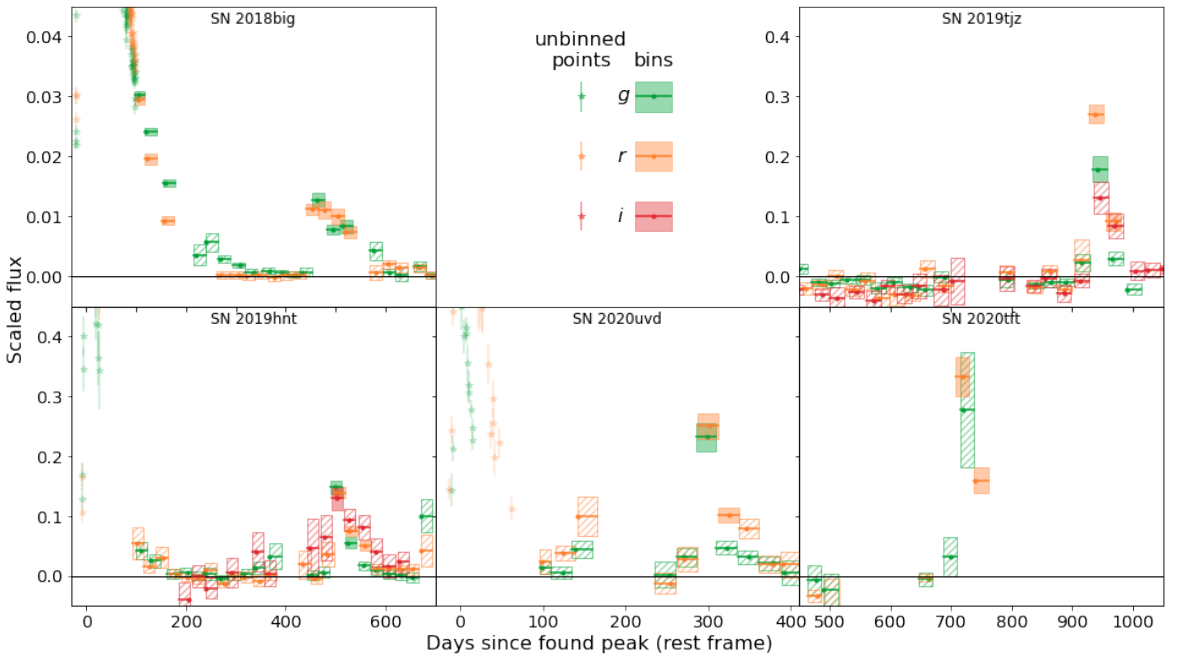


Figure 3.7: Binned late-time observations in flux space of the five events with a detected sibling, with the flux normalised to the found peak flux. All objects are plotted on the same flux scale for easy comparison except for SN 2018big, as its late-time detections are much weaker compared to the original SN peak magnitude due to the larger distance offset between the siblings.

peak at around 100 d after the first. Even though the light curve suggests the SN to be interacting, no H emission ($H\alpha$ or other lines) are observed. Kool et al. (in prep) present a detailed analysis of this object.

3.3.1.2 Siblings

Siblings are transients that occur in the same host galaxy as each other and can be useful for understanding differences in local environments (e.g. Biswas et al., 2022; Graham et al., 2022a). In some cases, the siblings occur in (almost) the same place on the sky, only differing in explosion time. This can be either due to the two transients being physically close together, or a projection effect due to the inclination of the host. However, the result is the same: forced photometry at the location of one sibling will result in a (partial) recovery of the other. Assuming that the first transient is a SN Ia in my sample and the second transient is fainter, my pipeline will flag the late-time rebrightening as a late-time excess in one of my objects.

Careful examination of the images using SNAP and cross-referencing using Fritz (an

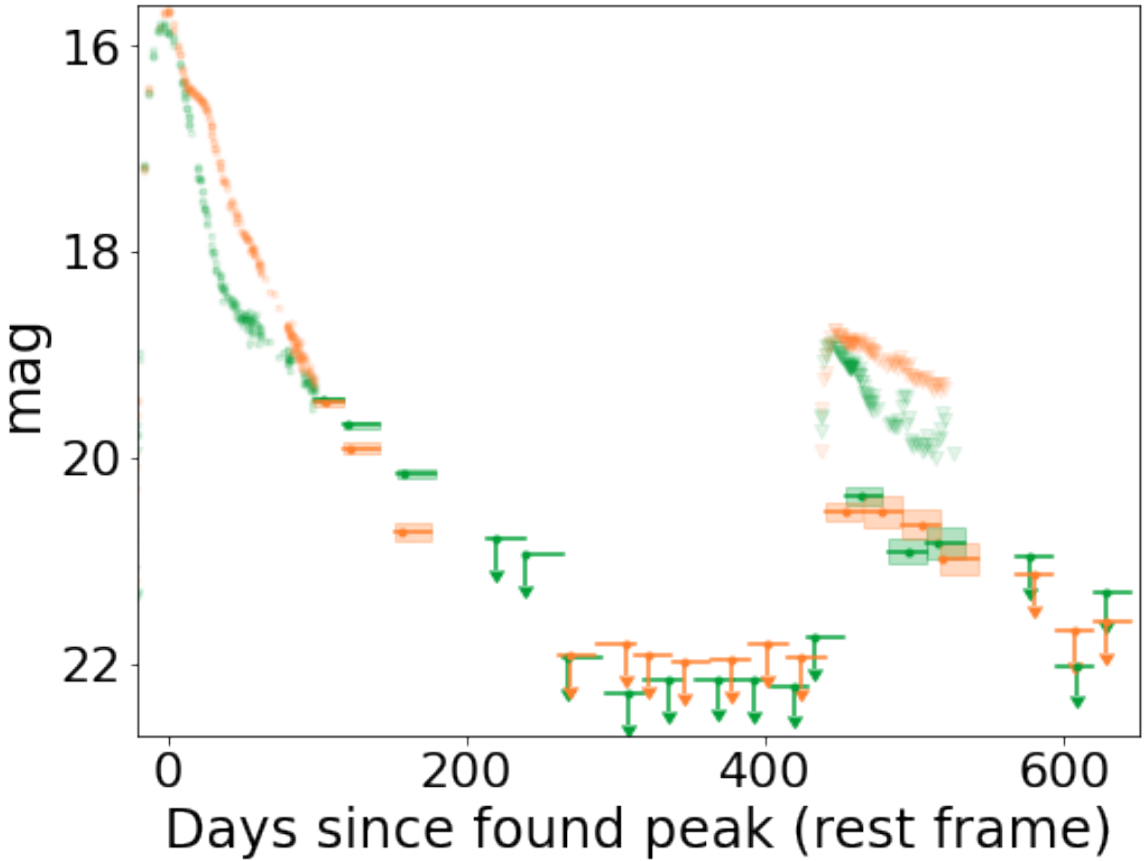


Figure 3.8: Light curves of SN 2018big and its sibling SN 2019nvm in magnitude space using bins of 25 d. The g (green) and r (orange) bins follow the tail of SN 2018big until it disappears in the noise. About 450 d after the peak of SN 2018big, new detections are identified in the binned photometry. The individual observations remain upper limits, although their shape hint to the true nature of these late-time detections.

Table 3.3: Objects with a detected sibling transient.

Primary name	IAU name	Sibling name	IAU name ^b	Type	Date ^a	Offset ('') ^c
ZTF18aasdted	SN 2018big	ZTF19abqhobb	SN 2019nvm	IIP	58 714	3.7
ZTF19aaysiwt	SN 2019hnt	ZTF20acwpads	-	-	59 186	1.2
ZTF19acihxzx	SN 2019tjz	ZTF18aanhpII	-	-	59 774	1.2
ZTF20abzetdf	SN 2020tft	-	-	Ia	59 867	< 1
ZTF20acehyxd	SN 2020uvd	ZTF21abouuow	SN 2021udv	Ia	59 422	3.1

^aMJD of the first detection of the sibling.

^bThe siblings ZTF19aaysiwt and ZTF20acwpads share an IAU name. For ZTF20abzetdf, the siblings are too close together ($<1''$ separation) to be automatically recognised as separate events, causing them to share both ZTF and IAU names. ZTF18aanhpII is a sibling transient in 2022 on top of the host nucleus, resulting in the internal name being from 2018.

^cAngular separation on the sky between the siblings.

alert broker, [van der Walt et al. 2019](#); [Duev et al. 2019](#); [Kasliwal et al. 2019](#); [Coughlin et al. 2023](#)) and the Transient Name Server¹ (TNS) showed that there are five objects in my shortlist whose late-time detections are due to a sibling. Figure 3.7 shows the binned light curves of these objects in flux space. In each light curve there is a sudden significant spike in the detected fluxes in all observed bands, which falls back down again after a short period of time. Table 4.3.2 lists the name and type of each sibling if known, as well as their sky separation. In some cases the siblings are close enough together that they are not automatically recognised as separate events, resulting in them having the same name. In the case of SN 2019tzj the sibling (ZTF18aanhpII) exploded close to the nucleus, which had some spurious detections in 2018. This caused the sibling to have a 2018 ZTF name, although it exploded in 2022.

Figure 3.8 shows the detection of a sibling (SN 2019nvm) in the late-time light curve of SN 2018big in magnitude space. SN 2019nvm is slightly offset ($\sim 4''$) from the location of the original SN. The photometry pipeline forces the point spread function (PSF) fit at the position of SN 2018big. As the position of SN 2019nvm is slightly offset, only some of the total flux of SN 2019nvm is captured in the fit. Besides these five siblings, I identified two other pairs of siblings with SNAP: SN 2019gcm and SN 2021fnj, and SN 2020jgs and SN 2021och. These siblings were too far apart to be picked up with the forced photometry (9.6 and 10.8'', respectively) but were found while inspecting using SNAP. For a complete list and study on the siblings found in the ZTF DR2, I refer the reader to Dhawan et al. (in prep.).

3.3.1.3 Kinked tails

This group consists of five objects where the simple tail model, based on the typical decline rate of SNe Ia based on SN 2011fe ([Dimitriadis et al., 2017](#)), failed to fit the observations at later times. The reason for this failure in four of the events is that there is a slow-down in the *r*- and *i*-band decline rates at $\sim 200 - 250$ d after peak, which the model does not take into account. The fifth event, SN 2020sck ([Dutta et al., 2022](#)), is

¹<https://www.wis-tns.org/>

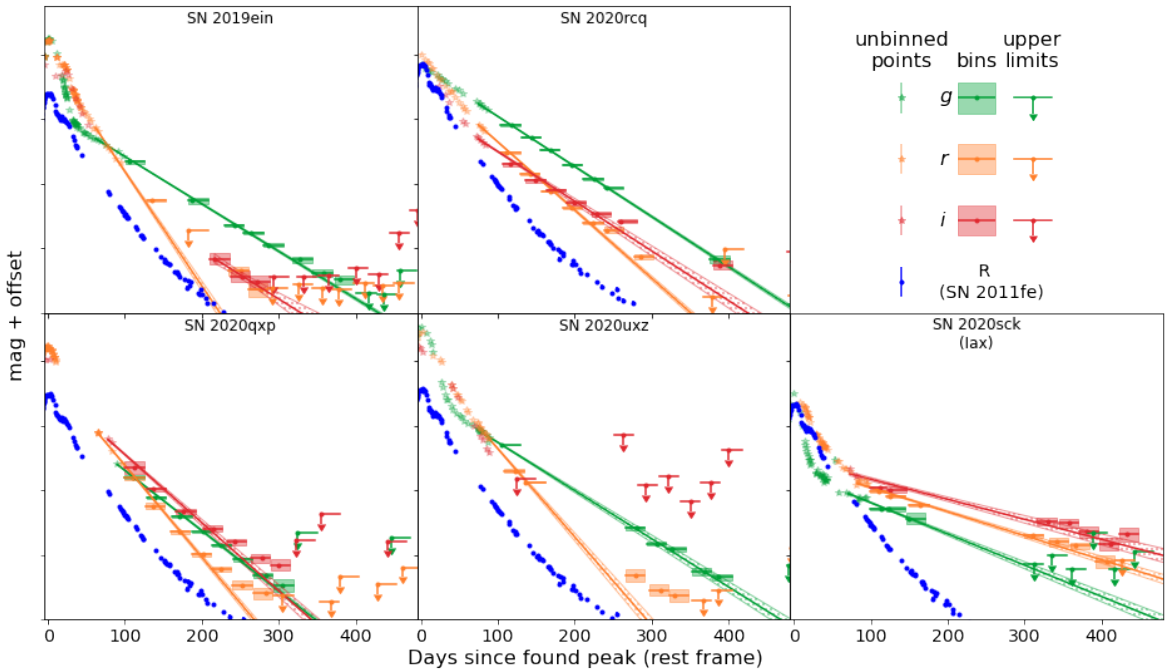


Figure 3.9: Five objects with kinks in their tails that start to deviate from the assumed decline rate at $\sim 200 - 250$ d post peak are shown in magnitude space as a function of days since peak. As most of these objects have their peak magnitude blinded, no scaling is shown. A normal radioactive decay model was fitted to these tails, shown as solid straight lines with their 1σ uncertainty as dashed regions. But as the ejecta opacity changes over time so does the half-life time of the tail, causing a kink seen in the bins which is not reproduced by the model. The arbitrarily normalised R -band light curve of SN 2011fe (known not to have CSM interaction from detailed spectral studies) (Zhang et al., 2016) is shown in blue, showing the same shift in decline slope at a similar phase.

a known SN Iax, a subclass known for having lower ejecta velocities and luminosities, suggesting that the explosion did not necessarily fully disrupt the star (Jordan et al., 2012; Kromer et al., 2013). This event was flagged because of a slow-down in its decline rate roughly 80 days after the identified peak. The change in slope is visible in all bands and significantly longer than the assumed $t_{1/2} = 50$ d of normal SNe Ia. The presence of a bound remnant has been suggested to be the cause of similar late-time signatures seen in other SNe Iax (Kawabata et al., 2018; McCully et al., 2022; Camacho-Neves et al., 2023).

The four SNe objects that deviate from the simple tail model are very nearby ($z \leq 0.009$) compared to the majority of ZTF DR2 sample and when using the binned observations they are bright enough to be detected up to (nearly) a year after their first detection. As Rigault et al. (in prep.) are using these nearby events to calibrate their H_0 measurement, their peak magnitudes are currently blinded. Figure 3.9 shows the g -, r -, and i -band light curves of these objects in magnitude space. The R -band light curve of SN 2011fe (Zhang et al., 2016), which had a similar change in decline slope, is also shown for comparison. As discussed in Dimitriadis et al. (2017), the radioactive decays produce γ -rays and positrons, as well as X-rays and electrons that can be thermalised, depositing their energy in the expanding SN ejecta. As the ejecta expand over time they become more transparent, shortening the delay between thermalisation of the deposited energy and the emission of optical radiation. This results in the SN tail slope changing as the opacity changes.

To be able to observe a change in decline slope such as this, a SN has to be both bright and well observed during the time it is visible. The other SNe Ia in my sample at similarly low redshifts have gaps in their observations or the change in slope is not strong enough for the tail fits to fall outside the allowed range of reduced chi-squared values ($\chi^2_{\text{red}} > 5$) and therefore, are not flagged by the pipeline due to this.

Table 3.4: Results of the additional tests for the ten promising objects. The host separation is given in " and converted to kpc using the redshift given in Table 3.2 and the same cosmology as was used in Section 3.2.4.4. In the final five columns the similarity of each SN Ia with a late-time excess is compared to different transient classes to see if the late-time signal can be interpreted as another transient. This can be excluded based on an inconsistent colour (1), duration (2), and/or an excessive amount of host extinction (3) needed to obtain the observed magnitudes.

Name	Red. error ^(a)	Host separation (")	$E(B - V)_{\text{host}}$ (mag.) ^(b)	AGN ^(c)	Approx. mag. ^(d)	SN Ia?	Ib?	Ic?	HIP?	TDE?	
SN 2018grt*	no	0.36 ± 0.03	0.32 ± 0.02	$0.21 - 0.36$	no	-16.5	no (23)	no (23)	no (2)	no (3)	no (13)
SN 2020pkj	no	0.52 ± 0.02	0.28 ± 0.01	$0.23 - 0.36$	no	-15.4	yes	yes	yes	no (23)	no (13)
SN 2019ldf*	no	0.65 ± 0.04	0.78 ± 0.05	≤ 0.03	no	-16.4	no (123)	no (123)	no (123)	no (123)	no (13)
SN 2019mse	no	0.59 ± 0.05	1.09 ± 0.10	0	no	-17.5	no (2)	no (2)	no (2)	no (2)	yes
SN 2019rqn	no	1.39 ± 0.08	2.21 ± 0.13	≤ 0.04	no	-16.8	no (13)	yes	yes	no (1)	no (13)
SN 2019vzf	no	3.89 ± 0.08	4.86 ± 0.10	0	yes	-	-	-	-	-	-
SN 2020awr	yes	19.60 ± 0.04	31.65 ± 0.07	-	-	-	-	-	-	-	-
SN 2020alm	no	0.67 ± 0.07	0.85 ± 0.09	≤ 0.05	no	-16.9	no (123)	no (12)	no (23)	no (123)	yes
SN 2020kzd	yes	4.67 ± 0.04	8.07 ± 0.07	-	-	-	-	-	-	-	-
SN 2020tfcc*	no	0.21 ± 0.02	0.14 ± 0.01	≤ 0.12	no	-16.8	no (123)	no (12)	no (23)	no (123)	no (3)

^(a)Reduction error: Comparison between the standard light curve reduction and scene modelling identified issues with the baseline correction (see Section 3.3.2.1).

^(b)Estimated assuming the main peak is a normal SN Ia. When correcting for Milky Way extinction and distance is enough to exceed an absolute *g*-band magnitude of -19.3, I quote a host $E(B - V) = 0$ mag.

^(c)The presence of an AGN was estimated using the WISE colours of the host and the criteria of [Hviding et al. \(2022\)](#).

^(d)Mean absolute magnitude of the *r*-band late-time excess after correction for Galactic and host extinction, averaged over the host extinction range considered.

3.3.2 Additional tests of promising events

After performing the tests discussed in the previous sections on each event, there are ten objects remaining with an unexplained late-time excess. Light echoes produced by SN light scattering off of nearby dust clouds were considered, but were ruled out as these are typically ≥ 10 mag fainter than the SN at its peak ([Patat, 2005](#); [Graur et al., 2016](#)). I performed several additional tests on these ten events to try to determine the origin of their late-time excess. The first is using SMP as described in Section 3.1.1. The second is testing for coincidence with an AGN and third is more detailed comparisons with known transient classes. These tests are discussed below and a summary is shown in Table 3.4.

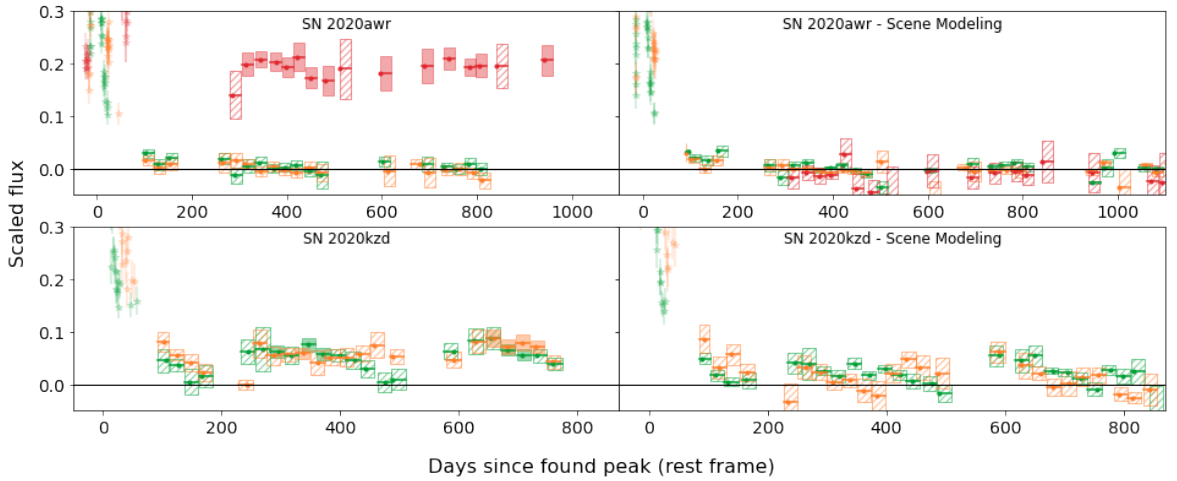


Figure 3.10: Two objects whose late-time detections were revealed to be caused by the photometry extraction. The colours are as in Fig. 3.9. The left side shows the binned forced photometry light curve, and the right side shows the binned SMP light curve. Bins with 5σ detections are shaded solid, while the non-detections are hashed.

3.3.2.1 Scene modelling photometry

To test for issues in data processing, The ten events were run through the scene modelling pipeline of Lacroix et al. (in prep.) as discussed in Section 3.1.1. Two SNe Ia (SN 2020awr and SN 2020kzd) were found to have issues with their difference imaging and forced photometry light curves, causing false detections. The detections in both these events are close to the detection limit and therefore, are impacted by even small errors in the baseline placement. The difference imaging (left panel) and scene-modelling (right panel) light curves of these two events are shown in Fig. 3.10.

For SN 2020awr, ~ 300 d after the SN peak, the i -band observations jump up to detections at ~ 20.3 mag. In contrast to other objects where baseline issues were found, here the offset occurs only for part of the light curve, while the pre-SN baseline has no visible issues. I could not identify a clear reason for this when inspecting the images with SNAP, and the SN is too far away from the host nucleus for it to be host activity. For the scene-modelling version of the photometry, the jump in the i -band observations has disappeared completely, showing that there was indeed an unidentified issue with the i -band data for this object. Since the late-time detections are determined to be spurious, this object is ruled out from having late-time detections.

In the case of SN 2020kzd, late-time detections are present in the g - and r -bands

Table 3.5: Details of the comparison transients used to test if late-time detections could be explained by another transient at a similar sky position. The first column shows the assumed type of transient, the second shows the transients used to represent each type, the third has the approximate absolute extinction-corrected r -band peak magnitudes, and the fourth the reference for each event.

Type	Name	Peak abs. M_r (mag.)	Reference
SN Ia	SN 2011fe	$-18.4 - -19.4$	Mazzali et al. (2014)
SN Ib	SN 2019yvr	-17.9	Kilpatrick et al. (2021)
SN Ic	SN 2021krf	-17.3	Ravi et al. (2023)
SN IIP	SN 2020jfo	-17.8	Ailawadhi et al. (2023)
SN IIP	SN 2017gmr	-18.7	Andrews et al. (2019)
TDE	AT 2018hco	-22.1	van Velzen et al. (2021)
TDE	AT 2018zr	-20.1	van Velzen et al. (2021)

for hundreds of days (see Fig. 3.10). The SN is in a complex environment with three galaxies close to its sky position, which likely complicates the image subtraction and baseline correction. When SMP is performed on the event the detections disappear and average flux at late times is consistent with zero, showing that the binned forced photometry light curve likely suffered from a wrongly determined baseline correction.

3.3.2.2 AGN contamination

If a SN explosion site is coincident with a host galaxy that has an AGN, host activity is a likely cause of the late-time detections. Using data from the Wide-field Infrared Survey Explorer (WISE; [Wright et al. 2010](#)), [Hviding et al. \(2022\)](#) present a criterion to test if a galaxy hosts an AGN based on the WISE $W_1 - W_2$ and $W_2 - W_3$ colours, which I apply to my events. One object (SN 2019vzf) is 4.86 kpc of its host centre and its host is a known AGN, with WISE colours of $W_1 - W_2 = 0.55 \pm 0.03$ and $W_2 - W_3 = 2.90 \pm 0.04$ mag. In SNAP, the late-time signal appears to cover both the SN and AGN locations. The AGN contamination is too strong to put any meaningful constraints on the late-time flux at the SN location. I kept the object in my sample until now to test if it is possible to use scene modelling to reduce the AGN contamination. However, this is not possible. I attribute the late-time signal to host activity and disregard it in future discussion. The light curves of SN 2019vzf are shown in Fig. 3.11.

3.3.2.3 Presence of a sibling close to the SN location

To test if a previously unidentified sibling transient is causing the late-time detections of the remaining seven objects, I compared their late-time light curves to known classes of transients, including a SN Ia, core-collapse SNe (Type Ib, Type Ic, Type IIP) and two tidal disruption events (TDE). Firstly, I have estimated the amount of potential host extinction from the main SN peak by assuming it was a normal SN Ia with a typical *g*-band peak of -18.8 to -19.3 mag after correcting for the distance to the SN and for Milky Way extinction. These estimated host extinction values are given in Table 3.4, assuming $R_V = 3.1$. The bright end of the absolute peak magnitude gives an upper limit for the host extinction, and the faint end gives a lower limit. After correcting for this range of additional host galaxy extinction, the late-time excesses have mean absolute *r*-band magnitudes of -15.4 to -17.5 mag (see Table 3.4).

After estimating the allowed extinction for each primary SN Ia, I initially assumed that if the late-time excess is due to another transient then it will have the same extinction along the line-of-sight. For these other transients, I used examples of a SN Ia, Ib, Ic, two IIPs, and two TDEs to compare against, with details of the comparison objects described in Table 3.5. The transients chosen to represent their category are all in the typical magnitude range for their type. Two TDEs and SN IIPs were chosen to represent the upper and lower end of the range of peak magnitudes expected for these transients. I use my model for SN 2011fe to represent SNe Ia and test the lower and upper edge of the range of normal SN Ia peak *r*-band magnitude.

These comparison objects were chosen as they have well-sampled light curves in the ZTF filters, and literature values for the host extinction. I correct the light curves of the comparison objects using their literature redshifts and their extinction values before correcting for the redshift and extinction of each SN Ia in my sample with a potential late-time excess. I then compare this transient light curve to the found late-time detections to see how well they match. A good match will have a similar magnitude, colour, and duration.

It could be the case that the suspected sibling was in the same line-of-sight direction, but had a different amount of extinction due to, for instance, exploding behind a cloud that adds additional extinction. I check this by adding enough extinction to match the r -band detections between the different comparison events and the observed late-time detection and again check if the colour and duration match up, as the observed colour is affected by the extinction. For the TDE comparisons, I allow a host galaxy $E(B - V)$ of up to one magnitude, as was estimated for the ZTF TDE sample of Hammerstein et al. (2023).

For four events (SN 2019mse, SN 2019rqn, SN 2020alm, and SN 2020pkj), the late-time detections are consistent with at least one of the comparison classes, as detailed in Table 3.4 and shown in Fig. 3.11. I describe them individually in the following sections. The three remaining events (SN 2018grt, SN 2019ldf, and SN 2020tfc) cannot be explained by the presence of a sibling transient and are discussed further in Section 3.3.2.4.

SN 2019mse. SN 2019mse has late-time detections starting at 450 d after the peak and lasting \sim 250 d in the gri -bands with an absolute r -band magnitude of -17.5 mag during the excess. Careful re-examination of the difference images show that the late detections are slightly offset (about one pixel) from the SN location, and appear to be on the host nucleus location instead. However, with its WISE colours being $W1 - W2 = 0.25 \pm 0.04$ and $W2 - W3 = 2.44 \pm 0.09$, the host is determined to not contain an AGN. The scene modelling version of the light curve shows a similar late-time excess, showing that this is not an artefact from the chosen photometric analysis method.

The late-time signal is detected in all three bands, and its behaviour is very similar in all of them (see Fig. 3.11). Its rise and decline time scales, absolute magnitude, and colours agrees well with the ranges seen for TDE. Together with the observation that the late-time detection are at the host nucleus location, this suggests that a nuclear transient explains the late-time signal adequately.

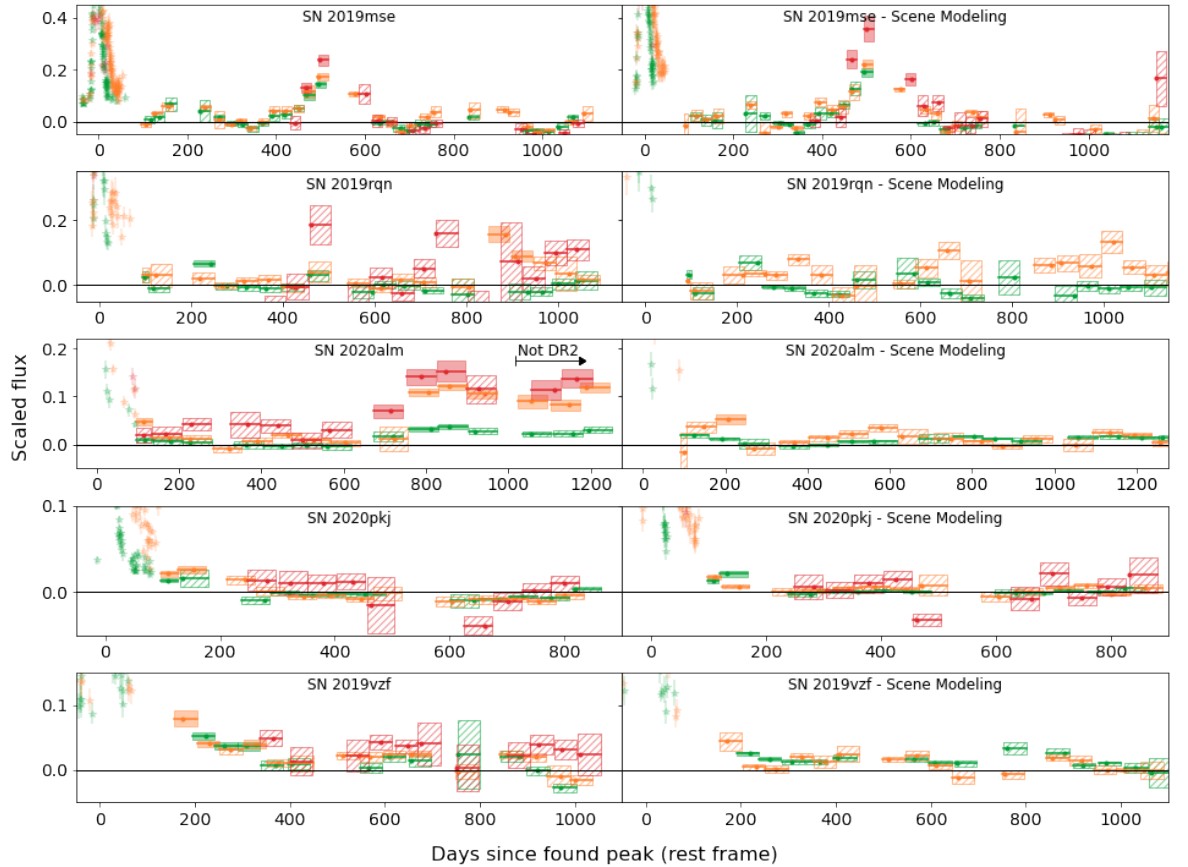


Figure 3.11: Objects whose late-time detections are explained in the additional tests. The top four rows show the light curves of the objects where a previously undetected sibling transient as an explanation for the late-time observations could not be ruled out, with forced photometry light curves in the left-hand panels and the scene modelling photometry light curves in the right-hand panels. The 5 σ detections are shown as bins with solid uncertainty regions and bins with hashed uncertainty regions are non-detections. The object whose late-time detections are caused by the host galaxy AGN, SN 2019vzf, is shown in the bottom row. The colours are as in Fig. 3.9 with gband in green, rband in orange, and iband in red.

SN 2019rqn. In the case of SN 2019rqn, there is a short period of detections at $950 - 1050$ d in the r -band after a gap in the observations, declining and fading below the detection significance within 100 d of the first detection. Nothing is detected at a $\geq 5\sigma$ level in the g - or i -band observations. The i -band SMP light curve had its host contribution not completely subtracted, causing a flux offset in the data points. I therefore do not consider the SMP i -band further. The data points in the g - and r -band light curve have slightly larger uncertainties in the SMP version, causing the main SN light curve to fall below the 5σ threshold at an earlier epoch resulting in fewer individual points visible (Fig. 3.11). Similarly, larger uncertainties for the SMP prevents the detection of a late-time r -band signal.

Assuming a sibling exploded during the gap in the observations between 870 and 950 d post peak, SNe Ib and Ic with $E(B - V) \leq 0.3$ mag extinction in the r -band can fit their tail to match the observed detections in the r -band without being excluded by the g -band and i -band non-detections. Therefore, I cannot rule out a sibling as the source of the detected late-time signal.

SN 2020alm. The late-time signal in SN 2020alm is seen in all three bands, beginning at ~ 750 d after the peak and lasting for at least 300 d. There is a gap of 80 d in the observations immediately before the period of activity. The detections slowly rise to a plateau. My initial analysis only included data for SN 2020alm up to ~ 1000 d after the peak. However, when this object was identified as having late-time detections, the light curve pipeline was rerun and it was found to be still bright at later times, with significant detections in the r - and i -bands, but not above 5σ detections in the g -band. The i -band SMP light curve contained a significant flux offset, as the host was not fully subtracted. I therefore do not further consider this band. The binned SMP r -band light curve fails to reproduce the late-time detections found in the forced photometry light curve. However, the g -band detections are recovered in the SMP. The SN is close to the host nucleus at $0.66''$ (0.85 kpc) offset at the redshift of the SN, but the WISE colours of $W1-W2 = 0.06 \pm 0.04$ and $W2-W3 = 2.42 \pm 0.12$ place it far

outside the AGN region.

As SN 2020alm was still active while my analysis was on-going, Two spectra were obtained using the Optical System for Imaging and low-Intermediate-Resolution Integrated Spectroscopy (OSIRIS+) instrument on the Gran Telescopio CANARIAS (GTC) at Roque de los Muchachos in La Palma on 26 July 2023 using the R1000R grism. As the spectrum is heavily dominated by the host galaxy, I subtracted a re-binned spectrum of the host taken by the Sloan Digital Sky Survey (SDSS, [York et al. 2000](#); [Adelman-McCarthy et al. 2006](#); [Gunn et al. 2006](#); [Smee et al. 2013](#)) in 2003, well before the SN occurred. I confirmed successful host subtraction by checking for residual Na ID and Mg I $\lambda 5175$ absorption lines and found that no residual features were present. A more detailed explanation is given in Appendix [3.8. appendix to section?](#)

The resulting spectrum shows an excess that is stronger towards longer wavelengths (Fig. [3.15](#)). This is consistent with the broadband photometry finding an brighter excess in the redder bands, while the *g*-band remains within the noise after binning the observations. There is some excess in the narrow [N II] $\lambda\lambda 6548, 6583$, H α and [S II] $\lambda\lambda 6716, 6730$ emission lines, but I lack the resolution to check if this is significant. There is no visible additional H α component in the spectrum, which would be indicative of CSM interaction. Integrating the spectrum over the *r*- and *i*-band efficiencies gives an *r*–*i* colour of 0.6 mag, which is within 3σ of the value found in the latest photometry bin.

[Hammerstein et al. \(2023\)](#) show that TDEs generally have a *g*–*r* colour of zero and can have featureless spectra. I approximate a TDE by a flat line in order to estimate the amount of extinction needed to generate a red excess similar to the spectrum. I find that the general shape of the spectrum can be approximated with $0.6 < E(B - V)_{\text{host}} < 1$ mag. This would mean an absolute *r*-band magnitude of $-18.8 > M_r > -19.8$ mag. [Hammerstein et al. \(2023\)](#) show that both this amount of host extinction and late-time brightness are possible for TDEs. They also show that it is possible for a TDE to rise and fall back down within the 80 d gap in observations, although this is seen in fainter TDEs than corresponding to my estimated absolute magnitude range.

The TDE sample of Hammerstein et al. (2023) did not contain a single object that matches my late-time detections in duration and luminosity in SN 2020alm. However, it is possible to combine parts of different TDEs together to make a TDE that peaked and decayed within the 80 d gap and levelled out by the time it became observable again. Based on this, a TDE is a plausible explanation for the late-time signal detected in this object.

SN 2020pkj. In the case of SN 20120pkj, the first r -band bin with a detection is the end of the normally declining tail, but after the first bin the detections rise slightly in the next r -band bin (Fig. 3.11). None of the binned photometry for the g - and i -bands give significant detections. Unfortunately, there is a gap in the observations immediately after the r -band detections preventing me from following its evolution closely at these phases. When it became observable again at >200 d, no significant detections were found in any band. The duration of the transient is at least 75 d and could be up to 150 d. In the SMP light curve of this object, a similar rise at the same epochs is recovered, though it is found in the g -band instead of the r -band. This is likely due to the low significance of these detections at just $5.8\text{-}\sigma$ in the r -band in the forced photometry and $5.2\text{-}\sigma$ in the g -band in the SMP, showing that they are just on the detection limit of my binning technique.

With a redshift of $z = 0.02456$, this object is nearby enough for the end of the tail to be visible in the bins at 100 days. This could explain why the first bin is a detection, but the slight increase is still unexpected for a normal SN Ia decline tail. While the second bin is marginally consistent with my tail fit, a slight but steady increase can be seen in the unbinned flux values as well, suggesting that the brightening is real.

Assuming that the detected part of the late-time signal is the brightest part of a sibling transient, the tested transients need significantly more extinction of ~ 3 to 6 mag in the r -band (depending on the comparison transient) than was found for the main SN Ia peak. However, the ~ 80 d gap is long enough for a Type I sibling SN to peak higher during the gap and dim again before observations resumed. The other transient could

have just started when it stopped being observable, and declined below the detection limit when the location became observable again. Since there is no constraint on the magnitude, this could work with any amount of extinction. Therefore, I cannot rule out conclusively that the late-time detections are due to another transient.

3.3.2.4 Late-time interaction candidates

Finally, I present the three objects (SN 2018grt, SN 2019ldf, and SN 2020tfc) whose late-time detections could not be explained by any of the explanations discussed above. Their light curves are shown in Fig. 3.12, and the colours of the late-time detections in Fig. 3.13 and the SMP light curves for SNe 2019ldf and 2020tfc in 3.16. A scene modelling analysis could not be performed for SN 2018grt due to it exploding early in the ZTF survey. The forced photometry pipeline uses images obtained during the ZTF commissioning phase as templates but the SMP does not. I present these three objects as late-time interaction candidates as there are no spectra of these objects at these late times to confirm the presence of features consistent with CSM interaction.

By using the estimated mean absolute r -band magnitude after removing all extinction effects (see Table 3.4) I can estimate the required $H\alpha$ flux assuming that it is the source of all the detected flux in the r -band, and that the emission line has the same width as was used during the simulations. The identified strength of the signal is compared to the $H\alpha$ signal detected in SN 2015cp for each of the events.

SN 2018grt. The late-time signal of SN 2018grt is only detected in the r -band, the g -band stays around zero flux, and there are no i -band observations at these phases. The first detection in the r -band begins at 1350 d post peak with a magnitude of 21.4 ± 0.2 (absolute magnitude of -16.4 mag). It varies little over the ~ 100 d period where it is detected, after which it returns to zero flux within 50 d. The SN is close to the host nucleus with an offset of $0.35''$ (0.32 kpc) but its host colours place it well outside the expected AGN region. Checking the difference images with SNAP shows that the host nucleus and SN location differ by ~ 1 pixel.

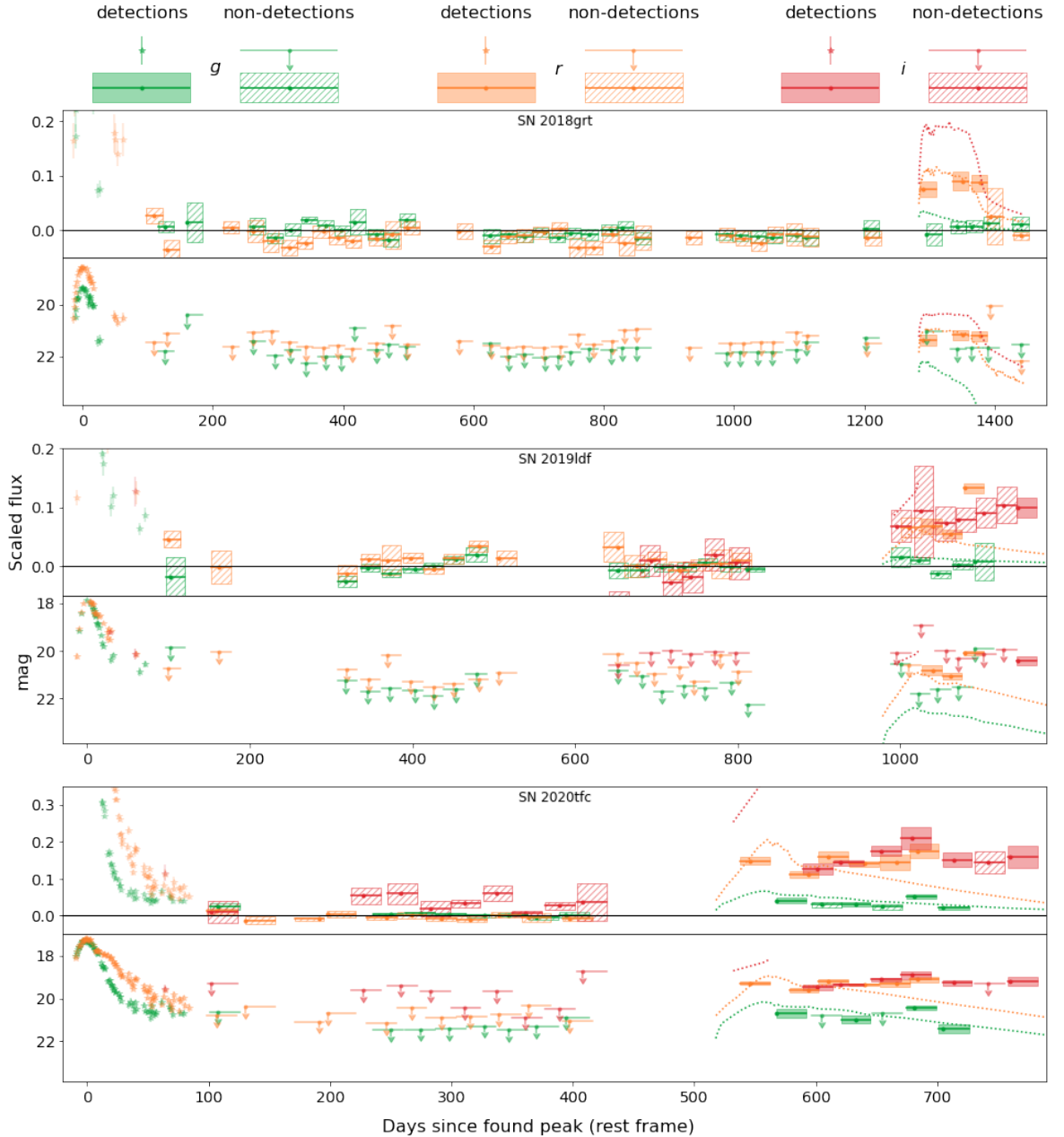


Figure 3.12: Three candidate objects, shown in magnitude and flux space. All three have significant detections ($\geq 5\sigma$) after a period of observations consistent with zero flux. From the alternative explanations the best fitting alternate transients are shown in dotted lines. For SN 2018grt this is the Type IIP SN 2017gmr, for SN 2019ldf and SN 2020tfc this is the TDE AT 2018hco.

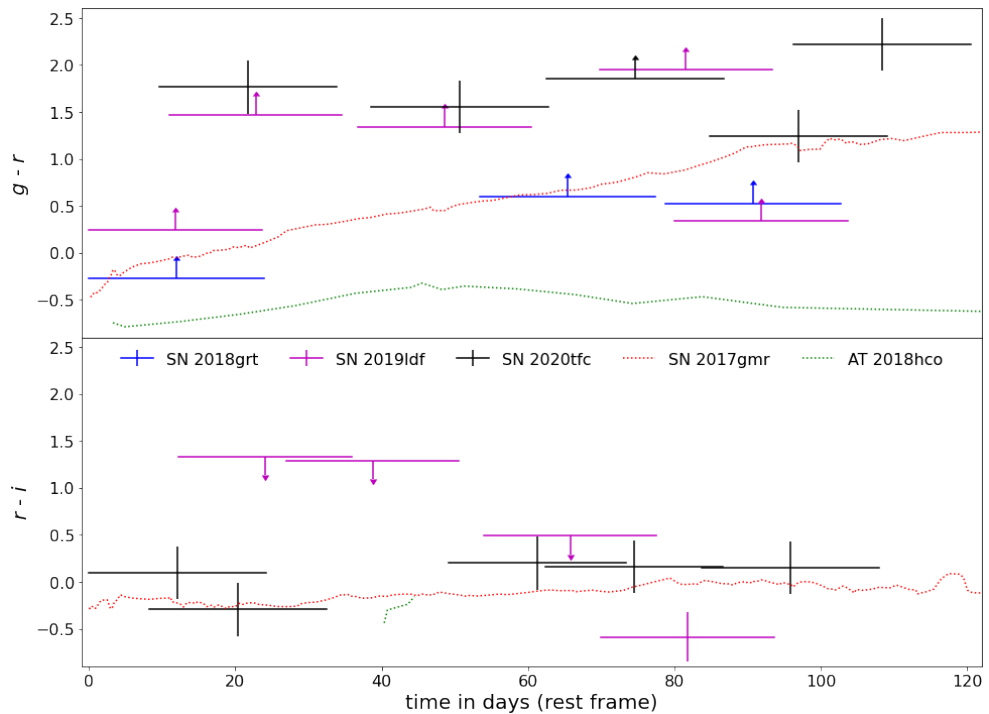


Figure 3.13: Colour curves of the three candidate objects, together with the colours of the best fitting alternate transients. The top and bottom panels show $g-r$ and $r-i$, respectively. The first bin for each object starts at zero days, but the bins can be shifted horizontally in an attempt to better fit the colour curve of the transient compared against (given that this is allowed by the rest of the light curve). Bins whose mean observation dates are closest to each other are used to calculate the colour, provided that these bins overlap in time. If there is a detection in only one band used to calculate the colour while the other is a non-detection, the result is a lower or upper limit.

The late-time detections are ~ 2.5 mag below the main SN peak. If the late-time signal is due to another SN Ia or a TDE, it would require a significantly higher extinction value than was found for SN 2018grt itself. In addition, this object shows a sudden drop in the r -band, which is not normal behaviour for a TDE. Most of the other transient types cannot reproduce the plateau followed by the sharp decline only detectable in the r -band, apart from a SN IIP, where the plateau of SN 2017gmr has nearly the same time span. However, to fit the observed magnitude with a IIP SN, it would require a host $E(B - V)$ that is three times higher than what was found for SN 2018grt, making this scenario less likely to be the case. Therefore, I conclude that late-time CSM interaction is a plausible scenario for the late-time signal in this object.

If I assume $0.21 \leq E(B - V)_{\text{host}} \leq 0.36$ mag and that the r -band signal is produced only by an $H\alpha$ emission line with a similar width to the one used in my simulations in Section 3.2.4, I estimate the strength of the emission to be much stronger than SN 2015cp, at 60 to 100 times its emission strength. However, there are examples of SNe Ia-CSM with interaction strengths this strong, for example, SN 2020eum was within this range ([Sharma et al., 2023](#)).

SN 2019ldf. SN 2019ldf has late-time detections in the r -band beginning at 1050 d after the peak and lasting for about 100 d, with an additional increase in brightness towards the end. There is a single 5σ detection in the i -band but there are a number of lower significance detections coeval with the r -band detections. These detections are directly after a long period without observations due to the object being behind the Sun. Nothing is detected in the g -band during the time of the rise in the r -band. The binned SMP light curve recovers these late-time r -band detections, and a single i -band detection, showing that these detections are not specific to the photometry method.

I compared the properties of the late-time detections to those of my comparison transient objects. Even if I assume that a SN exploded during the gap in observations in order to avoid needing a significantly larger $E(B - V)_{\text{host}}$ value, SNe evolve too much over a period of 100 days to explain the detections. In addition, detections would also

be expected in the g -band, which have not been found.

A TDE could fit the detections if it was intrinsically bright but heavily extinguished, as this could explain the red colour and absence of signal in the g -band. However, SN 2019ldf is offset from the host nucleus by $0.65''$ (0.78 kpc) and inspection of the difference images using SNAP shows that the late-time signal is more consistent with the SN location than the host nucleus location, disfavouring the TDE explanation. Therefore, I conclude that the late-time signal could be due to late-time CSM interaction.

The late-time detections persist until the end of the observation window. To determine if there were still signs of interaction once it was visible again, I obtained g - and r -band photometry with the EFOSC2 imaging spectrograph (Buzzoni et al., 1984) on the ESO New Technology Telescope (NTT) in La Silla, Chile on 2023 May 19 as part of the extended Public ESO Spectroscopic Survey of Transient Objects+ (ePESSTO+; Smartt et al. 2015).

To examine whether the SN is still detected in the images from May 2023, image subtraction techniques were used. Due to the lack of reference images in the g - and r -band filters from EFOSC2, images from the DESI Legacy Imaging Surveys Data Release 9 (Dey et al., 2019) were used. After aligning the images, They were subtracted from each other with the High Order Transform of Psf ANd Template Subtraction code version 5.11 (HOTPANTS; Becker, 2015). The brightness in the difference images was measured using aperture photometry. The photometry was calibrated against stars from DESI Legacy Imaging Surveys. The EFOSC2 and DESI Legacy Imaging Surveys filters are not identical which might add an unknown systematic to the reported photometry. The 5σ upper limits are $m_g = 24.7$ and $m_r = 24.3$ mag at 1397 days after the peak, with no detection in either band. This means that the signal has disappeared at this time, and thus could have lasted, at most, for about 500 days.

Assuming that the r -band signal is entirely due to the $H\alpha$ emission, I estimate it to be ~ 60 times as strong as the late-time interaction found in SN 2015cp. However, this assumption is very simplistic, as it completely disregards the rise in the i -band and therefore it is only a first order estimate.

SN 2020tfc. This object has late-time *gri*-band detections, beginning at 550 d after the peak and lasting for at least 250 days. While the *r*- and *i*-bands are at more or less the same magnitude, the *g*-band detections are about 1.3 mag fainter. This immediately poses an issue for any alternate transient considered, as either there is a low amount of extinction and a weak *g*-band signal, or there is a high amount of extinction and the intrinsic signal is even brighter in the *i*-band. This, combined with the fact that the signal lasts for several hundreds of days with little variation, disfavours a SN as an alternate transient explanation. The intrinsic colour also heavily disfavours a TDE as these objects tend to have a similar intrinsic brightness in the *g*-, *r*-, and *i*-bands. In the binned SMP light curve the late-time detections were confirmed in the *g*-band. The SMP *i*-band data points have a large scatter, most likely due to uncertain background removal because of a low number of available images for the SMP template. Therefore, I do not consider them further in my analysis. In the *r*-band SMP light curve, the data points are below my 5σ cut-off for detections, although one is very close to my limit at 4.6σ . However, the *g*-band detections seen in the forced photometry are confirmed by SMP suggesting a real signal is present at late-times in at least this band, and at lower significance in the *r*band.

Similar to SN 2020alm, the late-time signal was on-going during my analysis but unfortunately there is no archival host galaxy spectrum available to compare to. As the host dominates the late-time signal (the SN is at a distance of $0.28''$ (0.21 kpc) from the host nucleus) and cannot be removed using difference imaging or SMP as for the photometry, this prevented me from taking a spectrum of the late-time signal. With all alternate explanations ruled out or severely challenged by observations, the late-time CSM interaction remains as a plausible explanation for these late-time detections.

If I assume that the *r*-band signal is due to H α emission only, the interaction is estimated to be 110 to 150 times as strong as the interaction found in SN 2015cp. This is by far the strongest of the three, but again this simple assumption is unrealistic as it completely ignores the measured *g*- and *i*-band signal that suggests a contribution

Table 3.6: Parameters used for rate estimation simulations for each object.

Object	Start epoch (d)	Duration (d)	Strength (SN 2015cp)	N_{sample}	late-time CSM fraction	late-time CSM rate ($\text{Gpc}^{-3} \text{ yr}^{-1}$)
SN 2018grt (worst)	1 375*	100	60	748	$0.0084^{+0.0033}_{-0.0041}$	203^{+438}_{-97}
SN 2018grt (best)	1 275*	200	100	988	$0.0015^{+0.0032}_{-0.0007}$	36^{+76}_{-18}
SN 2019ldf (worst)	1 050*	200	60	1 931	$0.0019^{+0.0036}_{-0.0009}$	45^{+87}_{-22}
SN 2019ldf (best)	875*	500	60	2 505	$0.0023^{+0.0038}_{-0.0011}$	54^{+91}_{-26}
SN 2020tfc (worst)	550	250	100	3 439	$0.0004^{+0.0009}_{-0.0002}$	10^{+22}_{-5}
SN 2020tfc (best)	450	500	150	3 493	$0.0003^{+0.0008}_{-0.0002}$	8^{+20}_{-4}

For each of the three SNe I assumed a worst and best case scenario for detecting them in my sample, giving upper and lower limits for a simulated observing campaign. The efficiency curves generated from these simulations were then used to determine the intrinsic fraction of SNe Ia with late-time CSM interaction in an MCMC process, with the assumption that only one object was recovered in a sample size that is the same as the amount of DR2 objects with observations after the start epoch (N_{sample}). The last two columns show the found late-time CSM interaction fraction of the total SN Ia rate and the late-time CSM interaction rate.

*When the start epoch of the late-time excess is >750 d, 750 d is used as the start epoch because of limitations of the available ZTF survey plan. See Section 3.3.3 for more details.

from a continuum or other spectral lines to the late-time signal.

3.3.3 Late-time CSM interaction rates based on my candidate objects

I identified three objects (SNe 2018grt, 2019ldf, and 2020tfc) with potential late-time CSM interaction signatures. For SN 2018grt and SN 2019ldf, these detections were in the r -band (with no i -band data available for SN 2018grt and low significance i -band detections for SN 2019ldf). For SN 2020tfc, late-time detections were found in all three bands (gri). In my initial simulations to determine my recovery efficiency (Section 3.2.4), I made the assumption that any CSM interaction would be dominated by $\text{H}\alpha$ emission that would be present in only the r -band up to $z \sim 0.07$ and in the i -band beyond that. This was based on the dominant interaction signatures seen in SNe Ia-CSM and also the one event with late onset interaction, SN 2015cp (Graham et al., 2019b).

In Graham et al. (2019b), the Ca II NIR triplet emission was also identified in its

spectra, along with emission consistent with Mg I $\lambda 5175$. [Harris et al. \(2018a\)](#) speculated that although the Ca II NIR region was very noisy, the Ca II emission may be a similar strength to the H α emission. For SN 2019ldf at a redshift of 0.057, the Ca II NIR triplet, if present, would be partially shifted out of the *i*-band, which could potentially explain its low-significance *i*-band detections. SN 2020tfc is at lower redshift (0.031) so the Ca II NIR triplet would fall completely in the *i*-band and could potentially be the source of the *i*-band detections. The strength of the potential Mg I $\lambda 5175$ line in SN 2015cp was weak and not well constrained ([Graham et al., 2019b](#)) but could potentially result in a weak signature in the *g*-band. However, without spectral confirmation this is only speculation.

The other difference between my initial simulations for determining recovery efficiency and the observed detections in my three candidate late-time CSM objects is that the late-time CSM interaction signature is much stronger in the observed events. In my three candidates, the late-time signal is between 2 to 3 magnitudes below the SN peak magnitude, while in the simulations with strongest interaction the signal was about 4.4 magnitudes below the peak.

It is clear from my candidate events, that there is significant diversity (detected bands, timescales and strengths) in their potential CSM signatures and without knowledge of their underlying spectra (e.g. emission lines that are present), it is difficult to develop spectral models and run simulations covering this full diversity. Therefore, although very simplistic and ignoring other potential emission lines occurring in the *g*- and *i*-bands as were seen in SN 2015cp ([Graham et al., 2019b](#)), I focussed on H α emission dominated models and the corresponding *r*-band detection efficiency to estimate a rate of late-time H α emission dominated CSM interaction based on my three candidate objects. I use the same underlying spectral model (SN 2011fe combined with H α emission) as detailed Section 3.2.4 in further SIMSURVEY simulations but constrain the strength and timescale of the CSM signature based on my three events. In Table 3.6, I show the range of start epoch, duration and strength (dependent on assumed host galaxy extinction) simulated for each event. For each of the three objects, I take the

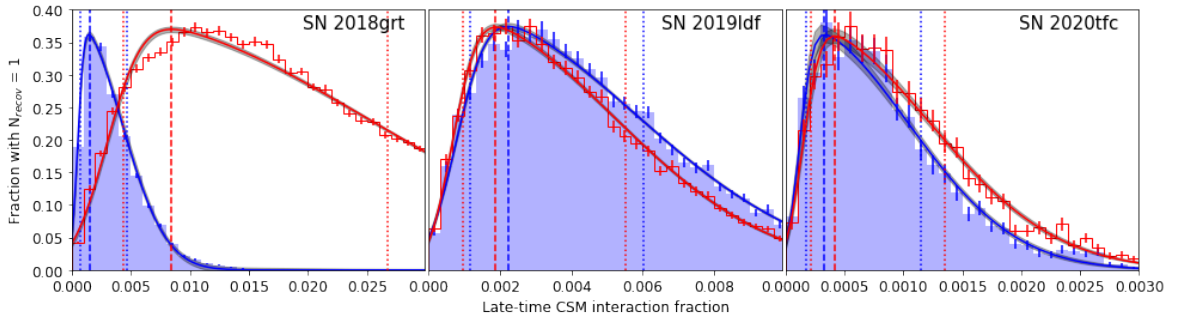


Figure 3.14: Fraction of MCMC realisations per bin that resulted in one object being recovered in a sample with the same size as the effective DR2 sample size as a function of the late-time CSM interaction fraction. The best and worst case scenario for each object is shown in blue and red, respectively. A skewed normal distribution fit with a 1 σ uncertainty band is shown for each scenario, and the dashed and dotted lines give maximum and 68 per cent confidence interval of these distributions, respectively. The distributions continue on the right side of each plot.

worst case scenario (shortest, weakest, latest start epoch) and the best case scenario (longest, strongest, earliest start epoch) allowed by the constraints from the data to estimate a worst and best case scenario recovery efficiency for each object.

Since the available ZTF survey plan for my simulations only spans 1004 d, I cannot set the interaction signal to start at phases after this as the interaction would never be observed. Therefore, I choose to start the interaction in my simulations no more than 750 d after the peak. This is done to ensure there is a decent chance to observe an event until after the interaction has started, while still being able to apply a good baseline correction. As the interaction is by far the dominant source of light at these epochs, changing the start date of the interaction in this way has little effect on the total brightness of the SN. However, it does affect the number of objects observed by allowing more objects to have observations at later times, when the interaction occurs. This is a redshift independent effect, but will impact the resulting recovery fraction function. To account for this, I only consider objects with observations after the start of the interaction, and remove those where the simulation limits prevent any possible late-time detection. While changing the interaction start date has increased the number of objects that satisfy this condition, there are still some objects that do not due to e.g. being in a sparsely observed field.

Not all objects in the DR2 have detections up to the time after the peak where the interaction was detected in the three final candidates. Similar to the simulation, in

order to get a proper estimate of the rate I can only consider the objects that could have been found interacting (N_{sample}), and remove those without observations this late after the peak. This gives me an effective sample size that is smaller than the full DR2, and is listed in Table 3.6.

The expected number of observed objects with late-time interaction in a sample $N_{\text{recov}}(N_{\text{sample}}, \eta(z))$ is a function of the efficiency and the intrinsic rate, which in turn is a fraction of the total SN Ia rate. If I assume the SN Ia rate from [Frohmaier et al. \(2019\)](#) as in my initial simulations and that the fraction of these showing late-time interaction, f , is redshift independent, then the only z dependency is in the efficiency of my pipeline. In a similar approach to [Prajs et al. \(2017\)](#) and [Frohmaier et al. \(2018\)](#), I run a Markov chain Monte Carlo (MCMC) simulation with 10^7 realisations for each scenario to find the fraction of interacting SNe that best explains my findings.

In each realisation of the MCMC, I draw N_{sample} objects, and assign a redshift to each object according to the distribution from [Frohmaier et al. \(2019\)](#). For each object I also draw two random numbers from a flat distribution between zero and one. The first random number is used to decide if the object was interacting, and the second to decide if any interaction would have been recovered. Interaction is true if the random number is below the chosen value for f for that realisation. Recovery is true if the second random number is below $\eta(z)$ at the z of the object (e.g. if the recovery efficiency is 0.7 at the SN redshift, a drawn number below 0.7 will result in a detection if the object was interacting). The number of recovered objects with interaction can be found by counting the objects for which both interaction and recovery is true, while the actual number of interacting objects can be found by counting the objects where interaction is true.

Figure 3.14 shows per bin the fraction of realisations that resulted in one object being recovered as a function of late-time CSM interaction fraction with the best and worst scenario parameters for the three discovered events. I approximate them by fitting a skewed normal distribution and use the fit to estimate the peak of the distribution and the 68 per cent confidence interval on either side. These values are quoted

as a fraction of the total SN Ia rate and as the late-time CSM interaction rate in the last two columns of Table 3.6.

3.4 Discussion

In this section, I first discuss the overall rate of CSM interaction signatures found in my analysis (Section 3.4.1) and some of the properties of the three SNe Ia displaying these unexplained late-time detections (Section 3.4.2).

3.4.1 Late-time interaction is rare in SNe Ia

In my study of the ~ 3500 SNe Ia in the ZTF DR2 with photometry at >100 d, I identified three objects (SN 2018grt, SN 2019ldf, and SN 2020tfc) for which late-time CSM interaction is the best explanation for their detected late-time flux excesses. However, as each of these has significantly different parameters for the interaction, they have to be treated separately when trying to estimate the rate of late-time CSM interaction in SNe Ia (Section 3.3.3). Except for the worst case scenario of SN 2018grt, the identified rate for all cases agree with one another within the uncertainty, with the fraction of SNe Ia showing late-time H α -dominated CSM interaction between $0.03^{+0.08}_{-0.02}$ and $0.23^{+0.38}_{-0.11}$ per cent. This is similar to what was found by [Sharma et al. \(2023\)](#) in their Ia-CSM sample, and agrees with the upper limit set by [Graham et al. \(2019b\)](#) with their discovery of the late-time interaction in SN 2015cp. Some objects were disregarded as I could not definitively determine that they were not due to a sibling transient. Therefore, there could be a handful of additional objects displaying strong late-time H α -dominated CSM interaction that were not included in my rate estimates but this would double the rate at most. Therefore, I estimate that the intrinsic rate of late-time H α -dominated CSM interaction in SNe Ia is < 0.5 per cent.

The identified late-time signals that are consistent with CSM interaction occurred between 1.5 to over 3.5 years after the original SN peaked. If I assume that the SN ejecta have a velocity of the order of 10^4 km s $^{-1}$, the distance at which the CSM shell

resides is of the order of 10^{17} cm. As CSM moves slowly, this means it must have been ejected from the system a long time ago. The further out the shell is from the progenitor system, the more mass is contained in even a thin shell. This is especially true when one considers that in order to get a detectable signal from the interaction, the CSM density cannot be too low. At these distances, light travel time effects also become significant, and a short interaction with a thin shell will be smeared out over a long time. Unfortunately, since I have only partial constraints on the interaction timescales and CSM mass estimation from an interaction signature is far from straightforward, I do not attempt to provide a CSM mass estimate.

An interesting aspect of the late-time detections in my three candidates is their inferred strength. While my model is likely an oversimplification by trying to explain the entire r -band signal using only a narrow $H\alpha$ line, it is clear that the signal is much stronger compared to the one found in SN 2015cp, especially when there are other band(s) at a similar magnitude. Interaction this strong is not unprecedented though, SN 2020aekp for instance, starts to plateau around 50 days after peak at an absolute magnitude $M \sim -18.5$ in all three ZTF bands ([Sharma et al., 2023](#)) and holds this plateau for several hundreds of days. Most of the known SNe Ia-CSM presented in [Sharma et al. \(2023\)](#) have detections in multiple bands, and the spectra presented show more than just an $H\alpha$ line coming from the CSM interaction. CSM around a SN Ia also does not have to be spherically symmetric, especially in a scenario where material has been stripped and partially lost from the donor star in the progenitor system. [Smith et al. \(2015b\)](#) show for SNe IIn that if the CSM mostly resides in a disk, only the ejecta travelling in the direction of the disk will be slowed down and interact while ejecta at higher inclinations continues to expand normally.

The colour curves for the late-time detections in my three objects (Fig. 3.13), show that $g-r \sim 1.7$ mag for SN 2020tfc, with limits of $g-r > 0.5$ and 1.5 mag for SN 2018grt and SN 19ldf, respectively. For the two objects with i -band observations, $r-i < 0.5$ mag. The SN Ia-CSM sample of [Sharma et al. \(2023\)](#) had late-time (>300 d) $g-r$ colours of 0 – 0.5 mag, which are similar to SN 2018grt but bluer than SN 2019ldf and

SN 2020tfc. [Kool et al. \(2023\)](#) find $g - r \sim -1$ mag and $r - i \sim 0.5$ mag at late times for the He-interacting Ia-CSM SN 2020eyj. When taking into account the host galaxy extinction that they identify, it becomes even bluer and is much bluer than my three objects.

3.4.2 Properties of SNe Ia with late-time interaction

The three SNe Ia with late-time flux excesses that cannot be explained by other scenarios have SALT2 light curve fitter x_1 and c values that are generally typical of normal SNe Ia (Rigault et al. in prep.). However, the c value of SN 2018grt of 0.61 ± 0.03 is at the high end and would be excluded from cosmological analyses. I also identified significantly more host extinction for this object than for the other two based on their luminosities at the peak.

All three candidates are found at small projected distances from their host nuclei. While the small sample size might be used to explain part of this observation, the mean projected distance of all objects in the ZTF DR2 is 6.3 kpc (Rigault et al. in prep.). The chance for my three objects to be at most 0.8 kpc from the host is < 1 per cent, suggesting that objects with late-time interaction have a preference for small host separations, the detections are caused by nuclear variability, or they are caused by bad host subtraction. The location of the late-time signal is too close to the host nucleus to distinguish which location the late-time signal is more consistent with by using SNAP. The host galaxy colours are inconsistent with being AGN and the properties of the late-time detections cannot be easily explained by known nuclear transient classes such as TDEs. It is possible that by going to deeper limiting magnitudes with my light curve binning that I have identified previously unstudied nuclear variability but this cannot be confirmed. Imperfect template subtraction can occur to galaxy centres, resulting in a dipole artefact. However, these are easily recognisable with SNAP, and this possibility was ruled out for my three candidates. Therefore, I conclude that that a likely interpretation is that there may be something intrinsic to SNe Ia exploding in these environments that produces late-time CSM interaction but further samples are

required to confirm.

The morphologies of the host galaxies of the candidate events are broadly elliptical or spheroidal in nature with no signs of spiral arms. The galaxies have stellar masses of 4×10^9 , 6×10^{10} , and $2 \times 10^{10} M_{\odot}$ for SN 2018grt, SN 2019ldf, and SN 2020tfc, respectively. These host masses are all within the bulk of the masses of the ZTF DR2 SN Ia sample (Rigault et al. in prep.). The hosts of the known H-rich Ia-CSM sample have stellar masses of $\sim 3 \times 10^8$ to $3 \times 10^{10} M_{\odot}$, consistent with my objects (Sharma et al., 2023). SN 2020eyj, the He-interacting and radio detected SN Ia-CSM (Kool et al., 2023) also had a very small offset from its host of $0.57 \pm 0.02''$ (0.36 ± 0.01 kpc). Its host only has a WISE $W3$ upper limit so it cannot be excluded from having an AGN present. It is a compact star forming galaxy with a mass of $\sim 6 \times 10^7 M_{\odot}$, which is lower than the typical Ia-CSM range (Sharma et al., 2023).

The hosts of the three candidate events all have WISE $W1 - W2 \approx 0$ mag. SN 2020tfc has $W2 - W3$ of ~ 0.8 mag, while the other two have only limits with $W2 - W3 > 1.2$ mag. Based on Fig. 2 of Irani et al. (2022), this places them in the overlap region between elliptical and spiral host properties from the galaxy sample of Lintott et al. (2011). The vast majority of Ia-CSM sample of Sharma et al. (2023) has $W2 - W3$ colours of > 1 mag, again broadly consistent with my sample. However, the morphologies of my candidate events do not show evidence for spiral arms and their overlap between ellipticals and spirals in the $W2 - W3$ parameter space suggest they may come from different, older stellar populations than the known Ia-CSM events (Kool et al., 2023; Sharma et al., 2023). However, to prove that these are different populations requires a larger sample.

3.4.3 Limitations of the analysis

Since there is no good model of a Type Ia SN interacting with CSM at late times that could be used for my SIMSURVEY simulations, I had to make my own based on several assumptions. My main assumptions were that the SN Ia looks normal until the moment the interaction starts, and I assumed that this interaction was with hydrogen-

rich material showing itself primarily as an H α emission line. This is motivated by the fact that H α is found in most SNe Ia-CSM and the late-time interaction in SN 2015cp was confirmed through the observation of an H α emission line. However, [Graham et al. \(2019b\)](#) also found other emission lines that are associated with the SN, such as the Ca II triplet near 8500 Å and a tentative detection of Mg I λ 5175, suggesting that my model is too simplistic. Similarly, for SN 2020tfc, I identified late-time detections in the *gri*-bands, which cannot be explained by H α emission alone.

This method of binning the late-time light curves allows to push the detection limit down to a limiting magnitude $m = 21.44$ mag. Since the references used in ZTF have a mean limiting magnitude of $\bar{m}_{\text{lim}} \sim 21.8$ mag, this becomes the leading uncertainty preventing my binning technique to go deeper. I have shown through my simulations that deeper references will allow for the binning technique to go deeper and recover fainter interaction signatures in a larger redshift volume. I have also used SMP to generate light curves that did not rely on forced photometry to test for issues coming from the photometry measurement. In most cases the late-time detections were recovered with both methods, showing their robustness. However, the SMP has been found to have issues with identifying a baseline flux when the number of images used in scene model template creation is small. This highlights the requirement for a long off time to model the underlying galaxy light sufficiently.

The pipeline focusses more on the historical light curve of the SNe than their current state. Since I require two adjacent bins to be detections in order to avoid false positives and the smallest bins I use are 25 d, the interaction needs to be active for over a month before it is picked up. Only after this, can it be followed up with spectroscopy if identified fast enough and the interaction signature is still occurring. Unfortunately, in the cases of my three candidates this could not be done due to a combination of recovering the interaction late, the objects being blocked by the Sun for a section of the year, and not having a suitable reference spectrum of the host galaxy to subtract and isolate the interaction spectrum. Adapting the pipeline to run in real-time would help with shortening the timescale to detection but if the host galaxy contribution is

strong, then an archival reference spectrum is required.

3.4.4 By-product pipeline detections

The conservative, catch-all approach outlined in my work poses the challenge of identifying exactly why each object is flagged by the pipeline. My approach allows for different kinds of objects that become interesting at late times to be caught. I recovered nearly all known Ia-CSM SNe through their non-normal SN Ia tails, as well as a number of known and unknown siblings, along with evidence of a change in the declining tail slope of close-by, normal Type Ia SNe around 200 days after the peak. In my sample, four per cent of the objects needed to be visually inspected, upon which the cause of the (false) positive became clear quickly for most objects. Some of the checks, such as using the WISE colours to identify an AGN host close to the SN location, have been automated, reducing the workload in future attempts to use this method for searching for late-time signals, especially when using large datasets such as the Vera C. Rubin Observatory’s Legacy Survey of Space and Time (LSST; [Ivezić et al., 2019](#)).

The pipeline, as presented in this paper, is specifically tailored for finding SNe Ia that deviate from normal behaviour at >100 d after the peak. However, the method of binning late-time observations can be used for any type of transient, but the checks to ensure that the resulting detections are not due to expected behaviour are SN Ia specific. When other types of transients (e.g. SN Ib, Ic, IIP) are used as input, the result will likely vary. For instance, a long lasting plateau in an SN IIP will be unexpected by the pipeline as it does not follow the decline tail of a normal SN Ia. However, modifying the pipeline to work for different kinds of transients mostly requires revision of these checks.

3.5 Conclusions

I have presented a search of the ZTF DR2 SN Ia light curve sample for signatures of late-time CSM interaction. This is the first systematic search for signatures of late-time

interaction in SNe Ia in a large optical survey. I made a custom pipeline to calibrate and bin the light curve data at more than 100 d after the peak, using bins with sizes between 25 and 100 d. My analysis was based on searching for H α emission (as was seen in SN 2015cp and Ia-CSM) in the *r*-band at lower redshift and *i*-band above a redshift of $z = 0.07$. I performed simulations with SIMSURVEY to determine the efficiency of my search, as well as the intrinsic rate of potential H α -dominated CSM interaction in the sample. My main conclusions are:

1. My pipeline returned 134 SNe that were potentially interesting based on their late-time light curves. Visual inspection of these objects was performed using my visualisation programme, SNAP, to inspect the difference images, removing 101 objects as false positives.
2. Of the remaining 33 objects, I identified 13 out of the 14 known Ia-CSM objects in the DR2, five siblings close to the position of the original SN Ia, four very nearby events whose late-time light curves were not captured by my simple radioactive tail model and one Iax with a late-time excess in all three bands, consistent with the presence of a bound remnant.
3. Out of my final shortlist of ten candidate events, I identified three SNe Ia (SN 2018grt, SN 2019ldf, and SN 2020tfc) that displayed late-time detections beginning 550 - 1350 d after peak and lasting at least 100 - 250 d, which could not be explained by data issues, AGN activity, or other transient events exploding at a similar location.
4. For SN 2018grt, these late-time detections were only in the *r*-band (no coeval *i*-band data was available). For SN 2019ldf, detections were made in the *ri*-bands and for SN 2020tfc in all three bands suggesting potential contributions with Ca II NIR emission or other Mg I as was identified in SN 2015cp ([Graham et al., 2019b](#)).
5. The *r*-band magnitudes of the late-time interaction are -16.5 , -16.4 , and -16.8

mag for SN 2018grt, SN 2019ldf, and SN 2020tfc, respectively. At their respective redshifts, this corresponds to H α interaction strengths of 60 – 150 times that of SN 2015cp (depending on the extinction correction used). The strong nature of this signal could suggest I might only have found the high end of the late-time interaction strength distribution.

6. Using SIMSURVEY simulations of the ZTF survey, I estimated the intrinsic rate of strong H α -dominated late-time (> 100 days after the SN peak) interaction to be occurring in < 0.5 per cent of SNe Ia. This translates to absolute rates of 8_{-4}^{+20} to 54_{-26}^{+91} Gpc $^{-3}$ yr $^{-1}$, assuming a constant SN Ia rate of 2.4×10^{-5} Mpc $^{-3}$ yr $^{-1}$ for $z \leq 0.1$.

The rarity of late-time interaction (occurring in < 0.5 per cent of SNe Ia) highlights the importance of a large dataset of objects that have been observed for multiple years. The late-time detections occurred at different epochs for each object (from 550 – 1350 d post peak), showing that the phase at which SNe Ia will start to show signs of CSM interaction is highly variable. Therefore, the only viable strategy is to keep observing SNe even after they have faded beyond the detection limit and binning the late-time light curves. The interaction strength that the binning technique is sensitive to is heavily dependent on both the science and reference image depth. Future improvements to the analysis would include the use of deeper reference images to detect fainter signatures of late-time interaction, as well as running the pipeline in real time so that additional photometry and spectroscopy can be obtained to further characterise the late-time excesses. The deeper magnitude limits of LSST would be ideal for this study but cannot be immediately performed when the survey starts because of the requirements of deep reference images, as well as the need to wait up to more than three years after the SN Ia peak for the interaction to occur.

3.6 Tables

Table 3.7: Spectra used to make the SN 2011fe model. All spectra were taken from WISeREP (Yaron & Gal-Yam, 2012).

MJD	Phase (d)	Telescope	Instrument	Wavelength coverage (Å)	Reference
55798.0	-16.0	Lijiang-2.4m	YFOSC	3461 – 8956	Zhang et al. (2016)
55798.2	-15.8	Lick-3m	KAST	3416 – 10278	Nugent et al. (2011)
55799.0	-15.0	Lijiang-2.4m	YFOSC	3502 – 8958	Zhang et al. (2016)
55799.3	-14.7	UH88	SNIFS	3296 – 9693	Pereira et al. (2013)
55800.2	-13.8	UH88	SNIFS	3296 – 9693	Pereira et al. (2013)
55801.2	-12.8	UH88	SNIFS	3296 – 9693	Pereira et al. (2013)
55802.3	-11.7	UH88	SNIFS	3296 – 9693	Pereira et al. (2013)
55803.2	-10.8	UH88	SNIFS	3296 – 9693	Pereira et al. (2013)
55804.2	-9.8	UH88	SNIFS	3296 – 9693	Pereira et al. (2013)
55805.2	-8.8	UH88	SNIFS	3296 – 9693	Pereira et al. (2013)
55806.2	-7.8	UH88	SNIFS	3296 – 9693	Pereira et al. (2013)
55807.3	-6.7	UH88	SNIFS	3296 – 9693	Pereira et al. (2013)
55808.2	-5.8	UH88	SNIFS	3296 – 9693	Pereira et al. (2013)
55809.2	-4.8	UH88	SNIFS	3296 – 9693	Pereira et al. (2013)
55811.4	-2.6	HST	STIS	1779 – 24965	Mazzali et al. (2014)
55812.0	-2.0	Gemini-N	GMOS	3497 – 9648	Parrent et al. (2012)
55813.2	-0.8	UH88	SNIFS	3296 – 9693	Pereira et al. (2013)
55814.2	0.2	UH88	SNIFS	3296 – 9693	Pereira et al. (2013)
55815.2	1.2	UH88	SNIFS	3296 – 9693	Pereira et al. (2013)
55816.2	2.2	UH88	SNIFS	3296 – 9693	Pereira et al. (2013)
55817.2	3.2	UH88	SNIFS	3296 – 9693	Pereira et al. (2013)
55817.7	3.7	HST	STIS	1265 – 24965	Mazzali et al. (2014)
55818.2	4.2	UH88	SNIFS	3296 – 9693	Pereira et al. (2013)
55821.2	7.2	UH88	SNIFS	3296 – 9693	Pereira et al. (2013)
55823.2	9.2	UH88	SNIFS	3296 – 9693	Pereira et al. (2013)
55826.2	12.2	UH88	SNIFS	3296 – 9693	Pereira et al. (2013)
55828.2	14.2	UH88	SNIFS	3296 – 9693	Pereira et al. (2013)
55829.0	15.0	Gemini-N	GMOS	3497 – 9643	Parrent et al. (2012)
55830.2	16.2	Keck1	LRIS	3227 – 10242	Stahl et al. (2020)
55831.2	17.2	UH88	SNIFS	3296 – 9693	Pereira et al. (2013)
55832.0	18.0	Lijiang-2.4m	YFOSC	3577 – 8957	Zhang et al. (2016)
55833.2	19.2	UH88	SNIFS	3296 – 9693	Pereira et al. (2013)
55835.3	21.3	HST	STIS	1731 – 10221	Mazzali et al. (2014)
55836.2	22.2	UH88	SNIFS	3296 – 9693	Pereira et al. (2013)
55838.2	24.2	UH88	SNIFS	3296 – 9693	Pereira et al. (2013)
55841.3	27.3	HST	STIS	1738 – 10221	Mazzali et al. (2014)
55855.2	41.2	HST	STIS	1738 – 10216	Mazzali et al. (2014)
55888.6	74.7	UH88	SNIFS	3296 – 9693	Pereira et al. (2013)
55891.7	77.7	UH88	SNIFS	3296 – 9693	Pereira et al. (2013)
55893.6	79.7	UH88	SNIFS	3296 – 9693	Pereira et al. (2013)
55896.6	82.6	UH88	SNIFS	3296 – 9693	Pereira et al. (2013)
55897.7	83.7	Keck1	LRIS	3164 – 10126	Stahl et al. (2020)
55901.6	87.6	UH88	SNIFS	3296 – 9693	Pereira et al. (2013)
55903.6	89.6	UH88	SNIFS	3296 – 9693	Pereira et al. (2013)
55911.0	97.0	XLT	BFOSC	3296 – 9693	Zhang et al. (2016)
55911.6	97.6	UH88	SNIFS	3296 – 9693	Pereira et al. (2013)
55913.5	99.5	Lick-3m	KAST	3427 – 10332	Stahl et al. (2020)
55914.0	100.0	WHT-4.2m	ISIS	3499 – 9491	Friesen et al. (2017)
55916.0	102.0	WHT-4.2m	ISIS	3498 – 9491	Law et al. (2009); Rau et al. (2009)
55917.0	103.0	WHT-4.2m	ISIS	3499 – 9492	Law et al. (2009); Rau et al. (2009)
55926.0	112.0	Lijiang-2.4m	YFOSC	3366 – 9069	Zhang et al. (2016)
55929.5	115.5	Lick-3m	KAST	3426 – 10170	Stahl et al. (2020)
55944.5	130.5	Lick-3m	KAST	3453 – 10088	Stahl et al. (2020)
55959.0	145.0	Lick-3m	KAST	3497 – 10000	Law et al. (2009); Rau et al. (2009)
55980.4	166.4	Lick-3m	KAST	3441 – 10250	Stahl et al. (2020)

MJD	Phase (d)	Telescope	Instrument	Wavelength coverage (Å)	Reference
55988.0	174.0	WHT-4.2m	ISIS	3495 – 9982	Mazzali et al. (2015)
56019.4	205.4	Lick-3m	KAST	3438 – 10324	Mazzali et al. (2015)
56040.4	226.4	Lick-3m	KAST	3437 – 10178	Mazzali et al. (2015)
56047.0	233.0	Lijiang-2.4m	YFOSC	3392 – 9053	Zhang et al. (2016)
56073.0	259.0	WHT-4.2m	ISIS	3495 – 9483	Mazzali et al. (2015)
56103.0	289.0	WHT-4.2m	ISIS	3423 – 10268	Mazzali et al. (2015)
56127.0	313.0	P200	DBSP	3197 – 10991	Law et al. (2009); Rau et al. (2009)
56162.2	348.2	Lick-3m	KAST	3487 – 10240	Mazzali et al. (2015)
56194.2	380.2	Keck1	LRIS	3232 – 10268	Stahl et al. (2020)
56277.0	463.0	Lijiang-2.4m	YFOSC	3379 – 9337	Zhang et al. (2016)
56778.5	964.5	Keck1	LRIS	3074 – 10320	Graham et al. (2015)
56831.2	1017.2	LBT	MODS1	3098 – 10487	Taubenberger et al. (2015)

3.7 Inputs to SIMSURVEY simulations

The specific inputs to SIMSURVEY used in Section 3.2.4.2 to determine the detection efficiencies for SN 2015cp-like interaction are listed here.

- Model: SN 2011fe + H α line (Section 3.2.4.1).
- Sky distribution: RA $\in [0^\circ, 360^\circ]$, Dec. $\geq -30^\circ$ (The area covered by ZTF, Bellm et al. 2019a).
- Volumetric rate: The SN Ia rate is $2.4 \times 10^{-5} \text{ Mpc}^{-3} \text{ yr}^{-1}$ for $z \leq 0.1$ (Frohmaier et al., 2019). SIMSURVEY uses this to calculate the amount of SNe to generate at a given redshift interval.
- SN peak time distribution: $58\,195 \leq \text{modified Julian date (MJD)} \leq 58\,487$ (between 18 March 2018 and 4 January 2019).
- Galactic extinction: dust maps from Schlegel et al. (1998).
- Host galaxy extinction: Cardelli et al. (1989) extinction law, with $E(B - V)$ drawn from an exponential distribution with exponent $\lambda = 0.11$ (Stanishev et al., 2018), the same way as host extinction was added in the original SIMSURVEY paper (Feindt et al., 2019b).
- Telescope specifications: ZTF P48 camera, 4×4 grid of CCDs with four readout channels each, resulting in 64 separate output channels (Dekany et al., 2020).
- Survey plan: ZTF observation logs between $58\,197 \leq \text{MJD} \leq 59\,211$ (between 20 March 2018 and 28 December 2020), ensuring all simulated SNe are followed for a minimum of about 2 years after the peak.

3.8 Late-time spectrum of SN 2020alm

After confirming the late-time detections in SN 2020alm to still be ongoing, a spectrum was obtained using OSIRIS+ on the GTC on 26 July 2023, 1277 days after the

Table 3.8: Redshift values where 50 per cent of the simulated SNe were found to have CSM interaction. Strength is the strength of the H α line compared to the strength detected in SN 2015cp. Start shows how many days after the peak the interaction begins, and duration is in days as well. I fitted sigmoid functions to the results of each simulation in order to find the redshift where 50 per cent of the interactions were recovered, assuming the reference images were of the same depth as the ones used in ZTF or 0.5 or 1 mag deeper. These values are shown in $z_{50} \pm \sigma_{z_{50}}$, and χ^2_{red} shows the quality of the fit.

strength	start	duration	ZTF references			0.5 mag deeper			1 mag deeper		
			z_{50}	$\sigma_{z_{50}}$	χ^2_{red}	z_{50}	$\sigma_{z_{50}}$	χ^2_{red}	z_{50}	$\sigma_{z_{50}}$	χ^2_{red}
0.0	–	–	0.0038	0.0009	0.72	0.0042	0.0019	1.83	0.0046	0.0032	3.47
0.1	100	100	0.0041	0.0008	0.83	0.0049	0.0011	1.82	0.0049	0.0033	3.41
0.1	100	300	0.0050	0.0007	0.79	0.0055	0.0014	1.79	0.0059	0.0025	3.42
0.1	100	500	0.0053	0.0006	0.77	0.0062	0.0011	1.76	0.0068	0.0018	3.44
0.1	200	100	0.0045	0.0007	0.78	0.0050	0.0016	1.80	0.0054	0.0028	3.38
0.1	200	300	0.0053	0.0006	0.78	0.0058	0.0014	1.79	0.0063	0.0022	3.44
0.1	200	500	0.0056	0.0006	0.77	0.0066	0.0010	1.79	0.0073	0.0016	3.47
0.1	300	100	0.0050	0.0006	0.80	0.0056	0.0012	1.80	0.0059	0.0023	3.43
0.1	300	300	0.0052	0.0006	0.80	0.0061	0.0044	1.78	0.0067	0.0017	3.46
0.1	300	500	0.0053	0.0005	0.82	0.0060	0.0010	2.03	0.0069	0.0016	3.53
0.1	500	100	0.0045	0.0007	0.82	0.0048	0.0014	2.08	0.0054	0.0021	3.52
0.1	500	300	0.0050	0.0005	0.83	0.0056	0.0010	2.09	0.0062	0.0017	3.53
0.1	500	500	0.0050	0.0005	0.82	0.0057	0.0009	2.09	0.0063	0.0017	3.52
1.0	100	100	0.0041	0.0007	0.86	0.0045	0.0013	2.10	0.0046	0.0027	3.58
1.0	100	300	0.0091	0.0005	0.85	0.0096	0.0012	1.98	0.0108	0.0017	3.40
1.0	100	500	0.0111	0.0004	0.84	0.0129	0.0008	2.08	0.0139	0.0013	3.50
1.0	200	100	0.0067	0.0007	0.80	0.0077	0.0012	2.05	0.0083	0.0021	3.51
1.0	200	300	0.0104	0.0005	0.93	0.0122	0.0008	2.06	0.0130	0.0014	3.31
1.0	200	500	0.0116	0.0004	0.84	0.0129	0.0008	2.11	0.0140	0.0018	3.63
1.0	300	100	0.0086	0.0004	0.78	0.0094	0.0008	1.95	0.0100	0.0013	3.62
1.0	300	300	0.0105	0.0004	0.75	0.0118	0.0007	2.02	0.0128	0.0015	3.61
1.0	300	500	0.0109	0.0004	0.78	0.0125	0.0008	2.11	0.0139	0.0013	3.76
1.0	500	100	0.0081	0.0003	0.83	0.0090	0.0008	1.94	0.0094	0.0016	3.69
1.0	500	300	0.0104	0.0003	0.78	0.0121	0.0007	2.10	0.0133	0.0012	3.79
1.0	500	500	0.0105	0.0003	0.80	0.0122	0.0007	2.11	0.0135	0.0012	3.80
10.0	100	100	0.0091	0.0014	0.93	0.0097	0.0028	2.13	0.0087	0.0058	3.45
10.0	100	300	0.0259	0.0007	1.36	0.0299	0.0009	1.79	0.0328	0.0012	1.83
10.0	100	500	0.0297	0.0005	1.21	0.0347	0.0007	1.83	0.0383	0.0010	1.84
10.0	200	100	0.0204	0.0009	1.69	0.0223	0.0012	2.40	0.0217	0.0019	2.54
10.0	200	300	0.0314	0.0004	1.45	0.0351	0.0007	1.98	0.0377	0.0010	2.40
10.0	200	500	0.0326	0.0005	1.50	0.0374	0.0007	2.05	0.0415	0.0009	1.95
10.0	300	100	0.0221	0.0023	1.21	0.0233	0.0011	2.01	0.0231	0.0019	2.71
10.0	300	300	0.0311	0.0004	1.30	0.0350	0.0007	1.90	0.0375	0.0010	2.27
10.0	300	500	0.0328	0.0004	1.42	0.0381	0.0007	2.22	0.0423	0.0009	2.21
10.0	500	100	0.0199	0.0011	1.80	0.0224	0.0014	2.47	0.0226	0.0019	3.04
10.0	500	300	0.0323	0.0004	1.23	0.0371	0.0007	2.12	0.0406	0.0009	2.19
10.0	500	500	0.0323	0.0004	1.22	0.0373	0.0007	2.12	0.0407	0.0009	2.12

estimated peak date of the SN. As the observed spectrum is heavily dominated by the host galaxy, I subtracted a host galaxy spectrum taken by SDSS in 2003 to remove the host contamination. This was done after re-sampling the host spectrum to have the same wavelength spacing as the new spectrum. This left only the spectrum causing the late-time photometry detections, and is shown in Fig. 3.15. The subtraction was confirmed to be successful by checking that the Mg I $\lambda 5175$ and Na ID absorption lines were reduced to the noise level, as these lines are not expected to be due to the late-time signal but purely from the host galaxy. Some of the host galaxy emission lines were not completely subtracted during this process, most noticeably [N II] $\lambda 6583$ and [S II] $\lambda\lambda 6716, 6730$, but the resolution is inadequate to draw any conclusions from this.

The only explanation for the late-time detections that uses a second transient at the same location is a TDE. Hammerstein et al. (2023) shows that the intrinsic spectrum of a TDE is flat in this wavelength range, with sometimes some narrow emission lines. Therefore, I model a TDE spectrum as a line of constant flux density and add Milky Way extinction (using the SFD89 dust maps in the direction of the object; Schlegel et al., 1998) and variable host extinction in an attempt to obtain the general shape of the observed spectrum. I find that $0.6 \leq E(B - V)_{\text{host}} \leq 1$ mag is adequate to reproduce the general spectral shape and suggests that a TDE with approximately constant colour and moderate host extinction can explain the observed spectral excess for this event.

3.9 Binned SMP light curves of the final candidates

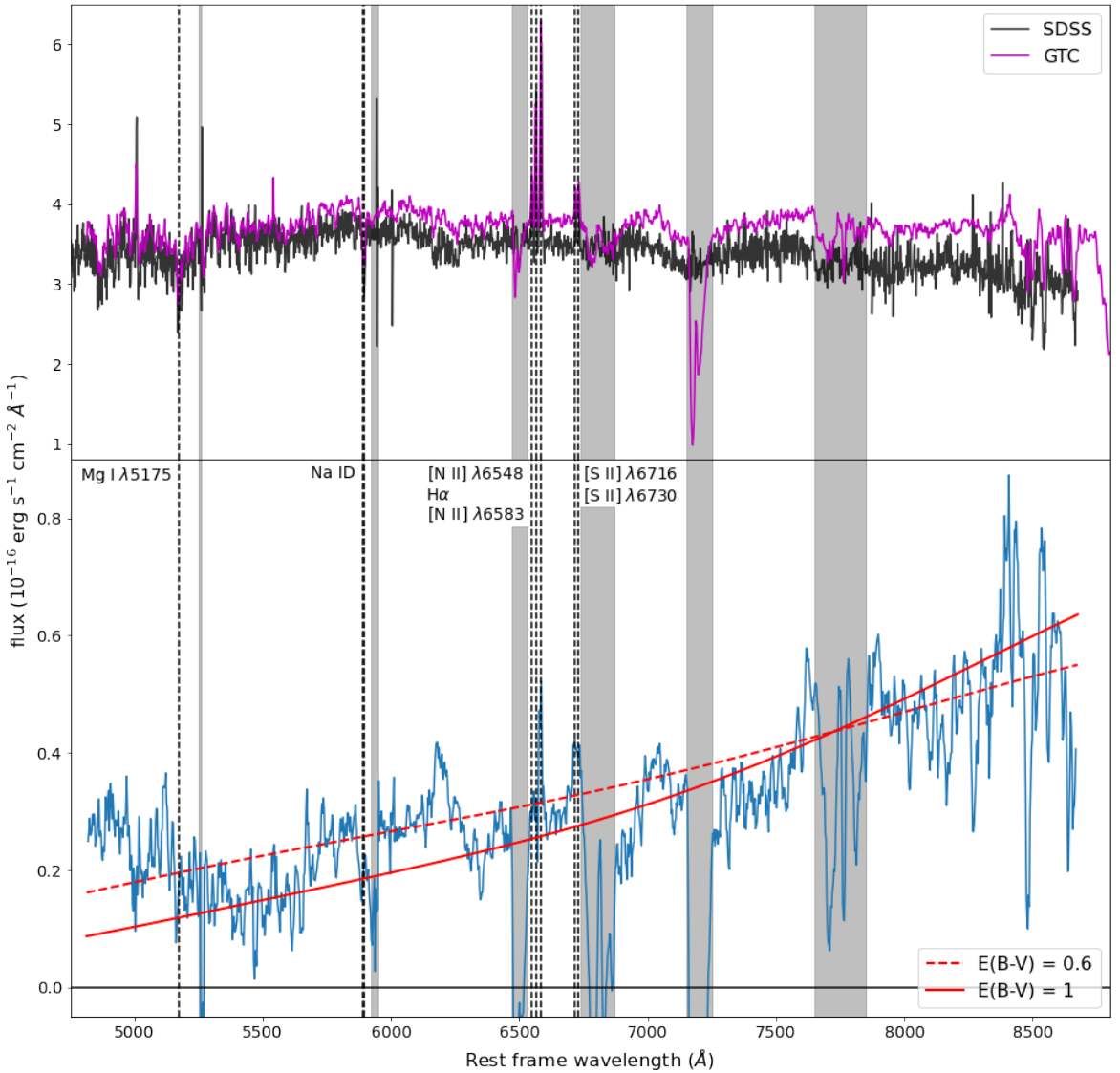


Figure 3.15: Spectrum of the late-time signal in SN 2020alm in its rest frame. The top panel shows the late-time spectrum obtained on 26 July 2023 using OSIRIS+ on the GTC, and the SDSS spectrum obtained in 2003. The bottom panel shows the late-time excess, obtained by subtracting the SDSS host galaxy spectrum from the observed late-time spectrum. A smoothed spectrum is shown in blue. The smoothing was done using a rolling kernel of size 5 to average over the values. The red lines are a simple TDE model with Milky Way and some amount of host galaxy extinction applied (the amount is shown in the legend), in order to get the approximate shape of the observed spectrum. Narrow emission and absorption lines that were notable in the unsubtracted spectrum are marked with dashed lines. The grey regions are affected by sky lines, and should be ignored. The late-time spectrum of SN 2020alm is available in electronic form at the CDS via anonymous ftp to cdsarc.u-strasbg.fr (130.79.128.5), via <http://cdsweb.u-strasbg.fr/cgi-bin/qcat?J/A+A/> or upon request to the author.

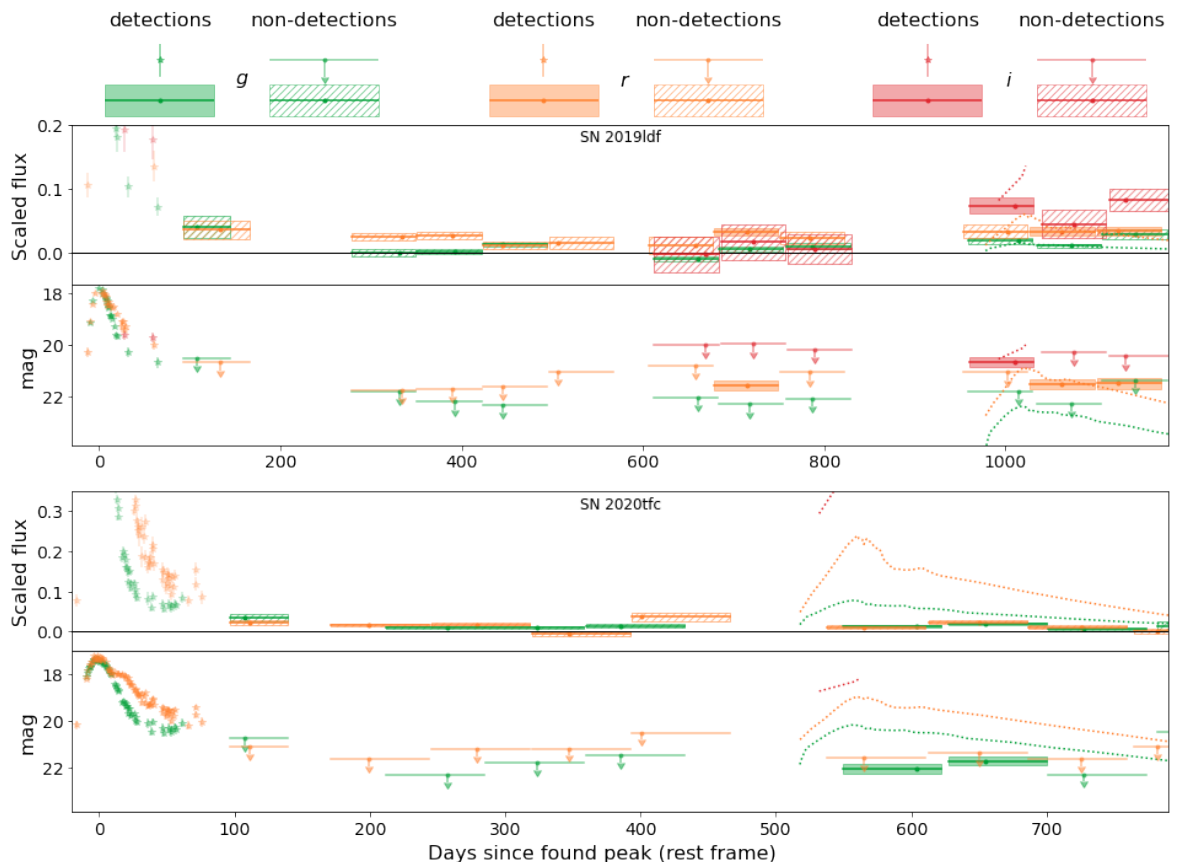


Figure 3.16: Binned SMP light curves of the three candidate objects. As no bins $\geq 5\sigma$ are recovered in SN 2018grt, it is not shown here. Both SN 2019ldf and SN 2020tfc do however still have robust detections in some bands. The best fitting alternate transients, shown in dotted lines, are the same as in Fig. 3.12. The *i*-band of SN 2020tfc is not shown as the background was not subtracted completely, resulting in a significant flux offset.

ZTF-observed late-time signals of pre-ZTF transients

This is Paper II, but needs to be properly adapted. All commented out sections are still in the overleaf version if needed. Copy back in final part of intro, make a short intro, refer back to previous chapters, put everything into I form. Copied starting from Data until the end of conclusions and appended the appendix straight afterwards. To-do list: Check for broken references, check for double refs, reformat pages, add chapter introduction, expand SNAP section, make sure all the *gri* things are consistent

4.1 Data

Our first aim is to compile a list of all transients discovered in the decade before ZTF started. To build our sample, we started with all transients in the Open Supernova Catalog (OSC¹, Guillochon et al. 2017) that were discovered between 1 January 2008 up to 1 January 2018, giving us 22 790 objects. We end our sample a few months before the start of the full ZTF survey in March 2018 to remove most pre-ZTF transients that were still visible by the start of ZTF. For each object we require a name, sky position, redshift, and classification of its type. We require the redshift to make an informed estimation of the absolute luminosity of any potentially detected late-time signal. For the vast majority of transients, a classification means a spectrum was obtained that enabled typing but the size of the sample precludes checking of each individual classification. However, further investigation of identified interesting events is performed where required. We also include objects classified as a ‘SN candidate’ as they are likely SNe but were never spectroscopically classified. These requirements cut our sample down to 8 865 objects. By querying WISEREP² (Yaron & Gal-Yam, 2012) for objects reported in the same date range, we attempted to recover objects that were

¹<https://github.com/astrocatalogs/supernovae>

²<https://www.wiserep.org>

incomplete or absent from the OSC. Out of the 12 955 OSC objects that did not have all the required information and no WISEREP match, 1 137 had no sky position while the other 11 818 had a sky position but no reported redshift and/or classification.

From the combined sample, we removed objects at $\text{Dec} \leq -32$ deg as ZTF is unable to observe below $\text{Dec} \approx -30$ deg. After these updates (including WISEREP and with Declination cut) our sample increased to 8 914 objects. The declination cut is liberal to ensure all object locations that could have been observed with ZTF remain in our sample. Objects outside the ZTF footprint but still in our sample are cut automatically when obtaining the ZTF light curves. We do not make a cut on proximity to the host nucleus as we want to be as inclusive as possible. Instead we accept the possible contamination by nuclear activity which, as will be shown later, is in most cases easily identifiable.

While cross-matching between OSC and WISEREP to remove duplicate entries, we noted several objects with different names and discovery dates but located very close on the sky. While uncommon, it is not impossible for multiple SNe to occur at the same sky position in short succession. Terwel et al. (2024) found several such sibling transients at very small separations where both SNe were detected by ZTF. Since we just look at the late-time light curve at the sky position of each pre-ZTF transient, sibling transients like these are investigated together as they have the sky position.

Our late-time light curves at the position of each transient in the list were constructed, using the method detailed in Section 4.2, between 9 December 2023 and 24 January 2024 using all available ZTF data at the time. This results in an effective range of over 5.5 years of ZTF observations for each object in our sample. For 207 sky positions that lay close to the edge of the ZTF survey, no ZTF observations were obtained and these were removed from our sample, leaving us with 8 707 transients in our final sample. The ZTF light curves at these sky positions are generated using FPBOT¹ (Reusch, 2023)

We group the transients in our sample into one of nine classes based on the most

¹<https://github.com/simeonreusch/fpbots>

precise common denominator of the reported classifications. For example, an object that was reported as both a SN Ia and SN Ib is grouped as a ‘SN I’, and an object that was reported as some type of SN I and SN II is grouped as a ‘SN’. SLSNe are handled the same and grouped with normal SNe into SN I or SN II, though we can recover their SLSN classification if the object proves interesting later. Objects whose classification included the interacting classes SNe Ibn and SNe IIn are kept separately as we expect these may have a higher chance of having a late-time signature that can be picked up by ZTF. Figure 4.1 shows the nine classes in our sample (‘Ia’, ‘II’, ‘Ib/c’, ‘IIn’, ‘Ibn’, ‘I’, ‘SN’, ‘SN candidate’, and ‘not SN’) and their relative sizes.

For completeness we include a ‘non SN’ class that consists of other type of transients. This class consists of 60 variable stars which includes cataclysmic variables (CVs), luminous blue variables (LBVs), and novae, 36 nuclear transients (including TDEs and AGN), 73 other transients (including gap transients, impostor-SNe, kilonovae), and 140 Long Gamma Ray Bursts (LGRBs). Figure 4.2 shows the amount of objects in each class as a function of redshift. Our sample is biased towards lower redshifts as it is magnitude limited. We also have more objects that have been discovered in years where large surveys such as PTF, iPTF and ATLAS were active.

4.2 Analysis

We use an adapted version of the pipeline introduced in [Terwel et al. \(2024\)](#) to test for late-time flux excesses in our sample of pre-ZTF transients. In brief, the pipeline first applies a baseline correction to ensure that the light curve has zero flux when no signal is expected (e.g. [Yao et al., 2019](#); [Miller et al., 2020](#)). It then bins the post-SN observations together in bins of 25, 50, 75, or 100 days to recover signals that are below the noise level of individual observations. To test if bin placement has an effect on the result, the binning is performed multiple times with shifted bin phase locations. Only signals that are sufficiently insensitive to bin placement are considered real. Binning observations increases the depth at which signals can be recovered at the cost of time

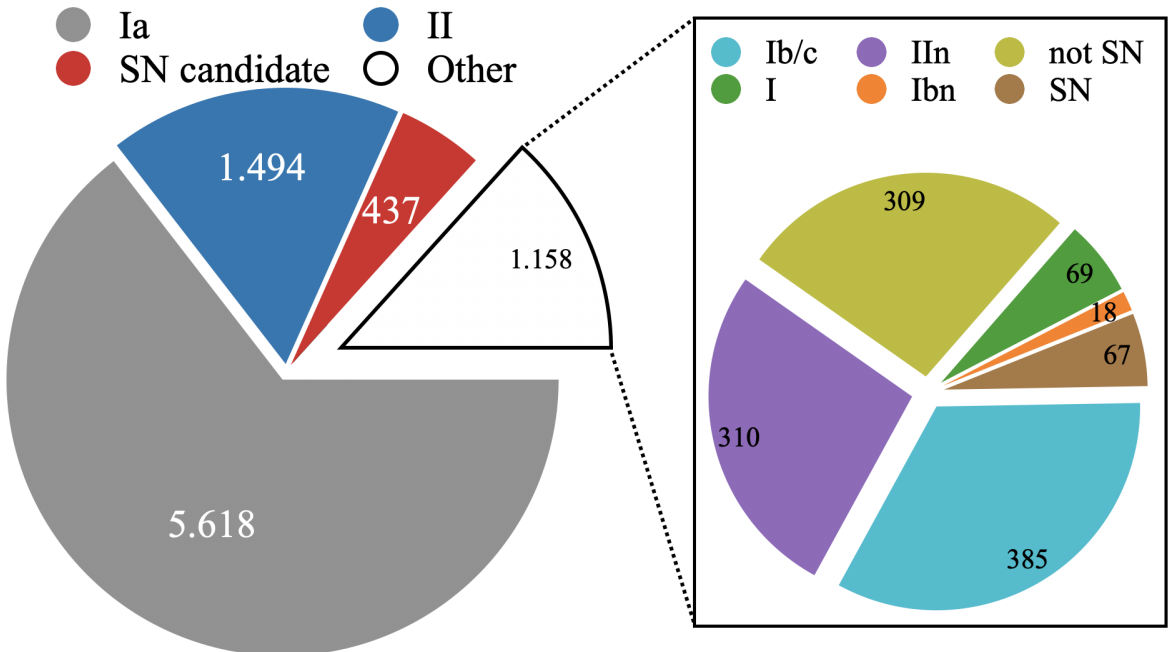


Figure 4.1: The final sample split into nine classes. As there is a big difference in class sizes, the smaller groups have been put together in the left chart as ‘other’ and are split up in the right chart.

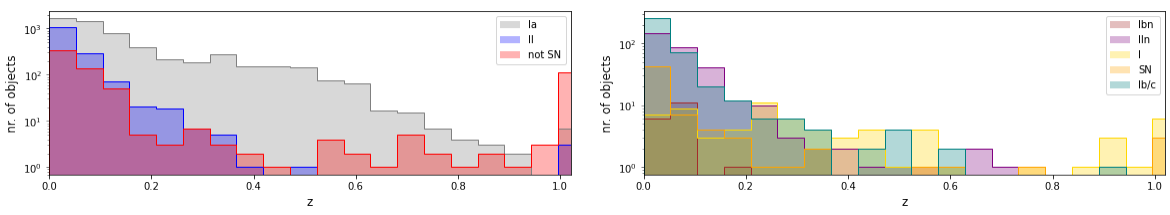


Figure 4.2: Sample size as a function of redshift for each class of objects. All objects with $z > 1$ are put together in the bin starting at $z = 1$. The histograms are split into two plots for better readability. In all classes of objects our sample is biased towards lower z .

sensitivity. As our smallest bins are 25 days in the observer frame, this means that we cannot detect details at similar or smaller time scales, such as rise times or short-term variations. In Section 4.2.1, we describe the modifications our detection pipeline from Terwel et al. (2024). In Section 4.2.2, we discuss the identification of false positives and in Section 4.2.3, we describe a method of obtaining a rough estimate of potential CSM masses to explain any observed late-time signals.

4.2.1 Detection pipeline modifications

Our main modifications to the pipeline presented in Terwel et al. (2024) are in the method of the baseline correction and the removal of the tail fitting procedure that was put in place to remove false positives from detecting the end of a normal SN Ia tail decline. In Terwel et al. (2024) the baseline correction was done by using the pre-SN observations, as late-time signals are expected in the observations only after the SN explosion. This cannot be done in our current sample since the date of explosion is not contained within the ZTF data time frame. Instead, we have to consider that a period with flux excess could occur any time during the ZTF observations.

Therefore, we run the pipeline several times using three different time frames for the baseline corrections. These time frames are chosen at the start, middle, and end of our ZTF light curves (see Table 4.1). We choose the baseline time frames to each be a year long to ensure that the targets are likely to have been observed, even if there are gaps in the observations due to the target location not being visible the entire year. We also choose not to include the first few months of ZTF data in the first baseline region as the final calibrations were not completed until July 2018 (Bellm et al., 2019b). By using different baseline regions we ensure that we bin the entire light curve multiple times (since the region used for the baseline corrections cannot be included in the light curve binning). If one of the baseline regions overlaps with the late-time signal the result can be a false baseline correction. By using multiple baseline regions these cases can be more easily be identified.

To ensure that there were enough points in each baseline region for a robust cor-

rection, we ignore all detections where the band in which the detection was found had < 30 points in the baseline. Table 4.1 shows the number of objects that meet this condition within each baseline region in each of the observational bands. In total, 989 objects never meet this condition in any band and are effectively removed from our sample, reducing the sample to 7718 objects.

A fitting procedure to identify the post-peak radioactive tail components of SNe Ia was used in [Terwel et al. \(2024\)](#). This was to distinguish between a normal SN Ia tail that was still visible ~ 100 days after the peak when the binning started and detections that could not be attributed to the decay tail of a normal SN Ia. Since the sample in this paper consists of transients that were first detected and expected to have (mostly) faded before the start of ZTF, this procedure is not needed. Also, we do not restrict ourselves to just SNe Ia, but search for late-time signals in any transient discovered in the 10 years before the start of ZTF. Therefore, for example, a procedure trying to find a SN Ia tail in a SN II event will always fail to do so.

4.2.2 Removing false positives

The pipeline outputs a list of 504 objects that have 5σ or greater binned detections in a band in at least four out of 16 attempts (four bin sizes, each shifted four times to avoid spurious detections caused by specific bin placement, see [Terwel et al. 2024](#) for more details). These are inspected visually to determine if the detections are due to observational issues, software issues, or if it is likely astrophysical in nature. A large fraction of the flagged light curves were deemed false positives after visual inspection. The main causes of the binning program wrongly finding bins with detections are due to issues in the difference imaging processing or the baseline correction.

To investigate these cases, we use the SuperNova Animation Program (SNAP¹) to inspect the difference images directly. Details on SNAP are presented in [Terwel et al. \(2024\)](#). Many false positives are identified as close to another source by inspection of the difference images. Usually this other source is the host galaxy (nucleus) but in

¹https://github.com/JTerwel/SuperNova_Animation_Program

some cases it can also be a foreground star. This can lead to an issue with an improper subtraction of the bright source, which results in a residual, generally a dipole, at the position that is picked up by our pipeline. To identify these cases, we use SNAP to visually inspect the images and remove spurious detections. This removes 155 events from our sample.

The other main group of false positives (88 cases) are flagged due to issues in the baseline determination. These can present as extremely large corrections, in some cases several orders of magnitude larger than the signals we expect to find. A baseline correction of $\mathcal{O}(10^5)$ can make a 17.5 mag signal appear or disappear. While in some cases big corrections are needed (see Section 4.3.1) in most cases such a correction led to noisy light curves, preventing us from probing beyond the individual ZTF image mag limit. In other cases the baseline is not constant but seems to vary over time or suddenly jump, making it very difficult or impossible to apply a proper baseline correction.

One potential cause of these issues could be due to ZTF continuing to improve the reference images by rebuilding them and stacking more observations, including observations from during the survey (Masci et al., 2019). To be able to compare observations from before and after this is done, one should remake all the difference images using the updated references. However, this is not feasible in a survey as large as ZTF, and since the offsets are usually below the noise threshold of the individual images the issue is of little importance to most of the survey science outputs. Only when attempting to go beyond the single image noise limit using, for instance, our binning method, this issue becomes noticeable enough and can lead to baseline offsets and varying or jumping baselines.

In 19 cases there were enough points in the baseline for the object to stay in our sample but the light curve was sampled sparsely with large gaps without observations surrounding sparse detections, making it impossible to determine the validity of these detections as there are no proper non-detections close in time to compare against.

Table 4.1: Details of the three baseline regions used in our pipeline. The first column gives the start and end MJD of each baseline region, and the second column gives its length in days. The last three columns give the number of transients that had at least 30 points in the baseline to provide a robust estimate of the baseline, in the g , r , and i band, respectively

Baseline region (MJD)	Length (d)	No. passing cuts		
		g	r	i
58300 – 58664	365	6817	7198	744
59031 – 59395	365	7251	7258	3447
59915 – 60335	422*	4792	5350	2457

* The light curves were generated between 9 December 2023 and 24 January 2024, meaning that the final baseline for each object is between 374 and 420 days long. The final two days are a buffer to ensure all data is used.

4.2.3 Estimating CSM masses

In Sect. 4.3.4, we describe our final shortlist of late-time flux excesses that cannot be explained by other sources. To determine if they are potentially due to CSM interaction signatures, we can make a rough estimate of the CSM mass required to generate such a signal. In this section, we describe the method used by Graham et al. (2019b) to put constraints on the CSM mass of their targeted SNe at similar epochs to ours, based on the observed near-ultra-violet (NUV) (non-)detections using the models of Harris et al. (2016). While CSM is line dominated, especially by H α , it is much more difficult to estimate a CSM mass without making many assumptions about the state of the CSM. Even though the statistical errors can be large, the resulting CSM masses for some of the objects in Sect. 4.3.4 is still unreasonable.

Assuming that the time of the late-time detections correspond to the peak of the CSM interaction light curve, Graham et al. (2019b) showed that the Bremsstrahlung spectral luminosity L_ν at frequency ν at the moment the interaction shock reaches the outer edge of the shell is

$$L_\nu \approx 1.63 \times 10^{-31} T^{-1/2} t_r^{-3} M_{\text{CSM}}^{17/7} e^{-\frac{h\nu}{kT}} y(F_R) \text{ erg s}^{-1}, \quad (4.1)$$

where T is the temperature of the shocked material in Kelvin, $t_r = t/(1+z)$ is the time after explosion in seconds in the rest frame of the SN at which the ejecta reach the

outer edge of the CSM shell and the interaction is assumed to be at its strongest, M_{CSM} is the CSM mass in grams, and $y(F_R) = F_R^{-3/7}(1 - F_R^{-3})^{-10/7}$ is the dependence on the fractional radius of the shell $F_R \equiv R_{\text{out}}/R_{\text{in}}$. Here R_{out} and R_{in} are the outer and inner radius of the CSM shell, respectively. $F_R = 1.1$ represents a thin nova-like shell, with higher values representing thicker shells. This equation assumes a low density, fully ionized H-dominated CSM to be the emission source after the interaction.

[Graham et al. \(2019b\)](#) derive Eq. 4.1 to use in the NUV and assume temperatures around 10^8 K. In these conditions the exponential term is near unity and can be ignored. Since we are targeting optical wavelengths, if the mechanism described here is the source, lower temperatures are needed where the exponential term cannot be ignored. The other assumptions made in [Graham et al. \(2019b\)](#) still hold for optical wavelengths, so we can use Eq. 4.1 to estimate the M_{CSM} required to explain any detected late-time signals using

$$10^{-0.4M} = \frac{L}{L_0} = \frac{L_\nu c}{L_0 \lambda}, \quad (4.2)$$

with M the absolute magnitude of the detected signal, c the speed of light, $L_0 = 3.0128 \times 10^{35}$ erg s $^{-1}$ the zero point luminosity, and λ the effective wavelength of the band we are considering (4746.48 Å, 6366.38 Å, and 7829.03 Å for g , r , and i , respectively). By combining Eq. 4.1 and Eq. 4.2 we get

$$\frac{M_{\text{CSM}}}{M_\odot} \approx 3 \times 10^{-8 - \frac{14}{85}M} \left(\frac{T}{K}\right)^{\frac{7}{34}} \left(\frac{t/(1+z)}{\text{days}}\right)^{\frac{21}{7}} \left(\frac{\lambda}{\text{\AA}}\right)^{\frac{7}{17}} e^{\frac{7hc}{17kT\lambda}} y(F_R)^{\frac{-7}{17}}. \quad (4.3)$$

We can obtain M , t , and z directly from our shortlist of transients with potential CSM interaction. For t the start of the signal should be taken as this assumes the least delay due to a non-negligible light-crossing time across the CSM shell. The remaining parameters are the fractional radius of the shell and the temperature.

If we assume the CSM shell to be nova-like then $F_R = 1.1$. Equation 4.3 gives very massive CSM shells very easily, especially if a significant delay time before the onset of the CSM interaction is present. The required M_{CSM} can be somewhat lowered if

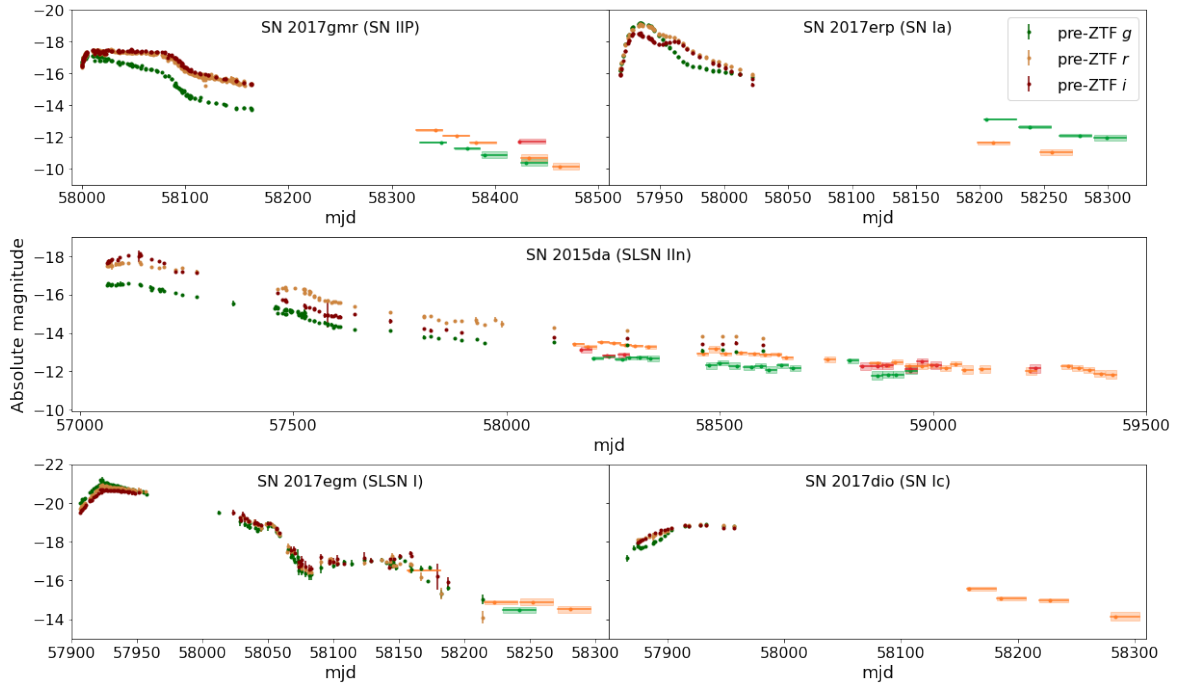


Figure 4.3: Examples of pre-ZTF SNe whose light curves have been recovered in the binned ZTF light curves. For each object we show the pre-ZTF g (dark green), r (dark yellow), and i (dark red) data points, as well as the binned ZTF detections (green, orange, red, respectively). The binned ZTF observations are in 25 day bins, with the width showing the beginning and end of each bin, and the shaded region shows its 1σ magnitude uncertainty. The pre-ZTF data was taken from [Andrews et al. \(2019\)](#) (SN 2017gmr), [Brown et al. \(2019\)](#) (SN 2017erp), [Tartaglia et al. \(2020\)](#) (SN 2015da), [Zhu et al. \(2023\)](#) (SN 2017egm), and [Kuncarayakti et al. \(2018\)](#) (SN 2017dio). None of the light curves are corrected for host extinction.

we assume that the actual thickness $R_{\text{in}} - R_{\text{out}}$ of the CSM shell remained constant after its creation, meaning that F_R decreases as the shell travels outwards. Since the SN ejecta move at a constant velocity, the distance of the CSM is proportional to the delay time of the interaction signal. If we assume a shell with $F_R = 1.1$ has a radius such that the late-time signal occurs at 300 days after the explosion, that same shell will have $F_R \approx 1.01$ if the interaction starts 3000 days after the explosion. We assume temperatures of 10^5 to 10^7 K, lower than the value assumed by [Graham et al. \(2019b\)](#) of 10^8 K, but more suitable for explaining optical emission.

In Section 4.3.4, we discuss the results of the CSM mass estimate for events with late-time flux excesses to determine if CSM interaction could be a plausible explanation. Equation 4.3 assumes that the magnitude is corrected for extinction. To get the lowest M_{CSM} possible we assume there is only Milky Way extinction in the line of sight of any of our targets. Any extinction in the host galaxy would make the intrinsic colour

of these objects bluer allowing for higher temperatures, but also raise the intrinsic absolute magnitude resulting in a higher overall estimate for M_{CSM} . The estimates should therefore be seen as lower limits.

4.3 Results

We have identified 98 transients with potential late-time excesses in their light curves that require further investigation. In Section 4.3.1, we describe the group of objects whose detections in ZTF can directly be linked to the pre-ZTF transient. These transients were still bright enough at the start of the ZTF survey to be detectable. In Section 4.3.2, we describe objects whose found ZTF signal is due to a sibling transient occurring at nearly the exact same sky position. A small fraction of our sample consists of non-SN transients, a few of which are returned by the pipeline and these are discussed in Section 4.3.3. Finally in Section 4.3.4, we describe the objects that required an individual, deeper investigation of the signal found in ZTF.

4.3.1 Pre-ZTF transients still active in ZTF

We chose to limit our sample to those objects that were first detected before 2018 to reduce the number of transients still visible at the start of ZTF. While this three month gap is enough for most transients to fade away, some super-luminous SNe, Type II-Plateau SNe, interacting classes like SNe Ibn and IIn, and even very nearby SNe Ia that exploded before ZTF started, may still be active during the ZTF survey time frame.

As these objects were active while the initial set of ZTF reference images were being produced, none of these objects have been found by ZTF even when the SN was still bright enough to be detected by ZTF once observing began. As the transient is in the reference images, it will cause an over-subtraction and leave an imprint, or ghost, at its location in the difference images. These are easily recognisable through visual inspection of the difference images using SNAP. Another clear sign is a significant

baseline correction that is consistent between the different baseline regions after the transient has faded away. The baseline correction corrects for the flux offset the ghost creates, revealing the tail as observed by ZTF in the light curve.

We find 63 transients whose ZTF detections are consistent with on-going transient flux. These are listed in Table 4.6 and some example light curves are shown in Fig. 4.3. The light curves show pre-ZTF data taken from the literature for SN 2017gmr (Andrews et al., 2019), 2017erp (Brown et al., 2019), SN 2015da (Tartaglia et al., 2020), SN 2017egm (Zhu et al., 2023), and SN 2017dio (Kuncarayakti et al., 2018). SN 2015da is an extremely slowly declining SLSN IIIn event (Tartaglia et al., 2020; Smith et al., 2024) and its light curve extends in the binned ZTF data to approximately eight years after discovery. In SN 2015da, the pre-ZTF and binned ZTF light curves do not overlap exactly in magnitude at epochs when data from the different surveys are available (MJD 58300 – 58600), showing that our pipeline underestimates the brightness of the transient. This is because some SN flux is still present even in our latest baseline region during mainly 2023, as can be seen in the observations presented in Smith et al. (2024). Therefore, the baseline correction is too small causing the binned detections to be slightly too low.

4.3.1.1 AT 2017gpv - a 14hls-like event

AT 2017gpv, shown in Fig. 4.4, is an unusual event similar in nature to iPTF14hls (Arcavi et al., 2017; Sollerman et al., 2019) and SN 2020faa (Yang et al., 2021) that was detected by our pipeline in the ZTF data. It was originally identified by Gaia, which detected it repeatedly during the first 500 days after its discovery. It has also been detected by ATLAS, which has a rich *o*-band light curve between 100 and 300 days after discovery that shows a plateau followed by a shallow decline that is interrupted by a rebrightening event. The first detections in ZTF are visible even in the non-binned data beginning around 200 days after first detection and last for around 400 days. With the binned observations the object can be recovered for another 1000 days before it fades below the noise limit. Pan-STARRS also detected this object in the *w* band,

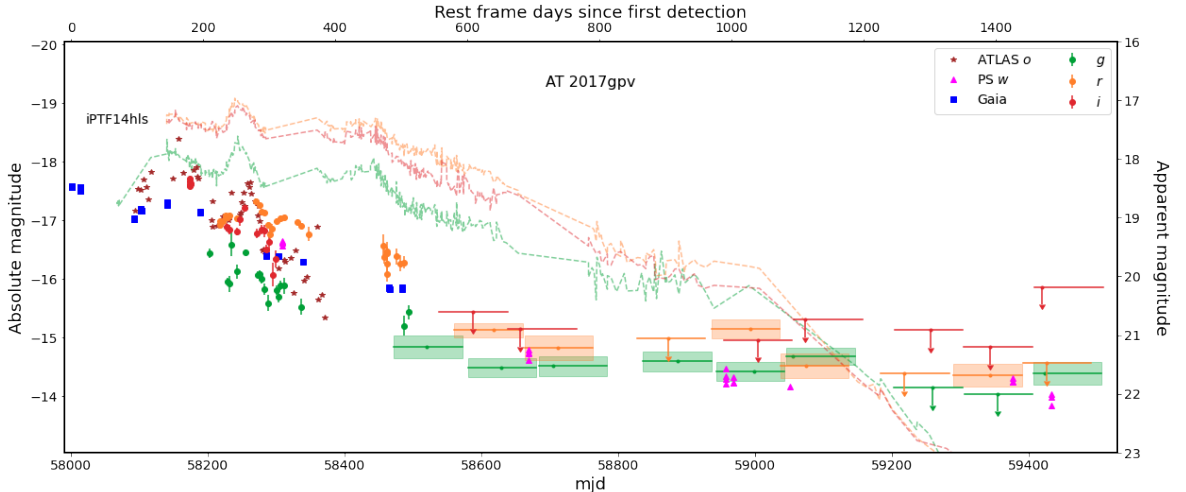


Figure 4.4: Light curve of AT 2017gpv with the axes representing absolute magnitude (left), apparent magnitude (right), the rest frame days since first detection (top) and mjd (bottom). Single epoch detections by ZTF, Gaia, Pan-STARRS and ATLAS are shown, as well as the binned ZTF observations after the transient faded below the single epoch noise limit. The dashed lines are the *gri*-band light curves of iPTF2014hls, which have been corrected for time dilation but not extinction (data taken from [Arcavi et al. 2017](#); [Sollerman et al. 2019](#)).

and given its deep detection limits it detected the transient up to over 1400 days after discovery.

Due to the long duration of detections of AT 2017gpv in ZTF, only the last baseline region can be trusted as it has the least contribution from the late-time signal, though given the slow decline of the transient it is likely that there could still be some excess present at the time of the last baseline region. As expected, the baseline corrections are significant, and SNAP clearly shows the transient in the reference images, as well as a significant ghost in all difference images. While it was picked up by the ZTF alert system and given an internal name (ZTF18acueiall), it was not recognized as a real transient.

Unfortunately, AT 2017gpv was never spectroscopically classified. The transient is at a distance of $6.88''$ from the host nucleus, removing host variability as a possible explanation, as well as limiting the amount of host extinction expected. The long time it was detectable and the bumpy nature of its light curves look similar to iPTF14hls ([Arcavi et al., 2017](#); [Sollerman et al., 2019](#)), a very peculiar SN II that is also shown in Fig. 4.4. Some similar events to iPTF14hls have been identified but they are rare ([Yang et al., 2021](#); [Soraisam et al., 2022](#)). The light curve of iPTF14hls spans over 600

Table 4.2: Pre-ZTF transients with a sibling transient detected in ZTF in single exposures. The first four columns give the name, type, discovery mjd, and redshift of the pre-ZTF transient, and the next five columns give the same information of its ZTF sibling when available. The second to last column gives an estimate of the peak r -band (unless specified otherwise) absolute magnitude of the ZTF transient assuming the pre-ZTF transient redshift, except for AT 2018iml as this is likely a foreground CV. The last column gives the separation between the siblings. A ? type means the transient was never spectroscopically classified. IAU names in parentheses are ZTF transients wrongly associated with a pre-ZTF transient.

Pre-ZTF transient				ZTF transient					
Name	Type	MJD	Redshift	ZTF name	IAU name	Type	MJD	Peak mag	Sep (")
SN 2017gcd	?*	57968	0.028593	ZTF19acdgwhq	(SN 2017gcd)	Ia-norm	58763	-18.8	1.02
AT 2017keg	?*	58068	0.05	ZTF19acihgng	SN 2019tka	Ia-norm	58781	-19.1 ^(g)	1.69
SN 2013ld	?*	56522	0.02741	ZTF18abavruc	SN 2021rgw	Ia	59393	-18.9 ^(g)	0.57
ASASSN-14ba	Ia pec/91T	56796	0.032668	ZTF22aaaawghw	AT 2022csd	II	59629	-16.8	1.29
SN 2017acp	II	57785	0.0215	ZTF19aavqics	SN 2019gxo	II	58633	-18.1	3.15
SN 2014gz	II	56678	0.02558	ZTF21abcpbqd	SN 2021nof	II	59362	-17.2 ⁽ⁱ⁾	0.30
SN 2009hz	II	55046	0.0253	ZTF18acotwcs	AT 2018iml	CV?**	58439	-	0.33
iPTF15wk	Ia	57097	0.23	ZTF21aaeebxm	-	?	59226	-20.0 ^(g)	0.31
SN 2016bsc	Ia	57500	0.05	ZTF23aaeljse	(SN 2016bsc)	?	60043	-17.9	1.61
SNF20080522-001	Ia	54608	0.04872	ZTF22aalbuig	AT 2022kuh	?	59724	-17.3	1.64
PS15ctg	Ia	57328	0.078	ZTF22abamjr	AT 2022rol	?	59806	-18.7	1.03
iPTF15eot	II	57357	0.039	ZTF19aakvysq	AT 2019bll	?	58541	-17.5	2.19

* Classified ZTF SNe that were wrongfully associated with the pre-ZTF name resulting in a mis-classification. The pre-ZTF transient itself was never actually classified In the cases of AT 2017keg and SN 2013ld.

** Not officially classified but based on evidence gathered from the ZTF forced photometry light curve.

^(g) Peak absolute magnitude in the g band.

⁽ⁱ⁾ Peak absolute magnitude in the i band.

days and is very bumpy. In both cases the explosion epoch is badly constrained, but the peak found in iPTF14hls matches up quite well with the bump around MJD 58250 in AT 2017gpv. Overall, AT 2017gpv looks like a fainter and somewhat faster decaying version of iPTF14hls. The late-time data of iPTF14hls ([Sollerman et al., 2019](#)) extends to \sim 1200 d after discovery and shows a sharp decline after \sim 1000 d, which is not seen in AT 2017gpv.

iPTF14hls is in our initial sample, but was not detected in ZTF because it is \sim 1000 days older than AT 2017gpv. Assuming that these two events evolved in a similar manner, iPTF14hls would have been close to the detection limit at the start of ZTF and faded below that before it could be picked up by our pipeline.

4.3.2 Siblings

Siblings are two (or more) transients that occur in the same host galaxy. While siblings can occur at any location in a galaxy (see e.g. [Graham et al., 2022b](#); [Dhawan et al., 2024](#), for a sample of ZTF-detected siblings), a subset of these occur with a small enough sky separation that part of the light of one sibling can be detected when performing forced photometry at the sky position of the other sibling. In [Terwel et al. \(2024\)](#), five such sibling pairs were found, with both transients detected within ZTF. With our current sample being larger and spanning a bigger time range over which the second transient can be observed, it is reasonable to expect a larger number of same-location sibling transients. We arbitrarily define siblings as a transient detected in ZTF *without* the use of additional binning to push the detection limit that are distinctively separate in time from the pre-ZTF transient at the same sky location. The ZTF transients do not have to be classified. We find 12 pairs of transients that satisfy these conditions, which we verified through the Fritz broker [van der Walt et al. \(2019\)](#); [Coughlin et al. \(2023\)](#). These are shown in Table 4.2.

In three cases, the ZTF-detected transient was classified but mistakenly associated with a pre-ZTF transient in WISEREP or OSC that subsequently got the same classification. In the case of SN 2017gcd, a decaying transient was observed in four epochs of unforced Pan-STARRS photometry, spread out over 125 days. This is enough to conclude that the 2017 transient was real and likely some kind of SN, but not necessarily a SN Ia.

In the two other cases (AT 2017keg/SN 2019tka and SN 2013ld/SN 2021rgw), the pre-ZTF detections are spurious and are unlikely to be true sibling pairs. AT 2017keg was reported by ATLAS in 2019 ([Tonry et al., 2019](#)) when SN 2019tka was found. Due to SN 2019tka being close to the host nucleus, likely spurious detections from two years before were present in the ATLAS light curve, resulting in the automated discovery report stating the wrong discovery date. SN 2019tka was reported by ZTF ([Forster et al., 2019](#)), which did not have such earlier detections as it only started

operating in 2018. SN 2013ld was reported in 2021 by Pan-STARRS1. Again, its sibling SN 2021rgw was on top of the host nucleus, which has had several epochs of minor variability. Even the internal ZTF name is from 2018, showing that ZTF also detected minor changes at the host nucleus location. When SN 2021rgw was found, ZTF issued an alert with the discovery date in 2021, resulting in SN 2021rgw (Nordin et al., 2021) while Pan-STARRS1 used the first unforced detection epoch in 2013 as the discovery date, resulting in SN 2013ld (Chambers et al., 2021).

For the other nine sibling pairs listed in Table 4.2, the pre-ZTF sibling has a classification (five SNe Ia and four Type II SNe) obtained at the time of discovery. Three of their paired ZTF siblings were spectroscopically classified as Type II SNe at the time of discovery in ZTF. For AT 2018iml, the sibling of Type II SN 2009hz, the ZTF detections were obtained in two periods (November 2018 and March 2024) and they are best matched to a CV. The remaining five had no ZTF-era classification. In some cases the ZTF sibling is close enough to get wrongly associated with the pre-ZTF sibling and obtain the same IAU name.

Assuming the five unclassified ZTF transients occurred in the same host galaxy as their classified sibling, we can use the known redshifts to estimate the absolute brightness of the unclassified transients and show that they are in the range of SNe and unlikely to be caused by late-time CSM interaction. ZTF21aae ebxm is found around 1800 days after its sibling, iPTF15wk, was first detected, and has an inferred absolute *g*-band magnitude of -20.0 at its peak at just $0.31''$ from iPTF15wk. To get such a strong signal this long after the explosion would require an unreasonably large CSM and thin shell, making CSM interaction an unlikely explanation. Its location is consistent with its host nucleus making a nuclear transient origin likely.

For ZTF23aaejse, ZTF22aalbuig, ZTF22abamjrf, and ZTF19aakvysq, their absolute peak magnitudes are in the range typical of SNe (-17.3 to -18.7 mag) and SNAP shows that there is a noticeable separation between the pre-ZTF and ZTF-detected signals (1.03 to $2.19''$), disfavouring any explanation that would require the two events to be at the same spatial position, such as CSM interaction. The inferred CSM masses

Table 4.3: Pre-ZTF transients detected in the binned ZTF light curves due to AGN or variable star activity. The original type and z values are as they were recorded on the OSC or WISeREP. The late-time type gives the reason for the ZTF detections.

Name	Pre-ZTF type	z	Late-time type
Gaia14adg	II	0.154	AGN
SN 2016fiz	II	0.05	AGN
SN 2017avb	II	0.096	AGN
LSQ12biu	IIn	0.136	AGN
SN 2017bcc	SLSN-II	0.133	AGN
PSN J0151 ⁽¹⁾	SLSN-II?/AGN	0.26	AGN
ATLAS17khl	AGN	0.06	AGN
PS17bgm	AGN	0.358	AGN
LSQ12ehj	AGN	0.12	AGN
AT 2017kas	SN candidate	0.031328	AGN
LSQ12fgx	Variable star	0	Variable star
SNhunt44	LRV? ⁽²⁾	0.0005864	Variable star
AT 2016ijb	SN candidate	-0.000781	Variable star
PTF10qpf	Variable star	0	Variable star

⁽¹⁾ PSN J0151 = PSN J01510869+3155215

⁽²⁾ Potential luminous red variable

to explain these events in this way are also unrealistically high. Their locations are inconsistent with their host nuclei. Therefore, we conclude that a sibling transient, likely a unclassified SN, is the most plausible explanation for these events.

4.3.3 Non-SN sources of flux excesses in ZTF

We identify some late-time excesses at the positions of our sample that are astrophysical but are due to known AGN activity or due to stellar variability. Ten transients (listed in Table 4.3) in our sample have been found to have genuine long-term variability due to an AGN that lasts for the whole time period of ZTF and is picked up by our pipeline. In each case, the source is a known AGN (verified through cross-referencing with SIMBAD, ZTF, and checking the AGN criterion from [Hviding et al. 2022](#) using the Wide-field Infrared Survey Explorer WISE [Wright et al. 2010](#)). Their light curves are shown in Fig. 4.8. While several of the pre-ZTF transients in this category have been classified as SNe II, some have high redshift, which suggests that these are AGN misclassified as SNe II.

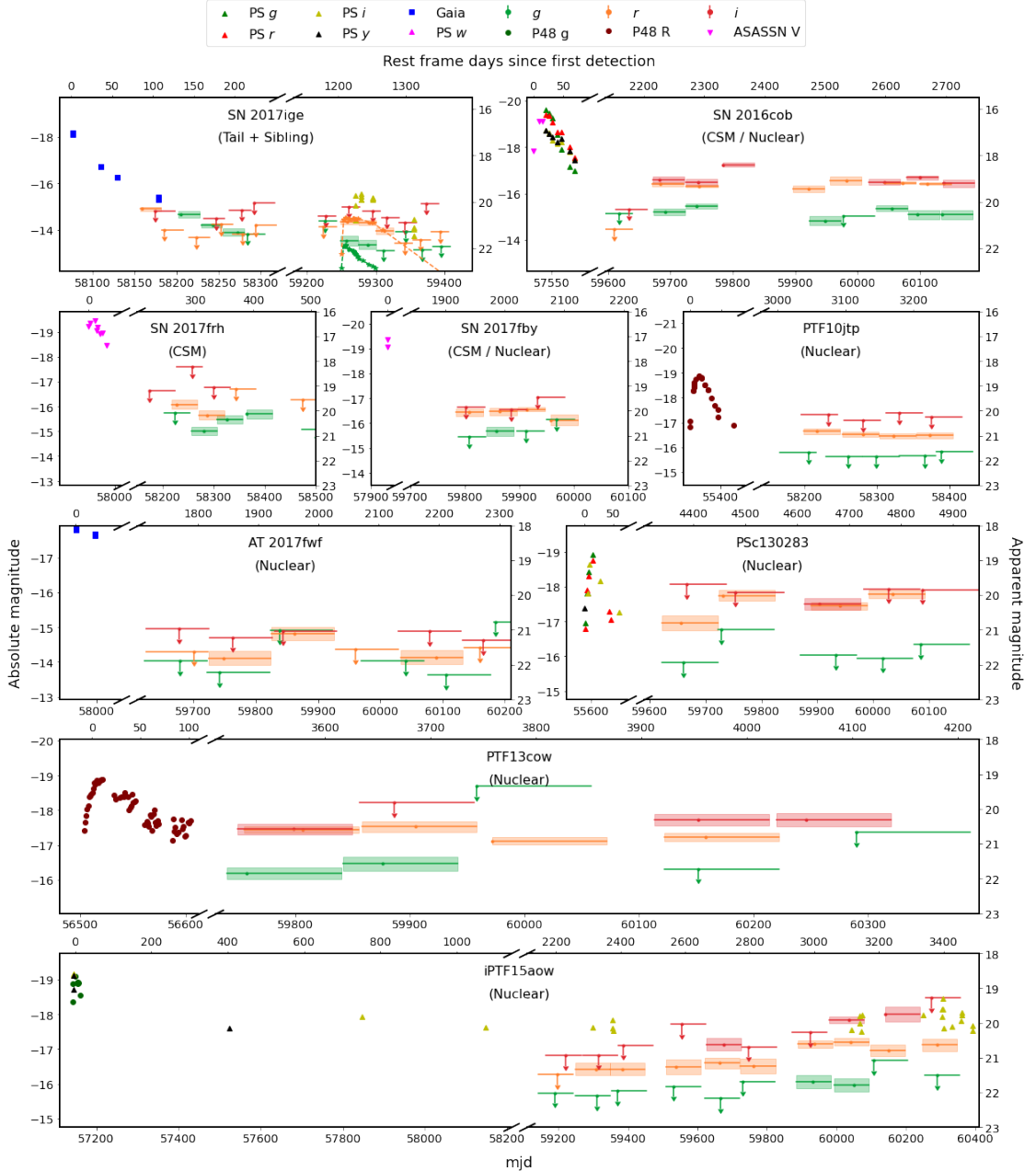


Figure 4.5: The nine objects whose late-time detections required a more rigorous investigation. Each object is shown in absolute and apparent magnitude (left and right axes respectively) and rest frame days since first detection and mjd (top and bottom axes respectively). We show the binned ZTF data with the late-time detections as well as pre-ZTF detections from other surveys (Pan-STARRS, Gaia, ASASSN, PTF) where available. For SN 2017ige a heavily extinct ($E(B-V)_{\text{host}} = 1.2 \text{ mag}$) light curve of SN 2020jfo is shown with dashed lines matching the late-time ZTF r -band detections. The objects are marked with the explanation for their late-time detections.

Table 4.4: Objects with detections whose origin was not immediately clear. The first five columns give information on the original transient, and the last six columns give an overview of the binned ZTF detections. Start gives the time after discovery of the first detections in ZTF, and duration gives the length of these detections. Both are in rest frame days and rounded to 10 days. The g , r , and i columns give the range of detections in absolute magnitude if detected. Inferred cause of excess gives the type of object that best explains the detections. The last two columns state whether the excess is consistent with the SN and host nucleus location, respectively.

Pre-ZTF					ZTF excess							
Name	Type	Discovery date	z	Host sep ('')	Start (d)	Duration (d)	g band abs. mag	r band abs. mag	i band abs. mag	Inferred cause of excess	Excess consistent with SN	Excess consistent with host nucleus
SN 2017ige ⁽¹⁾	Ia	17-11-17	0.02431	0.99	1190 ⁽²⁾	90	-13.5 – -13.3	-14.3 – -13.6	–	Sibling	yes	no
SN 2016cob	Ia-91T	26-05-16	0.02961	0.7	2200	490 ⁽³⁾	-15.3 – -14.7	-16.5 – -16.1	-17.2 – -16.4	CSM/Nuclear	yes	yes
SN 2017frh	Ia	17-07-17	0.032188	0.0	250 ⁽²⁾	190 ⁽³⁾	-15.6 – -14.9	-16.0 – -15.6	–	CSM	yes	yes
SN 2017by	Ia	01-07-17	0.043513	0.73	1940	200 ⁽³⁾	–	-16.5 – -16.1	–	CSM/Nuclear	yes	yes
PTF10jtp	Ia	04-06-10	0.067	1.11	3040	210 ⁽³⁾	–	-16.5 – -16.3	–	Nuclear	yes	yes
AT 2017wvf	Cand.	01-08-17	0.033707	1.67	1810	420	–	-14.7 – -14.0	–	Nuclear	no	yes
PSc130283	Ia	29-01-11	0.07622	0.44	4340	520 ⁽³⁾	–	-17.8 – -16.9	–	Nuclear	yes	yes
PTF13cow	Ia	07-08-13	0.086	0.56	3510	610 ⁽³⁾	-16.3 – -16.1	-17.4 – -17.1	–	Nuclear	no	yes
iPTF15aow	Ia	06-05-15	0.07597	0.92	2280	1130 ⁽³⁾	-16.0 – -15.9	-17.2 – -16.4	-18.0 – -17.1	Nuclear	yes	yes

⁽¹⁾ SN 2017ige has two separate periods with detections. The second is shown in the table while the first is consistent with the radioactive tail phase of the SN Ia. It starts at 80 d after discovery (the start of the ZTF survey) and lasts for 150 d declining from –14.6 to –13.8 mag over this time in the g band.

⁽²⁾ Detected from the start of ZTF.

⁽³⁾ Start or end with a gap in the binned observations or at the edge of available data.

We also recovered four long-term variable stars that are shown in Fig. 4.9 and listed in Table 4.3. The nature of these sources make it impossible to create a template that always subtracts them completely without leaving residual flux or a ghost as there may be no region without variability. However, if the variations in the source’s magnitude are large enough over a long period of time it will easily be picked up by the binning algorithm.

4.3.4 Final shortlist of late-time interaction

The final 9 objects in our sample cannot be put in any of the groups (on-going SN flux, sibling transient, nuclear activity, variable star) above. Each of these events is discussed individually below. Table 4.4 shows the general information of these events, and their light curves are shown in Fig. 4.5. The bin sizes and placement chosen for the plots are those that result in the clearest and cleanest signals. The baseline regions used are those that have the least amount of transient flux in them, which means they are the furthest away in time from the excess. As was done in Terwel et al. (2024), we compare the ZTF detections to several classes of transients in an attempt to explain

them as a previously unidentified sibling transient. We also estimate the potential CSM mass required to explain the late-time signature using the analysis method detailed in Sect. 4.2.3 for objects where a CSM interpretation cannot be ruled out.

SN 2017ige. SN 2017ige was initially discovered and classified as a SN Ia in late 2017, only a few months before the start of ZTF. As it was relatively close by, the radioactive tail phase was identified in the ZTF binned data out to ~ 200 d, before it faded below the noise limit. This tail matches well with the declining light curve seen in the early (< 100 d) Gaia data (see Fig. 4.5). SNAP shows that the SN is in the ZTF reference images, leaving a small ghost at its location in the difference images.

At 1200 days after the SN tail faded below the noise limit, a small excess is detected in both the ZTF *g* and *r* bands that lasts around 90 days. In the difference images a small excess can be seen semi-overlapping the negative imprint left by SN 2017ige during this excess. Such a dipole signal would usually suggest imperfect image subtractions, but in this case it can also be interpreted as a separate transient slightly offset from the location of SN 2017ige being over-subtracted due to the presence of a SN in the reference images.

The late-time excess has been detected by Pan-STARRS in their *i* band, given the internal name PS21aos, and linked to SN 2017ige based on the sky position, confirming that the excess found in ZTF at late times is real. The Pan-STARRS *i*-band detections are brighter than what was found in the ZTF *g* and *r* bands, likely due to a combination of the ZTF detections being underestimated as a result of the ghost of SN 2017ige, as well as the late-time excess being intrinsically red ($(g - r) \approx 1$ mag).

We use the duration and shape of the identified excess to test if it could be explained as a sibling transient. A light curve similar to that of SN 2020jfo (Sollerman et al., 2021; Ailawadhi et al., 2023), a Type IIP SN with a relatively short plateau, fits the excess quite well in duration and absolute magnitude when a host extinction of $E(B - V) = 1.2$ mag is added. Given that the sky position at which the forced photometry was performed is only $0.99''$ from the host nucleus of an edge-on galaxy,

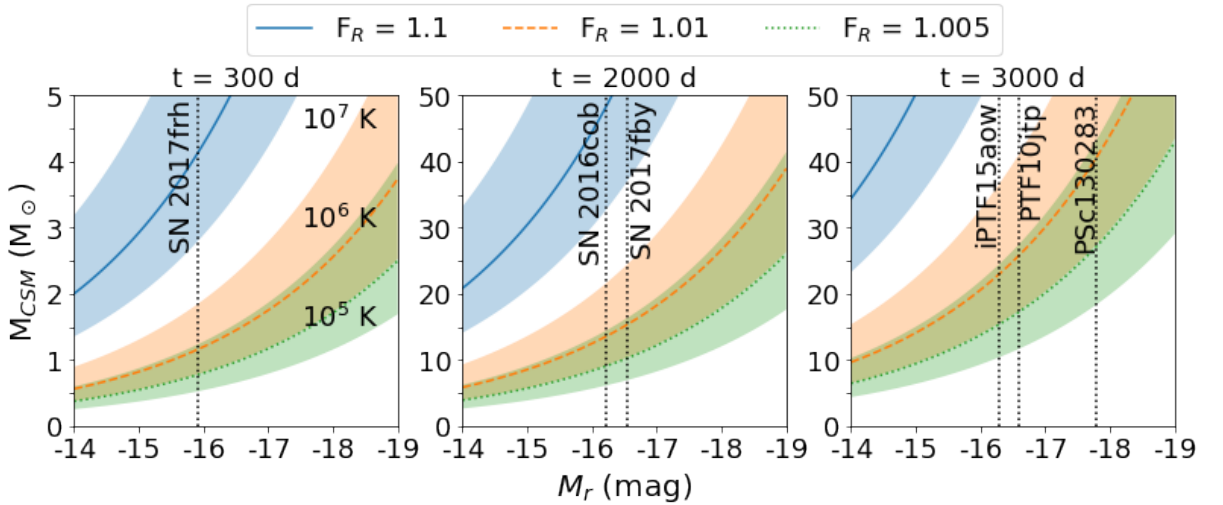


Figure 4.6: M_{CSM} as a function of the r -band absolute magnitude M for different assumptions of t (panels), T (shaded region), and F_R (colours). The five objects for which we estimate M_{CSM} in Sect. 4.3.4 have been marked in the panel that has t the closest to the detected signal. Decreasing shell thickness and temperature to mitigate M_{CSM} is effective, though there is a limit to far this can be done while keeping realistic values for F_R .

such a high amount of extinction is plausible. The original peak of the light curve of SN 2017ige in 2017 was not caught so a comparison with a similar extinction estimate cannot be made. Although close to the nucleus, inspection of the images shows that it is offset from the host centre as well as the original SN position. Therefore, we conclude that a Type II SN sibling with a relatively high value of extinction is an adequate explanation for this late-time excess.

SN 2016cob. SN 2016cob was classified as a SN Ia of sub-class 91T-like at early times. There is light curve data from Pan-STARRS and ASASSN around peak and extending to just past 50 d from peak. In the ZTF binned data, this event jumps up from non-detections to detections in all three bands around ~ 2200 d after first detection (Fig. 4.5). The i -band data is included for completeness but does not have reliable baseline estimate (> 30 points per region) so the values should be treated with caution. The detections are present in all bands at the same time and extend for at least 490 d at absolute magnitude of -15 to -17 mag. No SN-like transient can explain this long-lived flux excess.

Following the calculation in Section 4.2.3, if we assume a CSM shell with a fractional

radius of ≈ 1.005 at a temperature of 10^5 K, this gives $M_{\text{CSM}} \approx 6 M_{\odot}$. In Fig. 4.6 we show the M_{CSM} as a function of the r -band absolute magnitude, M_r , for three different times of the onset of the CSM interaction (300, 2000, 3000 d), three different F_R values (1.1, 1.01, and 1.005) and temperatures of 10^5 to 10^7 K. This value of $M_{\text{CSM}} \approx 6 M_{\odot}$ is a large CSM mass but around the same value as suggested to explain the interaction signatures seen in SN 2002ic (Hamuy et al., 2003b). Based on this, we put SN 2016cob forward as a candidate late-time CSM interaction, though we note that it would require a very thin shell ($F_R = 1.005$).

SN 2016cob is $0.7''$ from the host nucleus, putting the nucleus on the same or an adjacent pixel in the ZTF observations. This leaves room for a host variability interpretation, though the host has no AGN according to its WISE colours. SNAP does not show any reduction or subtraction issues that could explain the ZTF detections as a spurious source either.

The absolute magnitude, duration, and nuclear location are consistent with the ambiguous nuclear transient (ANT), ASASSN-20hx/AT 2020ohl (Hinkle et al., 2024). ANTs are events that cannot be easily classified into AGN activity or TDE. AT 2020ohl displayed a plateau or very slow decline in its optical light curves for >250 d relative to peak with an approximate plateau magnitude in the gri bands of -17.5 mag. In Fig. 4.7, we compare the light curves of the shortlisted transients that are consistent with their host nuclei compared to AT 2020ohl. The flux excess at the position of SN 2016cob is shown as blue squares and is slightly fainter than AT 2020ohl. AT 2020ohl had an observed rise-time of 30 days (Hinkle et al., 2024), slightly larger than our smallest bins. This would explain why no rise is detected, as our time resolution is too poor to detect time variations of this scale. We can only observe a sudden appearance of a very flat light curve. Both late-time CSM interaction and an ANT are adequate explanations for the identified signal, and without additional information we cannot decisively point at one of these two explanations.

SN 2017frh. SN 2017frh was discovered by ASASSN and spectroscopically clas-

sified as a SN Ia. A flux excess was detected in the binned ZTF g and r bands at absolute magnitudes of -15.3 and -15.8 , respectively. Only i -band upper limits were obtained. The detections were visible from the start of ZTF at a phase of 250 d after discovery and lasted for 190 d before disappearing behind the Sun. Nothing is detected after its return. The detections are found regardless of the baseline region that is used.

These detections are inconsistent with a normal SN Ia at these phases, which would have a significantly lower absolute magnitude ($M \approx -12$ mag) and also keep fading over time. If it were some type of sibling transient it would have to plateau at -15 to -16 mag for at least 180 d. No known class of SN shows this behaviour without the help of CSM interaction.

The late-time detections in SN 2017frh have a similar absolute magnitude and duration to the three late-time CSM interaction candidates that were presented in [Terwel et al. \(2024\)](#). However, the interaction in SN 2017frh starts significantly earlier (~ 240 d) than for those events. If we assume $F_R = 1.1$, a M_{CSM} of $1.8 M_{\odot}$ would be required to explain both the g and r bands assuming $T = 10^5$ K. Raising the temperature to $T = 10^7$ K gives $M_{\text{CSM}} \approx 4 M_{\odot}$ for the g band and $M_{\text{CSM}} \approx 4.5 M_{\odot}$ for the r band. SN 2017frh is shown in the left-hand panel of Fig. 4.6. If the F_R is reduced to 1.01, then the the CSM mass is lowered to between 0.5 and $1.2 M_{\odot}$. These mass estimates are in line with the suggestions of previous interacting SN events ([?Inserra et al., 2016b](#)). For these reasons, we classify SN 2017frh as a candidate SN with late-time CSM interaction.

The late-time excess at the position of SN 2017frh is also on top of the host nucleus, which could mean that the late-time signal is instead related to the host. However, the duration of the detected signal is the shortest of those shown in Fig. 4.7, although there is an observing gap at the end of the detected signal so no strict limit can be placed. Late-time CSM interaction signatures have been found in SNe Ia at similar phases ([Graham et al., 2019b](#)). Therefore, given the relatively low CSM mass required and the time frame of the interaction, we prefer the CSM interpretation for this late-time signal.

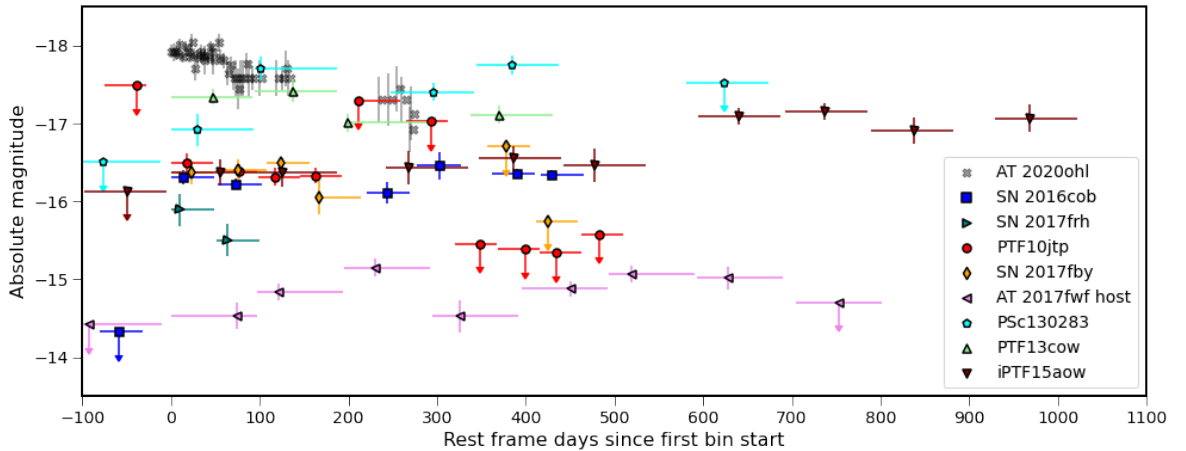


Figure 4.7: Binned r -band observations of the objects whose late-time detections are consistent with a galaxy nucleus (see Table 4.4) and are potentially transient events unrelated to the original SN. Upper limits are shown with downward arrows. The r -band light curve of the slowly evolving ambiguous nuclear transient AT 2020ohl (ASASSN-20hx, Hinkle et al. 2022) is also shown for comparison. As the late-time signal in AT 2017fwf was found to be significantly offset from the SN location we show the processed light curve at the host nucleus location instead.

SN 2017fby. SN 2017fby was discovered by ASASSN and spectroscopically classified as a SN Ia. The ZTF binned r band detections at an absolute magnitude of -16.3 are found when the sky location returns from behind the Sun at 1940 d after discovery and lasts 200 d until it becomes unobservable again. The light curve stays roughly constant over this time frame. There are hints of a g band excess as well but only one bin is above the 5σ threshold. After it comes back from behind the Sun nothing is detected anymore.

With a much stronger r band signal compared to the g band, one could argue for this being a reddened previously unknown sibling transient whose rise was missed due to it occurring while the sky position was too close to the Sun to be observed. However, the long plateau in the light curve of at least 190 d rules this out – Type IIP SNe have plateaus that are generally significantly shorter than this (Barbon et al., 1979; Anderson et al., 2014)

If we assume the detections could come from a CSM shell with a fractional radius as low as $F_R \approx 1.005$, this gives a required CSM mass of $M_{\text{CSM}} \approx 5.5 M_\odot$ according to the calculation in Section 4.2.3. This is around the upper end of the CSM masses that

have been estimated for known SNe Ia-CSM such as SN 1997cy (Chugai & Yungelson, 2004), SN 2002ic (Chugai & Yungelson, 2004; Inserra et al., 2016b), and SN 2012ca (Inserra et al., 2016b). Therefore, we note SN 2017fby as a SN with potentially late-time interaction with a thin, massive shell of CSM.

Checking the difference images with SNAP shows a clear bright spot at the SN location during the period of detections and no clear issues before or after it, confirming the excess to be real. At a distance of $0.73''$ (0.66 kpc at the host redshift) from the host nucleus, a TDE or other nuclear transient would likely appear on the same or adjacent pixel in the ZTF images. Like for SN 2016cob, this makes it difficult to say whether late-time CSM interaction or an ANT is the best explanation for the signal (Fig. 4.7).

PTF10jtp. PTF10jtp was discovered by PTF and classified spectroscopically as a SN Ia. Detections were made in the ZTF binned r -band light curves starting at 3040 d after discovery. It had a ~ 200 day r -band plateau around -16.4 mag before the sky position became unobservable. When it came back from behind the Sun, there are 5σ upper limits that are about one magnitude deeper than the previous detections (not shown in Fig. 4.5).

The g band has upper limits at approximately -15.5 mag during this entire period, while the i band bins are not deep enough for a constraining upper limit to be placed. The baseline correction in r is significant and comparable between the later two baseline regions, but is somewhat smaller in the first region as it partially includes the period in which the excess was detected. This suggests that the excess was present in (some of) the reference images, and the late-time excess was present for longer than was found with the binning procedure. SNAP confirms this, as a slight excess can be seen in the difference images, followed by a small ghost at later times.

As this excess occurs over eight years after the SN, any SN Ia radioactive tail contribution at this magnitude can immediately be ruled out. Although there are only detections in one band, the limits placed on the colour together with the > 200 day

plateau limit the possibilities for a sibling, even with moderate values of extinction.

An unreasonably thin shell of CSM is needed to explain detections that are this late and still have an absolute magnitude of $M \approx -16.5$ while keeping the total mass of to be at most $M_{\text{CSM}} \approx 5 M_{\odot}$ in line with literature events. A CSM mass of at least $10 M_{\odot}$ would be required. Therefore, we rule out CSM interaction as a likely explanation for this late-time flux excess.

The sky location is $1.11''$ from the host nucleus, and SNAP also shows that the excess is slightly offset from the SN location in most frames and consistent with the host nucleus. The long duration of the excess, combined with the central location, suggests host activity is the cause, although it is not an AGN according to its WISE colours. Therefore, a nuclear transient is the most likely explanation for these late-time detections. Its light curve is shown compared to the ANT AT 2020ohl in Fig. 4.7, where it is seen to be plausibly consistent in duration and absolute magnitude.

AT 2017fwf. This object was only detected by Gaia at early times with no spectrum obtained, preventing even a speculative classification based on the photometry. It is detected in ZTF binned r band data starting at 1810 d after discovery and this lasts for 420 d. The light curve rises from -14 to nearly -14.7 mag before slowly fading again. Despite having upper limits around the same magnitude as r , nothing was detected in g . The i band limits are shallower and less constraining. SNAP shows that the excess is real, but located at the nucleus location $1.67''$ from the SN. Therefore, CSM interaction can be ruled out. The long timescale of the transient also makes a SN-like transient unlikely.

Performing forced photometry at the host nucleus location reveals its properties much more clearly, being visible for nearly 700 days and reaches -15.2 mag at its brightest (see Fig. 4.7). This is longer by nearly 300 days and brighter by nearly 0.5 mag than the values given in Table 4.4 for the forced photometry at the SN position. The host galaxy is not an AGN according to its WISE colours. The excess is still very faint for a TDE unless it is heavily reddened, although a reddened TDE would likely

have been bright enough in the i band to still be visible. However, an ANT could be possible, but the signal is three mag fainter than AT 2020ohl but also visible for over twice as long. Faint nuclear variability could also be possible and there is some scatter in the light curve but with our 100 d bins for the light curve, small-scale variability can not be identified. Therefore, we can only conclude that some sort of nuclear variability is present.

We note that a sibling transient is also detected by ZTF in this host galaxy (SN 2020ackb, SN IIP), though it is at a distance of $5.23''$ and has no effect on the forced photometry at the location of AT 2017fwf. The time at which the sibling was visible also does not correspond with the detected host variability.

PSc130283. PSc130283 was detected by Pan-STARRS and spectroscopically classified as a SN Ia. At 4340 d past discovery, ZTF-detections are found in the r band at an absolute magnitude of -17 mag before brightening again to -17.8 mag in the next bin and staying there with variation ≤ 0.5 mag for the remainder of the light curve (at least 520 d). The non-detections before the start of the excess were up to 1.5 mag lower, suggesting that the excess started suddenly rather than a gradual brightening. During the entire late-time excess, the g band stays with 5σ upper limits at -16 mag.

Detections this late ($\gtrsim 4300$ days) and bright ($M \sim -18$ mag) cannot give a reasonable M_{CSM} in Eq. 4.2.3 unless a temperature around $10^{4.5}$ K and $F_R < 1.0005$ is assumed giving an unreasonably thin shell and no extinction between the SN site and us. Therefore, we rule out CSM interaction as a likely cause of the late-time flux excess.

SNAP shows a clear excess that is consistent with the SN location, and no ghost or residuals before the excess starts or image defects that could explain these detections. However, the flux excess is only $0.44''$ from the host nucleus, although the host is not an AGN according to its WISE colours. The host has a history of small variability that causes sparse detections (including a detection that put its discovery date over 400 days before the SN explosion), which points to the ZTF detections in the binned data

to be host related. Out of all excesses plotted in Fig. 4.7, PSc130283 is the brightest. It is very similar in brightness to AT 2020ohl though a bit longer in duration. These properties, combined with its relatively sharp rise suggest nuclear variability, such as an ANT, could explain these detections.

PTF13cow. PTF13cow was discovered by PTF and classified as a SN Ia. The late-time detections in the ZTF *gri* bands begin 3510 d after discovery at absolute magnitudes of -16.0 and -17.3 mag in the *g* and *r* bands, respectively. There are detections in the *i* band, however the baseline is too small for these to be considered any further here. The *r* band detections last for at least 610 d. The *g* band is only detected at the start but is significantly fainter and disappears below the detection threshold earlier. This long timescale rules out SN-like transients as a cause for the excess.

SNAP shows there is a clear excess in the images, and despite the host nucleus distance being only $0.56''$ from the SN location, the SN location and host nucleus are on different pixels. The excess has a preference to be at the host nucleus location, suggesting it is the cause of the signal. However, the host nucleus is not an AGN according to its WISE colours. The duration of over 560 d and a peak absolute *r* band magnitude of -17.4 of the identified late-time excess is similar to AT 2020ohl, meaning that an ANT could explain these detections.

iPTF15aow. iPTF15aow was discovered by the intermediate PTF survey (iPTF), as well as detected in Pan-STARRS and classified as a SN Ia. The late-time detections begin in the *r* band at 2280 d after discovery at -16.4 mag. There are only upper limits in the *g* and *i* bands at this time, but at later times some detections in these bands are made. The detections last for at least 1050 d and slightly brighten with time to -17.2 mag in the last bins. The long-lived nature rules out SN-like transients at the same position as the original SN Ia.

Even when assuming a scenario where the *r* band interaction stays at the level it

was discovered at for the entire duration it was detected, $> 5 M_{\odot}$ of CSM is required in a very thin, low temperature shell. However, the signal increases in strength over time, which would increase the required CSM mass. On top of that, no known SN Ia with CSM interaction has interaction as long as the late-time excess is found for or with the strength increasing over time, further disfavouring the CSM explanation.

The host nucleus is close by at $0.92''$ but from SNAP the transient does not look to significantly favour the SN or host nucleus location over the other. The host is not an AGN according to its WISE colours ($W1 - W2 = 0.077$ mag, $W2 - W3 = 1.564$ mag).

Pan-STARRS has some detections in the unforced photometry at the SN location, the first being at the time of iPTF15aow's discovery. However, it has no internal name. In the years after the first detection there are some detections in their i band but these are likely spurious because of a significant number of upper limits in between them that are not shown in Fig. 4.5. The number of Pan-STARRS i band detections increased significantly after ~ 2900 d after discovery, which corresponds to the brightest part of the binned ZTF detections.

The duration, shape, and close proximity to the host nucleus of the excess point to it being most likely host related. It has a similar brightness to AT 2020ohl, but has a several times longer duration and is still going. The fact that it continues to brighten is also very unusual. None of these signatures are consistent with what would be expected from a late-time CSM interaction.

4.4 Discussion

In this study we gathered a sample of 8707 transients that were first detected between 1 January 2008 and 31 December 2017 whose locations have been observed by ZTF between 2018 and 2023. By performing forced photometry on all ZTF observations at the target locations we created late-time light curves for all transients in our sample, often reaching over 10 years after the first detection. Using the pipeline from [Terwel et al. \(2024\)](#) we binned the ZTF light curves to search for the presence of faint previously

Table 4.5: Number of recovered signals for each SN type in our sample. As it is unclear whether SN 2016cob and SN2017fby should be counted as nuclear transients or due to CSM interaction, they have been counted in both.

Type	No.	Siblings		Nuclear		CSM	
		No.	%	No.	%	No.	%
Ia	5618	6 ^(a)	0.1	7	0.1	3	0.1
II	1494	4 ^(b)	0.3	0	0	0	0
Ib/c	385	0	0	0	0	0	0
IIn	310	0	0	0	0	0	0
I	69	0	0	0	0	0	0
Ibn	18	0	0	0	0	0	0

^(a) This includes the unconfirmed but likely sibling at the position of SN 2017ige determined from our binned light curve analysis.

^(b) This includes one sibling pair (SN 2009hz/AT 2018iml) where the ZTF transient was a likely CV based on its light curve.

undetected signals. We find 98 cases with detections that cannot be explained as false positives due to observational, reduction or software issues. These objects can be split into four groups: i) ongoing signatures of bright and/or nearby transients that were still detectable at the start of ZTF, ii) sibling transients at nearly the exact same location on the sky, iii) known variable sources such as AGN and variable stars, and iv) nine late-time flux excesses that required a more in-depth examination. Of these nine, we concluded that one was a sibling SN, five cases were nuclear transients close to the SN locations, two objects where it is unclear whether the ZTF signal is host or CSM related, and one SN whose ZTF-detections are most consistent with late-time CSM interaction.

4.4.1 Rarity of late-time signals from SNe

We started our search for late-time signals based on the positions of 8707 transients discovered before ZTF. Table 4.5 shows the number of objects that had detections in ZTF, split over the six main types of SNe we distinguish between in our sample. In the sections below, we discuss the main conclusions for each of the likely classes (siblings, nuclear, CSM) of the late-time signals detected.

4.4.1.1 Siblings

Within the uncertainties the rate of siblings found is the same for the different groups of objects with the SN Ia and Type II SN classes having rates of sibling discovery of $0.1 - 0.2 \%$. The percentage is similar, given the large uncertainties associated with low numbers of events, to the percentage of siblings found in [Terwel et al. \(2024\)](#) over a smaller time frame. These rates can be taken as lower limits because of observing gaps, which would result in transients being missed. In total, we found 10 siblings out of 7718 light curves that could be binned gives a lower limit on the rate of siblings of $0.13 \pm 0.04\%$. SN Ia sibling pairs along the same line of sight may be useful for constraining the origin of reddening in SN Ia light curve fitting for cosmology ([Dhawan et al., 2024](#)), but a larger sample would be required for meaningful constraints.

4.4.1.2 Serendipitous nuclear transient detections

We identify five late-time signals that were most likely due to host activity that was (partially) picked up in the forced photometry at the SN location. This was determined due to a combination of the shape and duration of the late-time light curve, as well as the inferred M_{CSM} from the absolute magnitude and delay between the main SN and late-time detections being unrealistically high in the best case scenario. We also identify signals at the positions of two events (SN 2016cob and SN 2017fby), where the inferred cause could be CSM or nuclear activity, bringing the total to seven potential nuclear events (see Table 4.5).

In Fig. 4.7, we show the late-time excess light curves for which nuclear transients can not be ruled, along with the late-time light curve of SN 2017frh for completeness, although we prefer a CSM interpretation for it. The light curves are shown as absolute magnitude in the r band against the time since the first binned data where a flux excess is identified. We also show the ANT AT 2020ohl ([Hinkle et al., 2022](#)) for comparison. AT 2020ohl is slightly brighter than most of these transient events apart from PSc130283. Our events are also longer lasting, ranging from ~ 200 days up to

~ 1100 days. This could mean that there is a previously unknown population of lower luminosity ANTs that require deeper (binned) observations to be detected.

[Wiseman et al. \(2024\)](#) showed that their sample of ANTs all have changes in their WISE $W1$ - and $W2$ -band observations, with a slight delay compared to the optical. We investigated the WISE light curve for our potential nuclear transients but unfortunately, these light curves use the total measured flux from the source. As the hosts of our nuclear transients have an apparent magnitude of around 15 mag in these bands and the optical variability we have identified is ≥ 5 mag fainter than that, any MIR variability is likely to be heavily suppressed into the noise of the WISE light curves.

CL-AGN show variability on similar timescales as those we have found here ([Ricci & Trakhtenbrot, 2023](#)). However, CL-AGN are a subset of AGN and the galaxies hosting our transients are not AGN according to the WISE criterion from [Hviding et al. \(2022\)](#). Our objects are also much lower luminosity than seen for CL-AGN, which also makes this classification unlikely.

4.4.1.3 CSM interaction

In [Terwel et al. \(2024\)](#), we estimated an intrinsic rate, through simulations of the detection efficiency for three out of 3 628 SNe Ia with potential late-time CSM signals, of <0.5 per cent of normal SNe Ia displaying late-time (> 100 d post peak) CSM signatures. [Dubay et al. \(2022\)](#) estimated a rate of late-time interaction in $<5\%$ of SNe Ia. In this work, we identified three SNe Ia whose signals in ZTF cannot be ruled out as being due to late-time CSM interaction, giving a raw rate of late onset CSM interaction of $\leq 0.1\%$ for the 5 618 SNe Ia in this sample (see Table 4.5). No potential late-time signature from CSM interaction was identified in any other SN type.

SN 2017frh is our best candidate for late-onset CSM interaction. It has the earliest period of late-time detections (~ 300 days after the first detection), and a similar estimate for M_{CSM} as [Graham et al. \(2019b\)](#) found for SN 2015cp. If we assume a nova-like shell at $T = 10^7$ K, we get a reasonable CSM mass of $M_{\text{CSM}} \approx 4 M_{\odot}$ (although see the discussion of the limitations of our CSM estimates in Section 4.4.2).

Our two other CSM candidates, SN 2017fby and SN 2016cob, have late-time signals five years after the SN was first detected. When we assume these objects to have shells of similar thickness as the shell in SN 2017frh, a CSM mass estimate of $\sim 5 M_{\odot}$ can be found for these objects as well. These estimates are lower limits, as no host extinction is assumed for objects in regions of galaxies where significant amounts of extinction can be expected.

We have not performed detailed rates calculations for the events discovered in this study. However, There are ~ 600 objects in our sample that were first detected less than 300 days before the start of ZTF, and we have one candidate with a late-time signal detected around 300 days after discovery. This gives a raw rate of 0.2 % when not taking into account any bias. Two additional candidates have their detections in the fifth year after the explosion. About half of our sample exploded less than five years before the start of ZTF, and have their fifth year observed the survey. Two of these are candidates for having late-time CSM interaction at these phases, giving a rate of 0.05% when not taking any bias into account. Our rough estimates of the rates suggest similar values to those of [Terwel et al. \(2024\)](#), within the uncertainty of the small numbers of events detected.

The three events in [Terwel et al. \(2024\)](#) that were identified as consistent with CSM interaction, were also close to their host nuclei. As discussed in [Terwel et al. \(2024\)](#), this could suggest a preference for CSM interaction to occur in SNe Ia in these environments or an alternative explanation is that they are caused by nuclear activity. However, as discussed in Section 4.4.1.2 and shown in Fig. 4.7, these late-time signals are similar but not entirely consistent with nuclear activity/transients.

4.4.2 Limitations

We found a large group of SNe whose tail was detected by ZTF but never properly picked up by the survey – all of them required more thorough baseline corrections as the transient was present in the reference images. Several of these were exceptionally long lived, with detections in the binned data being recovered over a year after the

start of ZTF. We also found some periodic variable sources that have this behaviour for at least the length of the survey, making it impossible to generate proper reference images or apply a good baseline correction. Both groups can leave behind a ghost, which is an imprint at the transient location when the object is fainter than it was in the references. These events can be recovered from the data, particularly if different time frames for estimating the baseline correction are used, but they are often hidden if a baseline correction is not applied.

As in [Terwel et al. \(2024\)](#), the magnitude limit of the binning technique is set by the magnitude limit of the references, as their uncertainty starts to dominate when more epochs of observation are binned together. One way to improve the sensitivity, though computationally expensive, is to find a region where we are certain there is no excess at the SN location and use it to generate custom references to use for difference imaging. This would immediately lessen the need for a baseline correction significantly, as an adequately chosen reference region already has this built in automatically.

Any search for late-time signals from SNe will also be dependent on the constraints placed on the sample. We required a first detection between 2008 and 2018 and a classification or candidate SN status. Our sample contained several false positives from objects that had spurious detections within the initial sample definition, but a SN (which was classified) exploded years later and was observed by ZTF. Siblings, whether they are true SN siblings or false due to spurious detections or projection effects, can be confused if they occur at (nearly) the same position in the sky. One way to remove false siblings, like AT 2017keg and SN 2013ld, is to require a spectroscopic classification in the same time period as the first detection, though this would also remove objects like SN 2017gcd as in that case only the second sibling was classified, and candidate objects like AT 2017fwf and AT 2017gpv that were never spectroscopically classified at all.

We attempted to estimate the CSM mass required to produce late-time detections as bright as we observed them, assuming Bremsstrahlung to be the main mechanism producing light. In most cases when assuming a thin nova-like shell the required CSM

mass is above $\sim 10 M_{\odot}$, with the only exception being SN 2017frh due to its relatively short delay time between the SN explosion and late-time detection. For SN 2016cob and SN 2017fby the only way to get realistic CSM mass estimates is by assuming a colder CSM and a lower F_R , which could be explained by the shell size that is needed for interaction to start over five years after the SN (see the end of Sect. 4.2.3). [Graham et al. \(2019b\)](#) argue that the simplified assumption of Bremsstrahlung being the main mechanism is largely responsible for the high CSM mass estimates. They find an upper limit of $M_{\text{CSM}} \sim 7 M_{\odot}$ for SN 2015cp with this method, while [Harris et al. \(2018b\)](#) find $M_{\text{CSM}} \lesssim 0.5 M_{\odot}$ using radio non-detections. They argue that line emission from elements such as H, Mg, and Ca are instead the main contributors to the emission. However, as line emission requires much more assumptions on the state of the emitting gas, it is much more complicated to derive a good estimation for M_{CSM} for it.

Even if we assume that Eq. 4.3 gives an upper limit and the better estimates from modelling of radio observations to be ~ 14 times smaller (based on the two estimates for SN 2015cp), the CSM interaction scenario for late-time signatures at 2000 – 4000 days post initial SN discovery is still unlikely for five of our events that are also potentially due to nuclear activity. We have also not considered the impact of extinction in the host galaxy, which is likely non-negligible given the nuclear location of the transients considered. The CSM mass can be reduced by assuming a smaller F_R , but the effect is limited unless we consider shells that are unphysically thin. However, thin shells are not ruled out by a several hundred day long period of late-time detections, as the time delay due to the large radius of the shell can smear even a 1 s interaction signal out over several months. This shows that it is very difficult to properly constrain the CSM mass from photometry alone without knowing the mechanism powering it and more detailed theoretical studies.

4.5 Conclusions

In this work we have presented a search for late-time signals observed in ZTF from transients that were first detected up to ten years before the start of the survey. By binning the ZTF data we were able to go nearly one magnitude below the noise limit of unbinned data points. Our sample consists of 8 707 unique objects that are in the ZTF footprint and could be searched for late-time signatures. By careful inspection of the ZTF images and comparison to known classes of transients, we determined the most likely source of the late-time signatures we identified at the positions of 98 transients discovered prior to ZTF starting. Our main conclusions are:

1. We identified several very long-lived transients that began pre-ZTF and continued for many hundreds to thousands of days. These include the SLSN IIn, SN 2015da, with data extending to eight years after discovery and the spectroscopically unclassified AT 2017gpv, whose bumpy long-lived light curve (detected up to nearly four years post discovery) is reminiscent of iPTF14hls ([Arcavi et al., 2017](#); [Sollerman et al., 2019](#)) and SN 2020faa ([Yang et al., 2021](#); [Salmaso et al., 2023](#)).
2. We found 10 confirmed pairs of sibling transients where the pre-ZTF and ZTF siblings are at nearly the same sky position. One additional unconfirmed but likely sibling transient was identified when applying our binning technique at the positions of SN 2017ige (it was detected by Pan-STARRS with internal name PS21aos). In the majority of the cases, one of the siblings was never spectroscopically classified. We also found two pairs where the ZTF transient was mistakenly reported as a pre-ZTF transient due to spurious detections from the nearby host.
3. We found six flux excesses at the position of events classified pre-ZTF as Type II SNe (three Type II, one IIn and two SLSN-II) consistent with AGN activity in known AGN host galaxies. We speculate that some of these were likely misclassified at the time of the pre-ZTF detection.

4. We found five flux excesses that were consistent with activity of the host nucleus close to the location of the original transient. The brightness, light curve shape, and duration are broadly consistent with (ambiguous) nuclear transients, showing that there may be a previously unknown population of faint nuclear transients that requires deeper (binned) observations to be discovered.

5. We found three flux excesses that were consistent with late-time interaction with a $4-5 M_{\odot}$ CSM shell, assuming Bremsstrahlung as the main emission mechanism. In two of these the signal is ~ 5 years after the SN and could also be explained by a nuclear unrelated to the SN. SN 2017frh is our best candidate with a signal ~ 300 days after the SN consistent with a $4 M_{\odot}$ nova-like CSM shell at 10^7 K. Although a nuclear transient can not be completely ruled out.

The Vera C. Rubin Observatory’s Legacy Survey of Space and Time (LSST; [Ivezić et al., 2019](#)) will observe the transient universe several magnitudes deeper than ZTF. This is crucial for finding faint interaction signals like those we have searched for in this paper, as we have shown these to be rare. Increasing the volume that can be probed is the best way to find new events and follow them up. Current samples of objects will be observed at late times by LSST, making it possible to do a late-time signal search in real-time. By using a well-defined and complete sample such as the ZTF SN Ia DR2 ([Rigault et al., 2024](#), , Smith et al. in prep.), Bright Transient Survey (BTS; [Fremling et al., 2020b](#); [Perley et al., 2020b](#)), or a similar sample for ZTF SNe first detected in 2021+ as the basis for a similar search of late-time signals observed with LSST, it will also be possible to properly estimate their rates. Not only can these methods be used to search for late-time CSM interaction, but as we have shown they are also suitable for finding other weak signals, such as faint nuclear transients.

4.6 Tables

Table 4.6: List of the 63 pre-ZTF objects whose tail is still visible in ZTF using our binning method after a baseline correction.

Name	Type	z	Discovery date	visible until (mjd)
AT 2017fwg	Candidate	0.113627	01-08-2017	58325
AT 2017gpv	Candidate	0.025563	04-09-2017	59480
AT 2017gpy	Candidate	0.025187	04-09-2017	58250
AT 2017hat	Candidate	0.020454	01-10-2017	58275
AT 2017igk	Candidate	0.040847	16-11-2017	58250
AT 2017ihh	Candidate	0.027521	03-10-2017	58300
AT 2017aho	Candidate	0.053421	17-11-2017	58250
AT 2017ims	Candidate	0.030094	15-11-2017	58300
AT 2017iru	Candidate	0.018156	29-11-2017	58375
ATLAS17nbe	Candidate	0.013476	05-11-2017	58400
ATLAS17oai	Candidate	0.099205	23-12-2017	58300
ATLAS18eas	Candidate	0.033103	30-12-2017	58325
ATLAS18mmr	Candidate	0.077507	15-12-2017	58325
DES16X2bkr	SN II	0.159	21-09-2016	58400
SN 2015da	SLSN IIn	0.007222	09-01-2015	59475
SN 2016bkv	SN II	0.002	21-03-2016	58475
SN 2016cyi	SN IIn	0.044	25-06-2016	58475
SN 2016ieq	SN IIn	0.066	14-11-2016	58400
SN 2017aym	SN IIP	0.005928	13-01-2017	58700
SN 2017dio	SN Ic	0.037	26-04-2017	58300
SN 2017dpu	SN II	0.018	30-04-2017	58250
SN 2017eby	SN Ia-CSM	0.081	01-04-2017	58350
SN 2017egm	SLSN I	0.030721	23-05-2017	58300
SN 2017emq	SN Ia	0.005247	03-06-2017	58250
SN 2017erp	SN Ia	0.006174	13-06-2017	58375
SN 2017err	SLSN IIn	0.107	12-06-2017	58275

Name	Type	z	Discovery date	visible until (mjd)
SN 2017faa	SN II	0.01845	27-06-2017	58300
SN 2017fgc	SN Ia	0.007722	11-07-2017	58400
SN 2017fvr	SN IIP	0.012539	01-08-2017	58450
SN 2017gas	SN IIn	0.011	10-08-2017	58850
SN 2017ghw	SN IIn	0.076	25-08-2017	58450
SN 2017glx	SN Ia-91T	0.011294	03-09-2017	58400
SN 2017gmr	SN IIP	0.005037	04-09-2017	58475
SN 2017gvb	SN IIn	0.030344	18-09-2017	59000
SN 2017gww	SN II	0.01748	26-09-2017	58375
SN 2017gxq	SN Ia	0.008406	17-09-2017	58450
SN 2017hcc	SN IIn	0.0173	02-10-2017	58500
SN 2017hbg	SN II	0.016	25-09-2017	58375
SN 2017hca	SN II	0.013403	28-09-2017	58450
SN 2017hfv	SN Ia	0.028199	10-10-2017	58200
SN 2017hix	SN Ic	0.012	13-10-2017	58375
SN 2017hlt	SN Ia	0.027	10-10-2017	58275
SN 2017hmi	SN Ia	0.0398	18-10-2017	58250
SN 2017hpa	SN Ia	0.015654	25-10-2017	58400
SN 2017hqj	SN IIP	0.009	27-10-2017	58300
SN 2017hro	SN II	0.015	28-10-2017	58800
SN 2017igf	SN Ia	0.005624	12-11-2017	58350
SN 2017ijr	SN Ia	0.04	20-11-2017	58300
SN 2017ijx	SN Ia	0.027729	18-11-2017	58300
SN 2017ivh	SN II	0.008	05-12-2017	58300
SN 2017ivu	SN IIP	0.006528	11-12-2017	58400
SN 2017ivv	SN II	0.022	12-12-2017	58450
SN 2017ixg	SN Ia	0.0277	14-12-2017	58400
SN 2017ixv	SN Ic-BL	0.007302	17-12-2017	58350

Name	Type	z	Discovery date	visible until (mjd)
SN 2017ixx	SN II	0.041	17-12-2017	58300
SN 2017ixz	SN I Ib	0.024	14-12-2017	58250
SN 2017iyd	SN I Ib	0.0285	13-12-2017	58275
SN 2017jav	SN Ia	0.01517	19-12-2017	58275
SN 2017bjj	SN II	0.013492	20-12-2017	58400
SN 2017jeh	SN Ia	0.020961	26-12-2017	58275
SN 2018L	SN Ia	0.02582	25-12-2017	58325
SN 2018bq	SN Ia	0.025628	30-12-2017	58275
SN 2018fd	SLSN I	0.263	11-10-2017	58450

4.7 Recovered non-SN sources

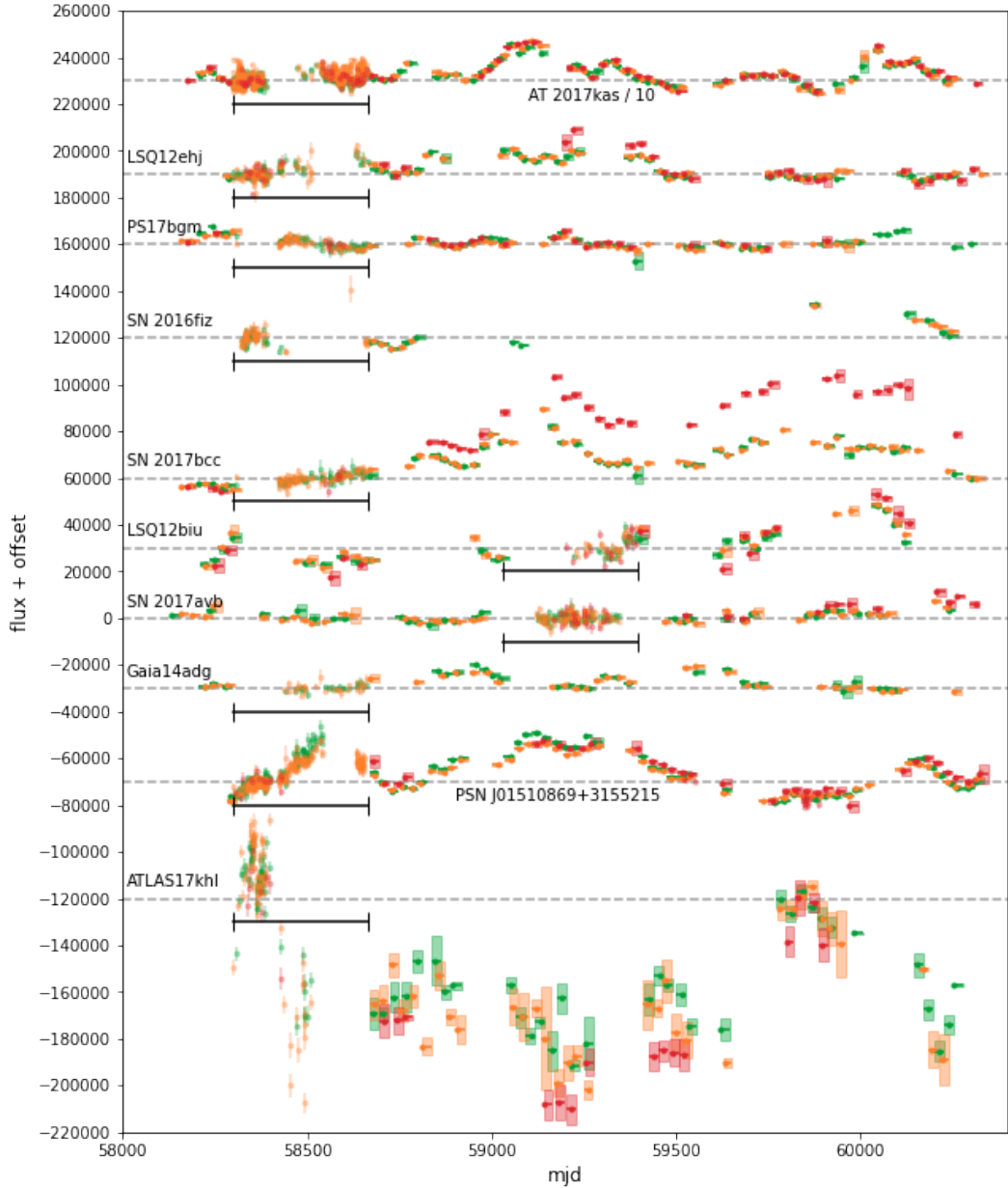


Figure 4.8: Binned flux of the recovered AGN. The flux is calibrated to a zeropoint at mag 30. The dashed lines show the baseline value for each object. Since the observations used to determine the baseline cannot be binned we show the unbinned data in the baseline region of each object, this region is marked by the black lines. Even though not all objects are properly sampled over the entire lifetime of ZTF, they all clearly show variability over long timescales. As these objects are always varying, it is impossible to do a baseline correction without the transient present. This causes some light curves to go below their baseline. Note that the values for AT 2017kas have been divided by 10 as the variability is so large.

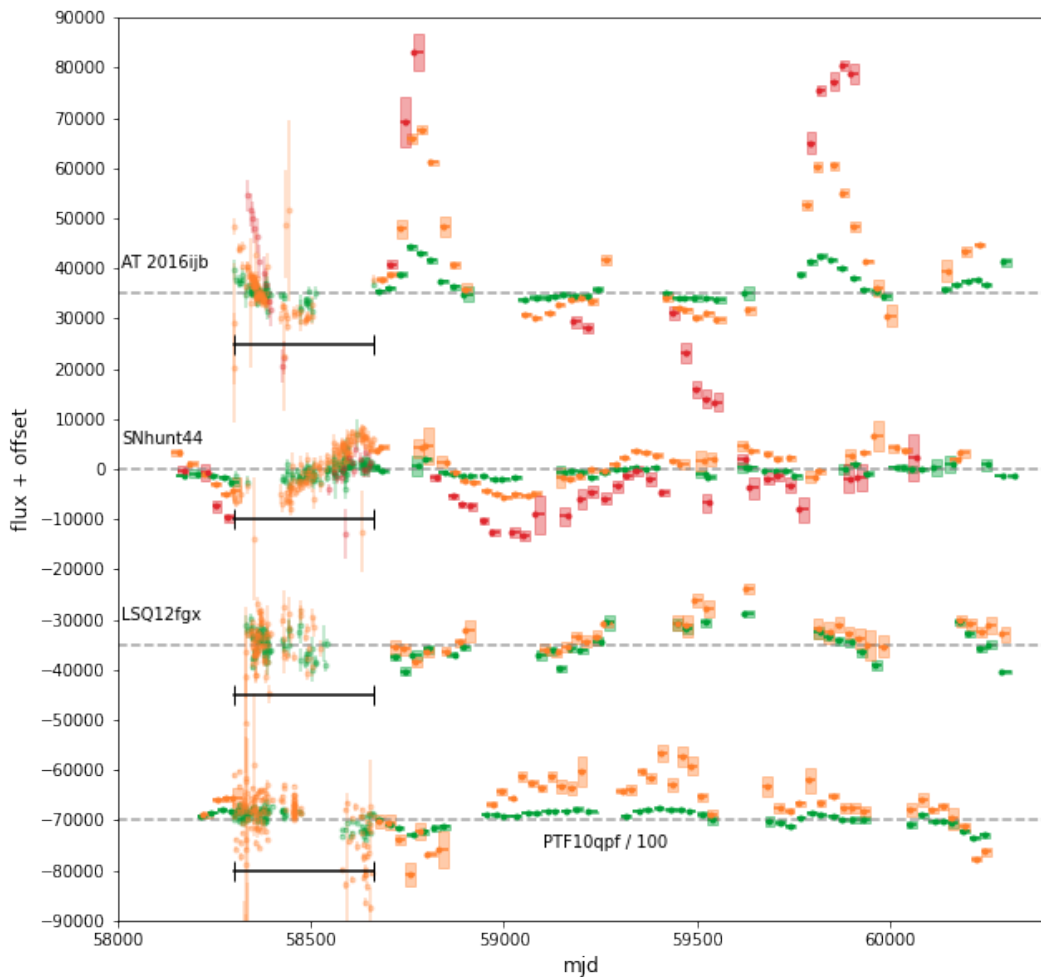


Figure 4.9: Binned flux of the recovered variable stars. The flux is calibrated to a zeropoint at mag 30. The dashed lines lines show the baseline for each object. Since the observations used to determine the baseline cannot be binned we show the unbinned data in the baseline region of each object, this region is marked by the black lines. All three objects vary around their central values, but the amplitude varies widely between the ZTF bands. Note that the values for PTF10qpf have been divided by 100 as the variability is so large.

References

- Adelman-McCarthy, J. K., Agüeros, M. A., Allam, S. S., et al. 2006, *Astrophysical Journal Supplemental Series*, 162, 38 (Cited on page 74.)
- Ailawadhi, B., Dastidar, R., Misra, K., et al. 2023, *Monthly Notices of the Royal Astronomical Society*, 519, 248 (Cited on pages 69 and 120.)
- Aldering, G., Antilogus, P., Bailey, S., et al. 2006, *Astrophysical Journal*, 650, 510 (Cited on page 18.)
- Alsabti, A. W. & Murdin, P. 2017, Supernovae and Supernova Remnants: The Big Picture in Low Resolution, ed. A. W. Alsabti & P. Murdin, 3 (Cited on page 6.)
- Anderson, J. P., González-Gaitán, S., Hamuy, M., et al. 2014, *Astrophysical Journal*, 786, 67 (Cited on page 124.)
- Andrews, J. E., Sand, D. J., Valenti, S., et al. 2019, *Astrophysical Journal*, 885, 43 (Cited on pages xv, 69, 110 and 112.)
- Antonucci, R. 1993, *Annual Review of Astronomy & Astrophysics*, 31, 473 (Cited on page 10.)
- Arcavi, I., Howell, D. A., Kasen, D., et al. 2017, *Nature*, 551, 210 (Cited on pages xv, 112, 113 and 136.)
- Barbary, K., Bailey, S., Barentsen, G., et al. 2021, SNCosmo (Cited on page 51.)
- Barbon, R., Ciatti, F., & Rosino, L. 1979, *Astronomy & Astrophysics*, 72, 287 (Cited on page 124.)
- Becker, A. 2015, HOTPANTS: High Order Transform of PSF ANd Template Subtraction, Astrophysics Source Code Library, record ascl:1504.004 (Cited on pages 37 and 80.)
- Bedding, T. R. & Zijlstra, A. A. 1998, *Astrophysical Journal Letters*, 506, L47 (Cited on page 11.)
- Bellm, E. C., Kulkarni, S. R., Barlow, T., et al. 2019a, *Publications of the Astronomical Society of the Pacific*, 131, 068003 (Cited on pages 28 and 96.)
- Bellm, E. C., Kulkarni, S. R., Graham, M. J., et al. 2019b, *Publications of the Astronomical Society of the Pacific*, 131, 018002 (Cited on pages 28 and 105.)
- Biswas, R., Goobar, A., Dhawan, S., et al. 2022, *Monthly Notices of the Royal Astronomical Society*, 509, 5340 (Cited on page 62.)
- Brown, P. J., Hosseinzadeh, G., Jha, S. W., et al. 2019, *Astrophysical Journal*, 877, 152 (Cited on pages xv, 110 and 112.)
- Bulla, M., Sim, S. A., Pakmor, R., et al. 2016, *Monthly Notices of the Royal Astronomical Society*, 455, 1060 (Cited on page 14.)
- Buzzoni, B., Delabre, B., Dekker, H., et al. 1984, *The Messenger*, 38, 9 (Cited on pages 31 and 80.)
- Camacho-Neves, Y., Jha, S. W., Barna, B., et al. 2023, arXiv e-prints, arXiv:2302.03105 (Cited on page 66.)

- Cardelli, J. A., Clayton, G. C., & Mathis, J. S. 1989, *Astrophysical Journal*, 345, 245 (Cited on pages 51 and 96.)
- Chambers, K. C., Boer, T. D., Bulger, J., et al. 2021, Transient Name Server Discovery Report, 2021-2390, 1 (Cited on page 116.)
- Chambers, K. C., Magnier, E. A., Metcalfe, N., et al. 2016, arXiv e-prints, arXiv:1612.05560 (Cited on page 31.)
- Chandrasekhar, S. 1931, The London, Edinburgh, and Dublin Philosophical Magazine and Journal of Science, 11, 592 (Cited on page 2.)
- Chugai, N. N., Blinnikov, S. I., Cumming, R. J., et al. 2004, *Monthly Notices of the Royal Astronomical Society*, 352, 1213 (Cited on page 21.)
- Chugai, N. N. & Yungelson, L. R. 2004, *Astronomy Letters*, 30, 65 (Cited on page 125.)
- Coughlin, M. W., Bloom, J. S., Nir, G., et al. 2023, *Astrophysical Journal Supplemental Series*, 267, 31 (Cited on pages 64 and 115.)
- Da Costa, G. S. 1992, in Astronomical Society of the Pacific Conference Series, Vol. 23, Astronomical CCD Observing and Reduction Techniques, ed. S. B. Howell, 90 (Cited on page 36.)
- Dahiwale, A. & Fremling, C. 2021, Transient Name Server Classification Report, 2021-135, 1 (Cited on page 20.)
- de Vaucouleurs, G., de Vaucouleurs, A., Corwin, Herold G., J., et al. 1991, Third Reference Catalogue of Bright Galaxies (Cited on page 4.)
- Dekany, R., Smith, R. M., Riddle, R., et al. 2020, *Publications of the Astronomical Society of the Pacific*, 132, 038001 (Cited on pages 28 and 96.)
- Dexter, J. & Kasen, D. 2013, *Astrophysical Journal*, 772, 30 (Cited on page 9.)
- Dey, A., Schlegel, D. J., Lang, D., et al. 2019, *Astronomical Journal*, 157, 168 (Cited on page 80.)
- Dhawan, S., Mortsell, E., Johansson, J., et al. 2024, arXiv e-prints, arXiv:2406.01434 (Cited on pages 115 and 131.)
- Dilday, B., Howell, D. A., Cenko, S. B., et al. 2012, *Science*, 337, 942 (Cited on page 20.)
- Dimitriadis, G., Burgaz, U., Deckers, M., et al. 2024, arXiv e-prints, arXiv:2409.04200 (Cited on pages 15 and 17.)
- Dimitriadis, G., Sullivan, M., Kerzendorf, W., et al. 2017, *Monthly Notices of the Royal Astronomical Society*, 468, 3798 (Cited on pages 47, 51, 64 and 66.)
- Dubay, L. O., Tucker, M. A., Do, A., Shappee, B. J., & Anand, G. S. 2022, *Astrophysical Journal*, 926, 98 (Cited on pages 23 and 132.)
- Duev, D. A., Mahabal, A., Masci, F. J., et al. 2019, *Monthly Notices of the Royal Astronomical Society*, 489, 3582 (Cited on page 64.)
- Dutta, A., Sahu, D. K., Anupama, G. C., et al. 2022, *Astrophysical Journal*, 925, 217 (Cited on pages 59 and 64.)
- Elias-Rosa, N., Brennan, S. J., Benetti, S., et al. 2024, *Astronomy & Astrophysics*, 686, A13 (Cited on page 22.)
- Feindt, U., M., R., V., B., & J., N. 2019a, ufeindt/simsurvey: 0.6.0 (Cited on page 50.)

- Feindt, U., Nordin, J., Rigault, M., et al. 2019b, , 2019, 005 (Cited on pages 50, 52 and 96.)
- Ferretti, R., Amanullah, R., Goobar, A., et al. 2016, *Astronomy & Astrophysics*, 592, A40 (Cited on page 18.)
- Filippenko, A. V. 1982, *Publications of the Astronomical Society of the Pacific*, 94, 715 (Cited on page 28.)
- Filippenko, A. V., Richmond, M. W., Matheson, T., et al. 1992, *Astrophysical Journal Letters*, 384, L15 (Cited on page 17.)
- Fink, M., Röpke, F. K., Hillebrandt, W., et al. 2010, *Astronomy & Astrophysics*, 514, A53 (Cited on page 13.)
- Forster, F., Bauer, F. E., Arredondo, J., et al. 2019, Transient Name Server Discovery Report, 2019-2185, 1 (Cited on page 115.)
- Fox, O. D., Filippenko, A. V., Skrutskie, M. F., et al. 2013, *Astronomical Journal*, 146, 2 (Cited on page 22.)
- Fraser, M., Magee, M., Kotak, R., et al. 2013, *Astrophysical Journal Letters*, 779, L8 (Cited on page 21.)
- Fremling, C., Miller, A. A., Sharma, Y., et al. 2020a, *Astrophysical Journal*, 895, 32 (Cited on page 60.)
- Fremling, C., Miller, A. A., Sharma, Y., et al. 2020b, *Astrophysical Journal*, 895, 32 (Cited on page 137.)
- Friesen, B., Baron, E., Parrent, J. T., et al. 2017, *Monthly Notices of the Royal Astronomical Society*, 467, 2392 (Cited on page 94.)
- Frohmaier, C., Sullivan, M., Maguire, K., & Nugent, P. 2018, *Astrophysical Journal*, 858, 50 (Cited on pages 17 and 85.)
- Frohmaier, C., Sullivan, M., Nugent, P. E., et al. 2019, *Monthly Notices of the Royal Astronomical Society*, 486, 2308 (Cited on pages 85 and 96.)
- Gaia Collaboration, Prusti, T., de Bruijne, J. H. J., et al. 2016, *Astronomy & Astrophysics*, 595, A1 (Cited on page 31.)
- Gal-Yam, A. 2019, *Annual Review of Astronomy & Astrophysics*, 57, 305 (Cited on page 9.)
- Gal-Yam, A., Bruch, R., Schulze, S., et al. 2022, *Nature*, 601, 201 (Cited on page 21.)
- Gibson, B. K., Stetson, P. B., Freedman, W. L., et al. 2000, *Astrophysical Journal*, 529, 723 (Cited on page 11.)
- Graham, M. J., Kulkarni, S. R., Bellm, E. C., et al. 2019a, *Publications of the Astronomical Society of the Pacific*, 131, 078001 (Cited on page 28.)
- Graham, M. L., Fremling, C., Perley, D. A., et al. 2022a, *Monthly Notices of the Royal Astronomical Society*, 511, 241 (Cited on page 62.)
- Graham, M. L., Fremling, C., Perley, D. A., et al. 2022b, *Monthly Notices of the Royal Astronomical Society*, 511, 241 (Cited on page 115.)
- Graham, M. L., Harris, C. E., Nugent, P. E., et al. 2019b, *Astrophysical Journal*, 871, 62 (Cited on pages 22, 43, 52, 56, 82, 83, 86, 90, 92, 108, 109, 110, 123, 132 and 135.)

- Graham, M. L., Nugent, P. E., Sullivan, M., et al. 2015, *Monthly Notices of the Royal Astronomical Society*, 454, 1948 (Cited on page 95.)
- Graur, O., Zurek, D., Shara, M. M., et al. 2016, *Astrophysical Journal*, 819, 31 (Cited on pages 18 and 67.)
- Groh, J. H., Meynet, G., Georgy, C., & Ekström, S. 2013, *Astronomy & Astrophysics*, 558, A131 (Cited on page 21.)
- Guillochon, J., Parrent, J., Kelley, L. Z., & Margutti, R. 2017, *Astrophysical Journal*, 835, 64 (Cited on page 101.)
- Gunn, J. E., Siegmund, W. A., Mannery, E. J., et al. 2006, *Astronomical Journal*, 131, 2332 (Cited on page 74.)
- Guy, J., Astier, P., Baumont, S., et al. 2007, *Astronomy & Astrophysics*, 466, 11 (Cited on page 51.)
- Hammerstein, E., van Velzen, S., Gezari, S., et al. 2023, *Astrophysical Journal*, 942, 9 (Cited on pages 71, 74, 75 and 98.)
- Hamuy, M., Phillips, M., Suntzeff, N., & Maza, J. 2003a, , 8151, 2 (Cited on page 18.)
- Hamuy, M., Phillips, M. M., Suntzeff, N. B., et al. 2003b, *Nature*, 424, 651 (Cited on pages 18 and 122.)
- Harris, C. E., Nugent, P. E., Horesh, A., et al. 2018a, *Astrophysical Journal*, 868, 21 (Cited on page 83.)
- Harris, C. E., Nugent, P. E., Horesh, A., et al. 2018b, *Astrophysical Journal*, 868, 21 (Cited on page 135.)
- Harris, C. E., Nugent, P. E., & Kasen, D. N. 2016, *Astrophysical Journal*, 823, 100 (Cited on page 108.)
- Hicken, M., Garnavich, P. M., Prieto, J. L., et al. 2007, *Astrophysical Journal Letters*, 669, L17 (Cited on page 17.)
- Hill, J. M., Green, R. F., & Slagle, J. H. 2006, in Society of Photo-Optical Instrumentation Engineers (SPIE) Conference Series, Vol. 6267, Society of Photo-Optical Instrumentation Engineers (SPIE) Conference Series, ed. L. M. Stepp, 62670Y (Cited on page 51.)
- Hills, J. G. 1975, *Nature*, 254, 295 (Cited on page 10.)
- Hinkle, J. T. 2024, *Monthly Notices of the Royal Astronomical Society*, 531, 2603 (Cited on page 11.)
- Hinkle, J. T., Holoi, T. W. S., Shappee, B. J., et al. 2022, *Astrophysical Journal*, 930, 12 (Cited on pages xvi, 11, 124 and 131.)
- Hinkle, J. T., Shappee, B. J., Auchettl, K., et al. 2024, arXiv e-prints, arXiv:2405.08855 (Cited on pages 11 and 122.)
- Holtzman, J. A., Marriner, J., Kessler, R., et al. 2008, *Astronomical Journal*, 136, 2306 (Cited on page 43.)
- Howell, D. A., Sullivan, M., Nugent, P. E., et al. 2006, *Nature*, 443, 308 (Cited on page 17.)
- Hoyle, F. & Fowler, W. A. 1960, *Astrophysical Journal*, 132, 565 (Cited on page 7.)

- Hviding, R. E., Hainline, K. N., Rieke, M., et al. 2022, *Astronomical Journal*, 163, 224 (Cited on pages 67, 69, 117 and 132.)
- Iben, I., J. & Tutukov, A. V. 1984, *Astrophysical Journal Supplemental Series*, 54, 335 (Cited on page 14.)
- Inserra, C., Fraser, M., Smartt, S. J., et al. 2016a, *Monthly Notices of the Royal Astronomical Society*, 459, 2721 (Cited on page 20.)
- Inserra, C., Fraser, M., Smartt, S. J., et al. 2016b, *Monthly Notices of the Royal Astronomical Society*, 459, 2721 (Cited on pages 123 and 125.)
- Irani, I., Prentice, S. J., Schulze, S., et al. 2022, *Astrophysical Journal*, 927, 10 (Cited on page 89.)
- Isern, J., Mochkovitch, R., García-Berro, E., & Hernanz, M. 1997, *Astrophysical Journal*, 485, 308 (Cited on page 2.)
- Itagaki, K. 2024, Transient Name Server Discovery Report, 2024-39, 1 (Cited on page 4.)
- Ivezić, Ž., Kahn, S. M., Tyson, J. A., et al. 2019, *Astrophysical Journal*, 873, 111 (Cited on pages 91 and 137.)
- Jayasinghe, T., Stanek, K. Z., Kochanek, C. S., et al. 2019, *Monthly Notices of the Royal Astronomical Society*, 485, 961 (Cited on page 31.)
- Jordan, George C., I., Perets, H. B., Fisher, R. T., & van Rossum, D. R. 2012, *Astrophysical Journal Letters*, 761, L23 (Cited on pages 15 and 66.)
- Kankare, E., Kotak, R., Mattila, S., et al. 2017, *Nature Astronomy*, 1, 865 (Cited on page 11.)
- Kasen, D. 2006, *Astrophysical Journal*, 649, 939 (Cited on page 8.)
- Kasen, D., Woosley, S. E., & Heger, A. 2011, *Astrophysical Journal*, 734, 102 (Cited on page 9.)
- Kashi, A. & Soker, N. 2011, *Monthly Notices of the Royal Astronomical Society*, 417, 1466 (Cited on page 13.)
- Kasliwal, M. M., Cannella, C., Bagdasaryan, A., et al. 2019, *Publications of the Astronomical Society of the Pacific*, 131, 038003 (Cited on page 64.)
- Kasliwal, M. M., Kulkarni, S. R., Gal-Yam, A., et al. 2012, *Astrophysical Journal*, 755, 161 (Cited on page 17.)
- Katsuda, S., Mori, K., Maeda, K., et al. 2015, *Astrophysical Journal*, 808, 49 (Cited on page 21.)
- Kawabata, M., Kawabata, K. S., Maeda, K., et al. 2018, *Publications of the Astronomical Society of Japan*, 70, 111 (Cited on page 66.)
- Kelly, P. L., Hicken, M., Burke, D. L., Mandel, K. S., & Kirshner, R. P. 2010, *Astrophysical Journal*, 715, 743 (Cited on page 8.)
- Khokhlov, A. M. 1991, *Astronomy & Astrophysics*, 245, L25 (Cited on page 13.)
- Kilpatrick, C. D., Drout, M. R., Auchettl, K., et al. 2021, *Monthly Notices of the Royal Astronomical Society*, 504, 2073 (Cited on page 69.)
- Kippenhahn, R., Weigert, A., & Weiss, A. 2013, Stellar Structure and Evolution (Cited on pages x, 1 and 3.)
- Kool, E. C., Johansson, J., Sollerman, J., et al. 2023, *Nature*, 617, 477 (Cited on pages 21, 60, 88 and 89.)

- Krause, O., Tanaka, M., Usuda, T., et al. 2008, *Nature*, 456, 617 (Cited on page 18.)
- Kromer, M., Fink, M., Stanishev, V., et al. 2013, *Monthly Notices of the Royal Astronomical Society*, 429, 2287 (Cited on pages 15 and 66.)
- Kulkarni, S. R. 2013, *The Astronomer's Telegram*, 4807, 1 (Cited on page 31.)
- Kuncarayakti, H., Maeda, K., Ashall, C. J., et al. 2018, *Astrophysical Journal Letters*, 854, L14 (Cited on pages xv, 110 and 112.)
- Law, N. M., Kulkarni, S. R., Dekany, R. G., et al. 2009, *Publications of the Astronomical Society of the Pacific*, 121, 1395 (Cited on pages 31, 51, 94 and 95.)
- Leloudas, G., Hsiao, E. Y., Johansson, J., et al. 2015, *Astronomy & Astrophysics*, 574, A61 (Cited on pages 21 and 22.)
- Lintott, C., Schawinski, K., Bamford, S., et al. 2011, *Monthly Notices of the Royal Astronomical Society*, 410, 166 (Cited on page 89.)
- Livne, E. & Arnett, D. 1995, *Astrophysical Journal*, 452, 62 (Cited on page 13.)
- Maeda, K., Tanaka, M., Nomoto, K., et al. 2007, *Astrophysical Journal*, 666, 1069 (Cited on page 9.)
- Masci, F. J., Laher, R. R., Rusholme, B., et al. 2019, *Publications of the Astronomical Society of the Pacific*, 131, 018003 (Cited on pages 28 and 107.)
- Mazzali, P. A., Röpke, F. K., Benetti, S., & Hillebrandt, W. 2007, *Science*, 315, 825 (Cited on page 13.)
- Mazzali, P. A., Sullivan, M., Filippenko, A. V., et al. 2015, *Monthly Notices of the Royal Astronomical Society*, 450, 2631 (Cited on page 95.)
- Mazzali, P. A., Sullivan, M., Hachinger, S., et al. 2014, *Monthly Notices of the Royal Astronomical Society*, 439, 1959 (Cited on pages xii, 54, 69 and 94.)
- McCully, C., Crawford, S., Kovacs, G., et al. 2018, astropy/astroscrappy: v1.0.5 Zenodo Release (Cited on page 35.)
- McCully, C., Jha, S. W., Scalzo, R. A., et al. 2022, *Astrophysical Journal*, 925, 138 (Cited on page 66.)
- Miller, A. A., Silverman, J. M., Butler, N. R., et al. 2010, *Monthly Notices of the Royal Astronomical Society*, 404, 305 (Cited on page 22.)
- Miller, A. A., Yao, Y., Bulla, M., et al. 2020, *Astrophysical Journal*, 902, 47 (Cited on pages 44 and 103.)
- Mochkovitch, R. 1983, *Astronomy & Astrophysics*, 122, 212 (Cited on page 2.)
- Nomoto, K. 1982, *Astrophysical Journal*, 253, 798 (Cited on page 13.)
- Nomoto, K., Suzuki, T., Deng, J., Uenishi, T., & Hachisu, I. 2005, in *Astronomical Society of the Pacific Conference Series*, Vol. 342, 1604-2004: Supernovae as Cosmological Lighthouses, ed. M. Turatto, S. Benetti, L. Zampieri, & W. Shea, 105 (Cited on pages 18 and 20.)
- Nordin, J., Brinnel, V., Santen, J. V., et al. 2021, Transient Name Server Discovery Report, 2021-2254, 1 (Cited on page 116.)
- Nugent, P. E., Sullivan, M., Cenko, S. B., et al. 2011, *Nature*, 480, 344 (Cited on page 94.)

- Pakmor, R., Kromer, M., Röpke, F. K., et al. 2010, *Nature*, 463, 61 (Cited on page 14.)
- Pakmor, R., Kromer, M., Taubenberger, S., et al. 2012, *Astrophysical Journal Letters*, 747, L10 (Cited on page 14.)
- Parrent, J. T., Howell, D. A., Friesen, B., et al. 2012, *Astrophysical Journal Letters*, 752, L26 (Cited on page 94.)
- Patat, F. 2005, *Monthly Notices of the Royal Astronomical Society*, 357, 1161 (Cited on pages 18 and 67.)
- Patat, F., Cordiner, M. A., Cox, N. L. J., et al. 2013, *Astronomy & Astrophysics*, 549, A62 (Cited on page 51.)
- Patnaude, D. J., Badenes, C., Park, S., & Laming, J. M. 2012, *Astrophysical Journal*, 756, 6 (Cited on page 21.)
- Pauli, W. 1925, *Zeitschrift fur Physik*, 31, 765 (Cited on page 1.)
- Pereira, R., Thomas, R. C., Aldering, G., et al. 2013, *Astronomy & Astrophysics*, 554, A27 (Cited on page 94.)
- Perets, H. B., Gal-Yam, A., Mazzali, P. A., et al. 2010, *Nature*, 465, 322 (Cited on page 17.)
- Perley, D. A., Fremling, C., Sollerman, J., et al. 2020a, *Astrophysical Journal*, 904, 35 (Cited on page 60.)
- Perley, D. A., Fremling, C., Sollerman, J., et al. 2020b, *Astrophysical Journal*, 904, 35 (Cited on page 137.)
- Perley, D. A., Schulze, S., Fremling, C., et al. 2021, Transient Name Server AstroNote, 156, 1 (Cited on page 20.)
- Peterson, B. M. & Horne, K. 2004, *Astronomische Nachrichten*, 325, 248 (Cited on page 10.)
- Phillips, M. M. 1993, *Astrophysical Journal Letters*, 413, L105 (Cited on page 8.)
- Piersanti, L., Gagliardi, S., Iben, Icko, J., & Tornambé, A. 2003a, *Astrophysical Journal*, 598, 1229 (Cited on page 14.)
- Piersanti, L., Gagliardi, S., Iben, Icko, J., & Tornambé, A. 2003b, *Astrophysical Journal*, 583, 885 (Cited on page 14.)
- Planck Collaboration, Aghanim, N., Akrami, Y., et al. 2020, *Astronomy & Astrophysics*, 641, A6 (Cited on page 24.)
- Prajs, S., Sullivan, M., Smith, M., et al. 2017, *Monthly Notices of the Royal Astronomical Society*, 464, 3568 (Cited on page 85.)
- Raskin, C. & Kasen, D. 2013, *Astrophysical Journal*, 772, 1 (Cited on page 20.)
- Rau, A., Kulkarni, S. R., Law, N. M., et al. 2009, *Publications of the Astronomical Society of the Pacific*, 121, 1334 (Cited on pages 31, 51, 94 and 95.)
- Ravi, A. P., Rho, J., Park, S., et al. 2023, *Astrophysical Journal*, 950, 14 (Cited on page 69.)
- Rees, M. J. 1988, *Nature*, 333, 523 (Cited on page 10.)
- Reusch, S. 2020, ztffps (Cited on page 43.)
- Reusch, S. 2023, simeonreusch/fpbot: Release 1.1.3 (Cited on pages 37 and 102.)

- Ricci, C. & Trakhtenbrot, B. 2023, *Nature Astronomy*, 7, 1282 (Cited on pages 10 and 132.)
- Richardson, D., Jenkins, Robert L., I., Wright, J., & Maddox, L. 2014, *Astronomical Journal*, 147, 118 (Cited on page 6.)
- Riess, A. G., Yuan, W., Macri, L. M., et al. 2021, arXiv e-prints, arXiv:2112.04510 (Cited on page 9.)
- Rigault, M. 2018, ztfquery, a python tool to access ZTF data (Cited on page 49.)
- Rigault, M., Smith, M., Goobar, A., et al. 2024, arXiv e-prints, arXiv:2409.04346 (Cited on pages 15 and 137.)
- Rosswog, S., Kasen, D., Guillochon, J., & Ramirez-Ruiz, E. 2009, *Astrophysical Journal Letters*, 705, L128 (Cited on page 14.)
- Ruiz-Lapuente, P., Cappellaro, E., Turatto, M., et al. 1992, *Astrophysical Journal Letters*, 387, L33 (Cited on page 17.)
- Saha, A., Thim, F., Tammann, G. A., Reindl, B., & Sandage, A. 2006, *Astrophysical Journal Supplemental Series*, 165, 108 (Cited on page 11.)
- Salmaso, I., Cappellaro, E., Tartaglia, L., et al. 2023, *Astronomy & Astrophysics*, 673, A127 (Cited on page 136.)
- Schlegel, D. J., Finkbeiner, D. P., & Davis, M. 1998, *Astrophysical Journal*, 500, 525 (Cited on pages 96 and 98.)
- Schulze, S., Gal-Yam, A., Dessart, L., et al. 2024, arXiv e-prints, arXiv:2409.02054 (Cited on page 22.)
- Scolnic, D., Brout, D., Carr, A., et al. 2021, arXiv e-prints, arXiv:2112.03863 (Cited on page 9.)
- Shappee, B. J., Prieto, J. L., Grupe, D., et al. 2014, *Astrophysical Journal*, 788, 48 (Cited on page 31.)
- Shappee, B. J. & Stanek, K. Z. 2011, *Astrophysical Journal*, 733, 124 (Cited on page 51.)
- Shappee, B. J., Stanek, K. Z., Kochanek, C. S., & Garnavich, P. M. 2017, *The Astrophysical Journal*, 841, 48 (Cited on page 51.)
- Sharma, Y., Sollerman, J., Fremling, C., et al. 2023, *Astrophysical Journal*, 948, 52 (Cited on pages 18, 22, 60, 79, 86, 87 and 89.)
- Shen, K. J. & Bildsten, L. 2009, *Astrophysical Journal*, 699, 1365 (Cited on page 13.)
- Silverman, J. M., Nugent, P. E., Gal-Yam, A., et al. 2013, *Astrophysical Journal Supplemental Series*, 207, 3 (Cited on page 18.)
- Smartt, S. J., Valenti, S., Fraser, M., et al. 2015, *Astronomy & Astrophysics*, 579, A40 (Cited on pages 31 and 80.)
- Smee, S. A., Gunn, J. E., Uomoto, A., et al. 2013, *Astronomical Journal*, 146, 32 (Cited on page 74.)
- Smith, N., Andrews, J. E., Milne, P., et al. 2024, *Monthly Notices of the Royal Astronomical Society*, 530, 405 (Cited on page 112.)
- Smith, N., Mauerhan, J. C., Cenko, S. B., et al. 2015a, *Monthly Notices of the Royal Astronomical Society*, 449, 1876 (Cited on page 21.)

- Smith, N., Mauerhan, J. C., Cenko, S. B., et al. 2015b, *Monthly Notices of the Royal Astronomical Society*, 449, 1876 (Cited on page 87.)
- Soker, N. 2015, *Monthly Notices of the Royal Astronomical Society*, 450, 1333 (Cited on pages 18 and 20.)
- Sollerman, J., Taddia, F., Arcavi, I., et al. 2019, *Astronomy & Astrophysics*, 621, A30 (Cited on pages xv, 112, 113, 114 and 136.)
- Sollerman, J., Yang, S., Schulze, S., et al. 2021, *Astronomy & Astrophysics*, 655, A105 (Cited on page 120.)
- Soraisam, M., Matheson, T., Lee, C.-H., et al. 2022, *Astrophysical Journal Letters*, 926, L11 (Cited on page 113.)
- Stahl, B. E., Zheng, W., de Jaeger, T., et al. 2020, *Monthly Notices of the Royal Astronomical Society*, 492, 4325 (Cited on pages 94 and 95.)
- Stanishev, V., Goobar, A., Amanullah, R., et al. 2018, *Astronomy & Astrophysics*, 615, A45 (Cited on page 96.)
- Stritzinger, M., Mazzali, P. A., Sollerman, J., & Benetti, S. 2006, *Astronomy & Astrophysics*, 460, 793 (Cited on page 7.)
- Strotjohann, N. L., Ofek, E. O., Gal-Yam, A., et al. 2021, *Astrophysical Journal*, 907, 99 (Cited on pages 47 and 57.)
- Strubbe, L. E. & Quataert, E. 2009, *Monthly Notices of the Royal Astronomical Society*, 400, 2070 (Cited on page 10.)
- Subrayan, B. M., Milisavljevic, D., Chornock, R., et al. 2023, *Astrophysical Journal Letters*, 948, L19 (Cited on page 11.)
- Sullivan, M., Conley, A., Howell, D. A., et al. 2010, *Monthly Notices of the Royal Astronomical Society*, 406, 782 (Cited on page 8.)
- Taam, R. E. 1980, *Astrophysical Journal*, 242, 749 (Cited on page 13.)
- Tartaglia, L., Pastorello, A., Sollerman, J., et al. 2020, *Astronomy & Astrophysics*, 635, A39 (Cited on pages xv, 110 and 112.)
- Taubenberger, S. 2017, The Extremes of Thermonuclear Supernovae, ed. A. W. Alsabti & P. Murdin, 317 (Cited on pages x, 15 and 16.)
- Taubenberger, S., Elias-Rosa, N., Kerzendorf, W. E., et al. 2015, *Monthly Notices of the Royal Astronomical Society*, 448, L48 (Cited on page 95.)
- Terwel, J. H., Maguire, K., Dimitriadis, G., et al. 2024, arXiv e-prints, arXiv:2402.16962 (Cited on pages 23, 42, 102, 103, 105, 106, 115, 119, 123, 129, 131, 132, 133 and 134.)
- Tonry, J., Denneau, L., Heinze, A., et al. 2019, Transient Name Server Discovery Report, 2019-2239, 1 (Cited on page 115.)
- Tonry, J. L., Denneau, L., Heinze, A. N., et al. 2018, *Publications of the Astronomical Society of the Pacific*, 130, 064505 (Cited on page 31.)
- Tripp, R. 1998, *Astronomy & Astrophysics*, 331, 815 (Cited on page 8.)
- Tsebrenko, D. & Soker, N. 2015, *Monthly Notices of the Royal Astronomical Society*, 447, 2568 (Cited on page 20.)

- Urry, C. M. & Padovani, P. 1995, *Publications of the Astronomical Society of the Pacific*, 107, 803 (Cited on page 10.)
- van der Walt, S. J., Crellin-Quick, A., & Bloom, J. S. 2019, *Journal of Open Source Software*, 4 (Cited on pages 64 and 115.)
- van Dokkum, P. G. 2001, *Publications of the Astronomical Society of the Pacific*, 113, 1420 (Cited on page 35.)
- van Velzen, S., Gezari, S., Hammerstein, E., et al. 2021, *Astrophysical Journal*, 908, 4 (Cited on page 69.)
- Wandel, A., Peterson, B. M., & Malkan, M. A. 1999, *Astrophysical Journal*, 526, 579 (Cited on page 10.)
- Wang, L., Baade, D., & Patat, F. 2007, *Science*, 315, 212 (Cited on page 14.)
- Webbink, R. F. 1984, *Astrophysical Journal*, 277, 355 (Cited on page 14.)
- Whelan, J. & Iben, Icko, J. 1973, *Astrophysical Journal*, 186, 1007 (Cited on page 13.)
- Wiseman, P., Wang, Y., Hönig, S., et al. 2023, *Monthly Notices of the Royal Astronomical Society*, 522, 3992 (Cited on page 11.)
- Wiseman, P., Williams, R. D., Arcavi, I., et al. 2024, arXiv e-prints, arXiv:2406.11552 (Cited on pages 11 and 132.)
- Wood-Vasey, W. M., Wang, L., & Aldering, G. 2004, *Astrophysical Journal*, 616, 339 (Cited on page 18.)
- Wright, E. L., Eisenhardt, P. R. M., Mainzer, A. K., et al. 2010, *Astronomical Journal*, 140, 1868 (Cited on pages 32, 69 and 117.)
- Yamanaka, M., Kawabata, K. S., Kinugasa, K., et al. 2009, *Astrophysical Journal Letters*, 707, L118 (Cited on page 17.)
- Yan, L., Lunyan, R., Perley, D. A., et al. 2017, *Astrophysical Journal*, 848, 6 (Cited on page 10.)
- Yang, S., Sollerman, J., Chen, T. W., et al. 2021, *Astronomy & Astrophysics*, 646, A22 (Cited on pages 112, 113 and 136.)
- Yao, Y., Miller, A. A., Kulkarni, S. R., et al. 2019, *Astrophysical Journal*, 886, 152 (Cited on pages 44 and 103.)
- Yaron, O. & Gal-Yam, A. 2012, *Publications of the Astronomical Society of the Pacific*, 124, 668 (Cited on pages xvii, 51, 94 and 101.)
- York, D. G., Adelman, J., Anderson, John E., J., et al. 2000, *Astronomical Journal*, 120, 1579 (Cited on page 74.)
- Zackay, B., Ofek, E. O., & Gal-Yam, A. 2016, *Astrophysical Journal*, 830, 27 (Cited on pages 37 and 43.)
- Zhang, K., Wang, X., Zhang, J., et al. 2016, *Astrophysical Journal*, 820, 67 (Cited on pages xiii, 65, 66, 94 and 95.)
- Zhu, J., Jiang, N., Dong, S., et al. 2023, *Astrophysical Journal*, 949, 23 (Cited on pages xv, 110 and 112.)